Ph.D. Program in Civil, Chemical and Environmental Engineering

Curriculum in Chemical, Materials and Processes Engineering

Department of Civil, Chemical and Environmental Engineering

Polytechnic School, University of Genoa, Italy.

Among old materials and different approaches to enhance stability and electrochemical activity of Solid Oxide Cells

Davide Clematis

AMONG OLD MATERIALS AND DIFFERENT APPROACHES TO ENHANCE STABILITY AND ELECTROCHEMICAL ACTIVITY OF SOLID OXIDE CELLS

BY

DAVIDE CLEMATIS

Dissertation discussed in partial fulfillment of
the requirements for the Degree of

DOCTOR OF PHILOSOPHY

Civil, Chemical and Environmental Engineering
Curriculum in Chemical, Materials and Processes Engineering,
Department of Civil, Chemical and Environmental Engineering, University of Genoa, Italy

March, 2019

Advisers:
Prof. Antonio Barbucci – Department of Civil, Chemical and Environmental Engineering, University of Genoa
Prof. Marco Panizza – Department of Civil, Chemical and Environmental Engineering, University of Genoa

External Reviewers:
Prof. Juergen Fleig – Department Institute of Chemical Technologies and Analytics, Technical University of Vienna
Prof. Cristiano Nicolella – Department of Civil and Industrial Engineering, University of Pisa

Examination Committee:
Prof. Renzo Di Felice – Department of Civil, Chemical and Environmental Engineering, University of Genoa
Prof. Giovanna Ferrari – Department of Industrial Engineering, University of Salerno
Prof. Linda Barelli – Department of Engineering, University of Perugia

Ph.D. program in Civil, Chemical and Environmental Engineering

Curriculum in Chemical, Materials and Processes Engineering

Cycle XXXI

Acknowledgements

This thesis was developed in the Electrochemistry Laboratory of the Department of Civil, Chemical and Environmental Engineering (DICCA) of University of Genoa and in the Institute of Chemical Technologies and Analytics, Division "Technical Electrochemistry" at Technical University of Wien.

First I would like to express my gratitude to my supervisors Professor Antonio Barbucci and Professor Marco Panizza, whom with their competence supported me in these three years.

A great thank is for the Professor Maria Paola Carpanese, always ready to give fundamental advices, and a relevant scientific contribution to my growth, and Dr. Alice Giuliano, who helped me in the first period of PhD with her knowledge, laughs and encouragements.

I would like to sincerely thank Professor Juergen Fleig to host me in his group at TU Wien in the Institute of Chemical Technologies and Analytics, giving me the opportunity to work in a scientifically advanced, but always friendly, environment and Doctor Markus Kubicek, to follow me step by step with high precision and competence. A big thank also to Stefie, Tobias, Alex V., Alex S., Alex. H., Max, Stefan and Clemens for helping me on any occasion and giving me funny moments.

Backing to Italy I would like to be very grateful to Professor Antonio Bertei, a perfect mixing of skills and curiosity, and to Doctor Massimo Viviani and Doctor Sabrina Presto for their scientific and technical support in results interpretation.

I wish to thank all the staff of Department of Civil, Chemical and Environmental Engineering for assistance during experimental measurements.

A special thanks to all my friends who supported me every time and everywhere. All my gratitude is for my parents, my sister, Marta, bearers of serenity and Valentina, who colors the world.

Abstract

Among old materials and different approaches to enhance stability and electrochemical activity of Solid Oxide Cells

Perovskite materials are widely studied as cathode materials for intermediate-temperature solid oxide fuel cells (IT-SOFC) for their relevant properties regarding electrocatalytic activity or stability. Nevertheless, a material that combines both it is not yet available. Among them, $La_{1-X}Sr_xMnO_3$ (LSM), $La_{1-x}Sr_xCo_{1-y}Fe_yO_3$ (LSCF), $Ba_{1-x}Sr_xCo_{1-y}Fe_yO_3$ (BSCF), $La_{1-x}Sr_xFeO_3$ (LSF), $La_{1-x}Ba_xCoO_3$ (LBC), were deeply investigated but their properties are not completely exploited or optimized.

In this PhD project all the reported electrode materials are investigated using different approaches. The study starts from LSM – based electrodes, which show a change in kinetic mechanism under particular operating conditions. These results open new horizons about the employment of this material, up today considered not suitable for IT-SOFC temperature range. A first application, with promising results, is proposed here with a LSM infiltration in LSCF and BSCF scaffold. The presence of infiltrated-phase enhance stability and electrochemical activity of electrodes.

Promising results are obtained also by mixing BSCF and LSCF powders. Three different BSCF:LSCF ratio are considered to produce three different cathodes. All the new compositions show an improvement of activity for oxygen reduction reaction, with very competitive values of polarization resistance. Moreover, one of these new electrodes has also a lowering of degradation rate compared with reference materials

In the last year of this project, other two materials are combined and their interactions investigate. LSF, providing a high stability, is coupled with LBC, which has a really high surface electrocatalytic activity. The two materials are tested in different thin film systems. When they are mixed before the sintering stage react forming a new perovskite phase ($Ba_{0.099}Sr_{0.297}La_{0.594}Fe_{0.8}Co_{0.2}O_3$), with a higher activity. The reaction is avoided producing a bilayer system, and the presence of LBC top layer over a LSF dense thin film drastically reduces polarization resistance, highlighting promising results.

CHAPTER 1

Solid oxide cells – A brief introduction

1.1 Electrochemical device at high temperature – Solid Oxide Cells

A Solid Oxide Cell (SOC) is an electrochemical device which can operate in fuel cell mode (Solid Oxide Fuel Cell - SOFC) or in electrolysis cell mode (Solid Oxide Electrolysis Cell – SOEC) (Fig. 1. 1). Both technologies are highly interesting and promising for power to gas production or energy production respectively (1-3).

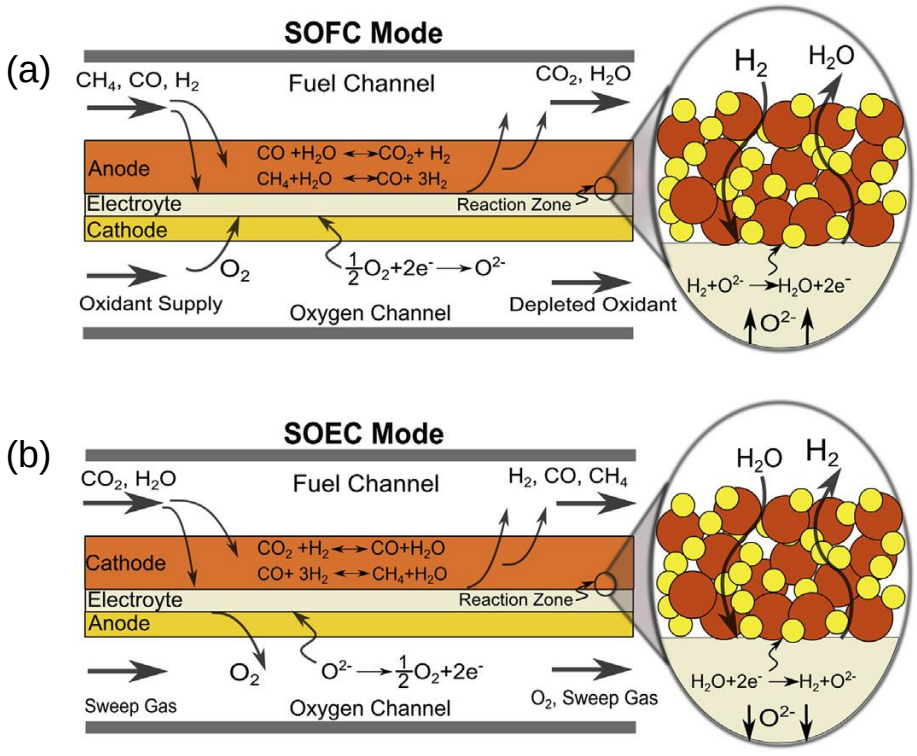

Fig. 1. 1 (a) SOFC and **(b)** SOEC working principle

A SOC consists in a three layers (anode, electrolyte and cathode) each of them with proper electrocatalytic properties toward a specific reaction and/or conductivity which have to last long over the time. Then, considering the typically harsh operating conditions chemical, thermal and mechanical stability have to be obtained by an accurate material selection and design (4, 5). Anode and cathode require porous structure and are the site for electrochemical reaction, the electrolyte is sandwiched between the two electrodes. This component must provide ionic conductivity and a dense structure to avoid gas cross over. It is also possible to build a reversible SOC able to operate in both SOEC and SOFC mode. During operation, reactants are supplied to the cell through channels designed in the metallic interconnects and go across the porous electrode structures.

Typically such cells are piled up to realize a cell stack in order to improve productivity. Cells in the stack are interconnected by metallic plats according to a bipolar or monopolar configuration. Furthermore, the overall system became more complex considering the gas manifolds and other surrounding devices (control system, reformer …). Although each component of the complete system has its peculiarities and play a relevant role, the pulsating hearth remain the single cell. The flexibility of such concept together with the use of poor materials has strongly attracted the scientific and technological communities, because it is clear that the proper exploitation of SOCs provide a realistic and valuable piece in the yet incomplete future energy scenario puzzle that is in some way also nicely represented by the vision of Zheng et al in the picture reported in Fig. 1. 2.

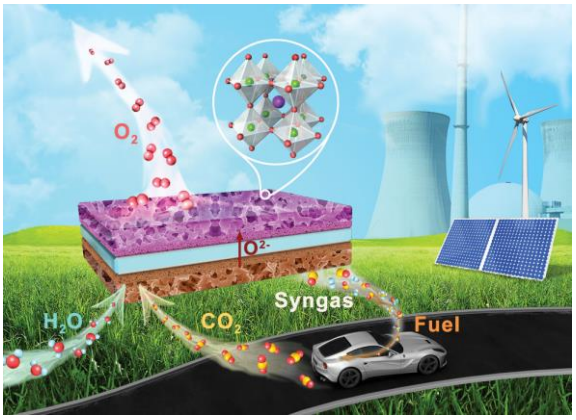

Fig. 1. 2 Co-electrolysis scenario from (5)

In case of SOEC mode H_2O/CO_2 mixture is reduced at fuel electrode, producing H_2/CO. Oxygen ions released at anode side cross the electrolyte and at cathode oxygen is formed. The process requires and consumes heat and electrical energy

During the high temperature co – electrolysis three main reactions occur:

i) Steam electrolysis: $H_2O \rightarrow H_2 + 1/2\, O_2$

ii) Carbon dioxide electrolysis: $CO_2 \rightarrow CO + 1/2\, O_2$

iii) Water Gas Shift: $H_2 + CO_2 \rightarrow H_2O + CO$

The overall reaction for high temperature co-electrolysis of H_2O and CO_2 is: $CO_2 + H_2O \rightarrow CO + H_2 + O_2$

On the other hand SOFC represents a noteworthy technology thanks to its electrical efficiency higher than conventional system for power generation. Moreover the efficiency is not strictly related with the plant size, and coupling with a size flexibility, SOFC allows to cover a wide power range.

Materials of each component play a key role to define the electrocatalytic properties and degradation rate of cell due to the high operating temperature. The state of art and commercial SOFC are mainly based on a cermet of Ni-YSZ anode or fuel electrode; this part of cell usually provides the mechanical support for other layers. Between the electrodes Yttria Stabilized Zirconia (YSZ) is deposited as electrolyte, while on the side of air channel Lanthanum Strontium Cobalt Iron Oxide (LSCF) ($La_{0.6}Sr_{0.4}Co_{0.2}Fe_{0.8}O_3$) is deposited. An interlayer of Gadolinium-doped Ceria is deposited between the YSZ electrolyte and LSCF cathode to prevent or limit the reaction.

An SOFC requires that fuel (hydrogen or hydrocarbons) and oxygen (air or pure oxygen) are supply to anode and cathode respectively. When hydrocarbons are fed to fuel electrode internal or external reforming it is required.

Fig. 1. 3 shows the basic process occurring during operative phase in an SOFC.

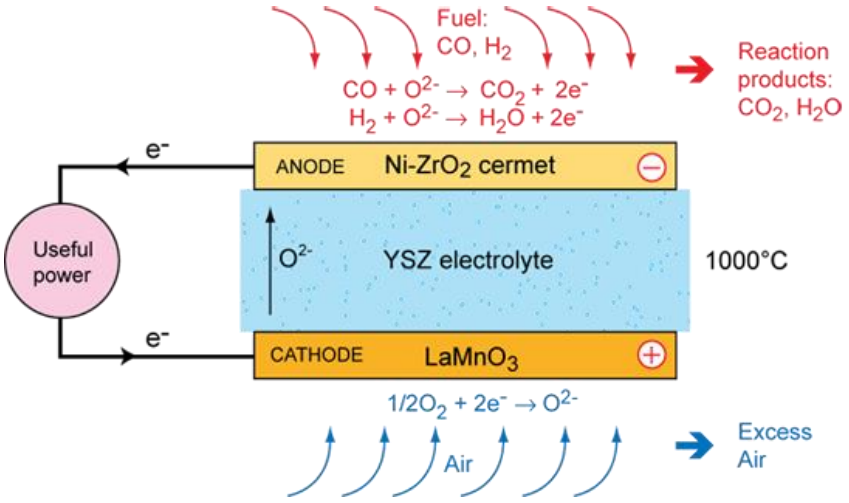

Fig. 1. 3 Sketch of SOFC operating principles and state of art for materials from (6)

Air is supplied to the cathode side, oxygen is adsorbed onto electrode surface and reacting with electrons forms ions able to cross the ionic conductive dense phase of electrolyte. At the other side of electrolyte ion oxygen can reacts oxidizing the fuel such as H_2, CO with the production of H_2O or CO_2 releasing electrons.

As introduced before, fuel can be a hydrocarbons; for this configuration a reforming of hydrocarbons is needed. If it directly inside the cell, it is called internal reforming, otherwise we speak about external reforming. In the second case it is important to keep in mind that external device and utilities will be required, complicating process layout. On the other hand an internal reforming needed an active material for reforming reactions. In case methane possible reactions are the steam reforming methane reaction and the water gas shift (Eq. 1.1 – Eq. 1.2)

$$CH_4 + H_2O \leftrightarrow CO + 3H_2 \quad (1.1)$$

$$CO + H_2O \leftrightarrow CO_2 + H_2 \quad (1.2)$$

then the global reaction is Eq. 1.3

$$CH_4 + 2H_2O \leftrightarrow CO_2 + 4H_2 \quad (1.3)$$

As at the anode side the oxidation occurs, at the cathode oxygen reduction takes place, then two electrochemical half-cells can be identified. Staring from the reaction (1.4)

$$H_2 + 1/2\,O_2 \rightarrow H_2O \quad (1.4)$$

the maximum work obtainable is related with the free energy change of the reaction.

The following thermodynamic discussion will be presented in terms of Gibbs energy. Reaction (1.4) is thermodynamically favored; the energy of the products is less than that of reactants. For an electrochemical device the standard free energy variation (ΔG) is defined as:

$$\Delta G = -nFE \quad (1.5)$$

where ΔG is the free energy change, n is the number of moles of electrons involved, E is the reversible potential, and F is Faraday's constant (96485 C mol^{-1}). When the reactants and the products are in their standard states, Eq. 1.5 can be expressed such as:

$$\Delta G^0 = -nFE^0 \quad (1.6)$$

Considering that for Eq.1.4 ΔG = 229 kJ/mol, n = 2, the corresponding value for E is 1.229 V.

The performance of an ideal fuel cell can be evaluated in several ways and the most commonly used is the Nernst potential represented as the cell voltage, expressed for the reaction (Eq.1.4) as:

$$E = E^0 + \frac{RT}{2F}\ln\left(\frac{\frac{p_{H_2}}{p}\left(\frac{p_{O_2}}{p}\right)^{0.5}}{\frac{p_{H_2O}}{p}}\right) \quad (1.7)$$

From Eq.1.7 it is clear that the Nernst equation highlights the change of potential E as a function of temperature and partial pressure of reactants and products. Then, the ideal cell voltage at operating conditions can be determined by this equation, once the ideal potential at standard condition is known.

The ideal and real performance of an electrochemical device such as a SOFC can differ a lot, as reported in Fig. 1. 4. Fuel cell released electrical energy when a current is drawn, but the actual potential is lowered from its equilibrium potential due to irreversible losses.

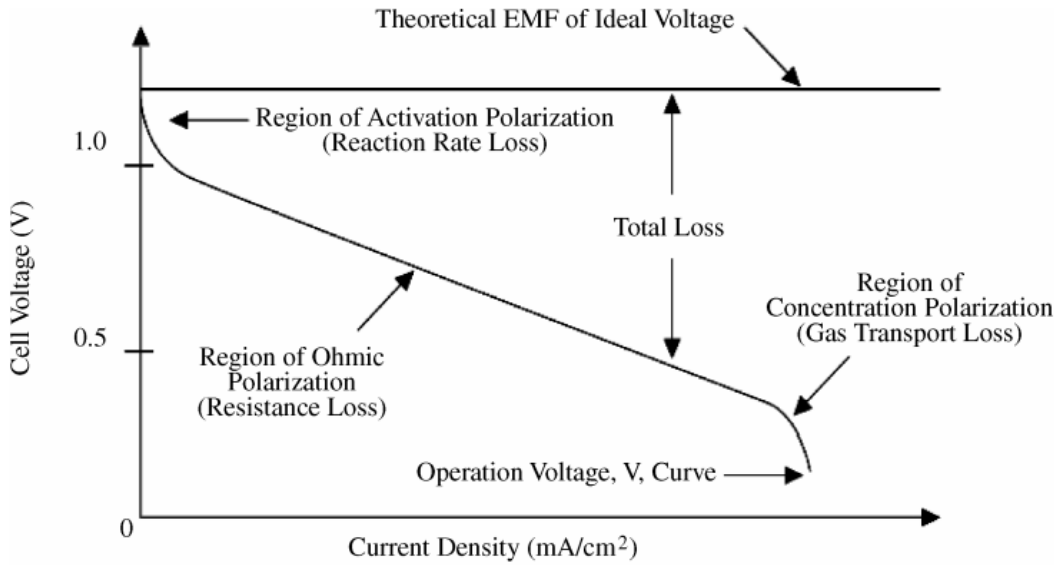

Fig. 1. 4 Ideal and real performance of a fuel cell represents as potential response

Losses can be caused by different phenomena and the main contributions are *activation, ohmic* and *concentration* polarizations.

A*ctivation polarization* (η_{act}) is evident at low current density, where the electronic barriers must be overcome to obtain a current and ionic flow. This value is proportional to the increase of current flow and can be presented as:

$$\eta_{act} = \frac{RT}{\alpha nF} \ln\left(\frac{i}{i_0}\right) \tag{1.8}$$

where R is the universal gas constant, T the temperature, α the charge transfer coefficient, n the number of electrons involved, F the Faraday constant, i the current density, and i_0 the exchange current density. This quantity is strictly related with reduction and oxidation process rate. In particular it is related with the electron exchange kinetics between the redox species at the electrode interface.

Ohmic polarization (η_{ohm}) changes proportionally to the increase in current and it represented as:

$$\eta_{ohm} = iR_c \tag{1.9}$$

where R_c is the cell resistance. Then ohmic losses are generate by the resistance to the flow of ions in the electrolyte and flow of electrons through the electrodes and the

external electrical circuit. The main source for this kind of resistance is the electrolyte and can be limited using a thin electrolyte layer and increasing its ionic conductivity.

Concentration polarization (η_{conc}) occur over the entire range of current density, becoming predominant at high current densities; in this conditions for gas reactant flow becomes difficult to reach the reaction sites at electrode, then this losses depends on the mass transfer kinetics. The concentration losses at cathode and anode side can be defined respectively as:

$$\eta_{conc,c} = \frac{RT}{2F} \ln \left[\frac{p_{O_2}^{bulk}}{p_{O_2}^{TPB}} \right]^{0.5} \tag{1.10}$$

$$\eta_{conc,a} = \frac{RT}{2F} \ln \left[\frac{p_{H_2}^{bulk}}{p_{H_2}^{TPB}} \frac{p_{H_2O}^{TPB}}{p_{H_2O}^{bulk}} \right] \tag{1.11}$$

Many processes can cause concentration polarization, such as (i) slow diffusion of the gases phase in the electrode pores, (ii) solution of the reactants into the electrolyte, (iii) dissolution of products out of the system, (iv) diffusion of reactants and products, from the reaction sites, through the electrolyte.

1.2 State of art and challenges in SOFC

SOC operation it is closely influenced by several electrochemical and thermodynamic variables (temperature, pressure, gas concentration, current density) which directly influence the cell potential and voltage losses. Modification of operating variables can lead to a positive or negative impact on fuel cell performance, extending the effects on other system components

For a fuel cell important information about working conditions can be obtained from voltage – current density and power density – current density curve, as reported in Fig. 1. 5

Generally operating conditions are chosen at a point on the left side of the power density peak, and at the same time considering a compromise between low operating cost and low capital cost.

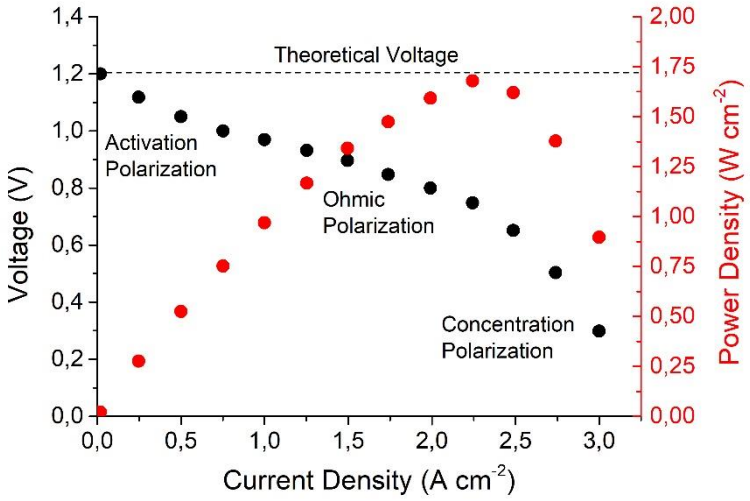

Fig. 1. 5 Typical I – V curve (black) and power density curve (red) for a fuel cell.

As introduced before SOFC features make these kind of system extremely suitable for the energy production. Nevertheless, despite several advantages the hard operating conditions impose strong constraints on the choice of material. The main problems are related with degradation phenomena, chemical and mechanical compatibility among different parts. Hence, one of the first goal in current research is the decreasing of temperature moving from 800 – 850 °C to the intermediate temperature range between 500 – 700 °C, without losses in power density and efficiency. In fact, the lowering of temperature leads to a reduction of thermal stresses and can limit degradation phenomena, but on the other hand has a negative impact on material properties, such as ionic conductivity of electrolyte and electrocatalytic activity of electrodes. Then, the development of new electrode and electrolyte materials maintaining a good mechanical and chemical compatibility between them is a key challenge.

Based on these preliminary assumptions a brief introduction about material for each part of a SOFC and possible cell geometry is reported in the following paragraph.

1.2.1 Materials for SOFC

- *Electrolyte materials*

Electrolyte must provide high ionic conductivity coupling with a low electronic conductivity, stability in reducing and oxidizing atmosphere and also a good thermal and mechanic properties are required. The mostly widely studied electrolyte materials for SOFC are Yttria – stabilized Zirconia (YSZ), Gadolinium or Samarium-doped Ceria (GDC and SDC) and Strontium, Magnesium-doped Lanthanum Gallate (LSGM). Fig. 1. 6 reports some value of ionic conductivity for SOFC electrolyte (7).

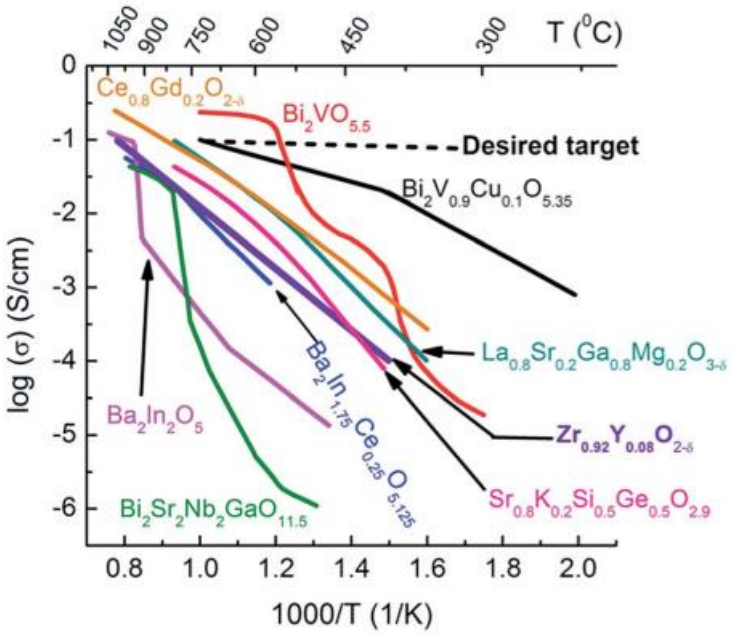

Fig. 1. 6 Oxide ion conductivities for SOFC electrolyte (7).

Fig. 1. 7 shows oxygen ions transport mechanism of migration, that occurs in electrolyte such as YSZ, SDC, GDC. They have a cubic fluorite structure which is stabilized by the introduction of (substitution or doping) with a small amount of divalent or trivalent cations. As example in Yttria-stabilized Zirconia (YSZ) electrolyte, Zr^{4+} present in ZrO_2 lattice is substituted by Y^{3+} using Y_2O_3. This produce oxygen vacancies at the oxygen positions enhancing oxygen mobility and then ion conductivity, by an hopping transport mechanism (6).

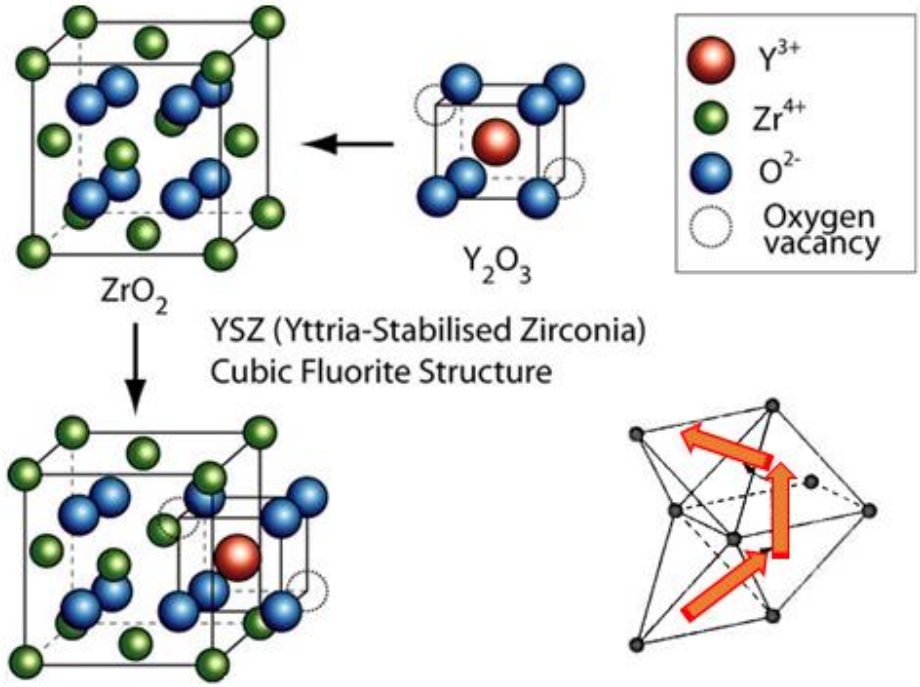

Fig. 1. 7 Mechanism for oxygen ion conductivity in Yttria-stabilized Zirconia**.** Orange arrows indicate path for oxygen ions migration from (6)**.**

For High – Temperature SOFC (HT-SOFC) the most common electrolyte is YSZ able to provide sufficient ionic conductivity and mechanic properties; nevertheless with the decreasing of operating temperature has a detrimental effect on its properties, in particular on conductivity (8, 9). This limitation required the development of new electrolyte materials, such as LSGM which shows a higher ionic conductivity also at lower temperature. In this case the main problems are related with Gallium price and the elevated fabrication temperature. Intensive efforts have been made about Ceria-based electrolyte doped with rare earth (SDC and GDC); this electrolyte family shows a very promising ionic conductivity even at low temperature (10, 11). For electrolyte such as SDC and GDC the problems rise up at higher temperature (close to 700 °C) due to the reduction of Ce^{4+} to Ce^{3+}, especially in the reducing condition at the anode side, with the increasing of its electronic conductivity.

As introduced before mechanical and thermal properties have a relevant effect on the choice of cell materials and a good compatibility among different parts must be achieve. Table 1. 1 reports thermal expansion coefficient (TEC) for some electrolyte materials and the temperature range considered.

Electrolyte Composition	**T (°C)**	**TEC (x 10^6 K^{-1})**	**Ref.**
$Zr_{0.9}Y_{0.1}O_{2-\delta}$	30 – 1000	11	(12)
$Ce_{0.9}Gd_{0.1}O_{2-\delta}$	30 – 800	13.4	(13)
$Ce_{0.8}Gd_{0.2}O_{2-\delta}$	30 – 800	11.8	(13)
$Ce_{0.9}Sm_{0.1}O_{2-\delta}$	30 – 1000	11.4	(14)
$La_{0.8}Sr_{0.2}Ga_{0.8}Mg_{0.2}O_{3-\delta}$	30 – 900	11.4	(15)

Table 1. 1 Average thermal expansion coefficient for SOFC electrolytes

TEC matching between electrolyte and electrodes can be achieve tailoring and optimizing both materials, and in general is necessary that TEC for electrodes is lower than ~ 15 x 10^{-6} K^{-1} to do not ruin stability and fuel cell performance (16, 17).

- *Anode materials*

Nickel (Ni) and Yttria-stabilized Zirconia (YSZ) are the main two materials used for SOFC anodes. They usually are used mixed forming a cermets and providing all the features required such as catalytic activity, due to the presence of Ni particles, and an excellent conductivity thank to the YSZ electrolyte inside the structure. Moreover, the presence of electrolyte in the anode mixture avoids or reduces the growth and coalescence of Ni particles, maintaining the desired particles size distribution after long-term operation at elevate temperature. In fact, performance of the anode are strongly related with its microstructure, affected both precursors' powder and degradation phenomena (18, 19).

Another important feature is the extension of three phase boundary (TPB) which is the point where the metal with electronic conductivity (Ni) is contact with the electrolyte, providing the ionic path and gas phase, as sketches in Fig. 1. 8

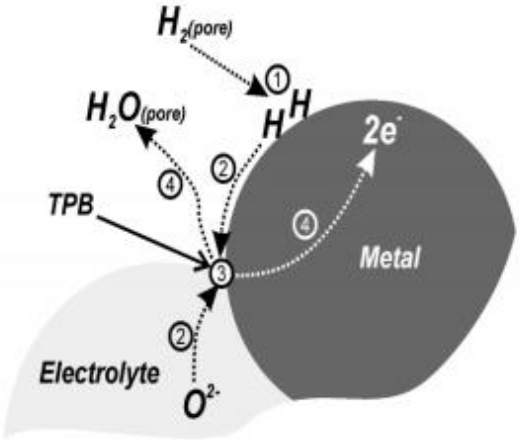

Fig. 1. 8 Reaction mechanism at anode side in SOFC.

For SOFC working with an internal reforming, anodes based on Ni – YSZ mixture are not suitable because they are prone to carburization in presence of hydrocarbon fuels (20, 21). To avoid electrode failure after few hours of operation new electrode systems have been proposed based on Nickel – Copper (Ni- Cu); other works highlight that the further addition of ceria helps in prevent carburization phenomena reducing performance degradation. Also the ternary system Cobalt – Copper – YSZ gave promising results; the substitution of Ni with Co has a beneficial effect on anode deactivation due to the Cu segregation at surface (22).

- *Cathode materials*

Lanthanum – Strontium manganite oxide (LSM) is the typical electrode material for HT – SOFC with an YSZ electrolyte; it exhibits high electronic conductivity, good stability under oxidizing atmospheres, and a TEC compatible with those of electrolytes. For LSM – based electrode the active zone for oxygen reduction reaction is narrow and close to the electrolyte interface, where the TPB provides all the conductive paths (electronic and ionic), to make the reaction possible. This mechanism is well presented

in Fig. 1. 9 (a) (23). Then, for the electrodes having a prevalent electronic conductivity, performance are highly related with the electrode morphology and sensitive to the formation of secondary phase.

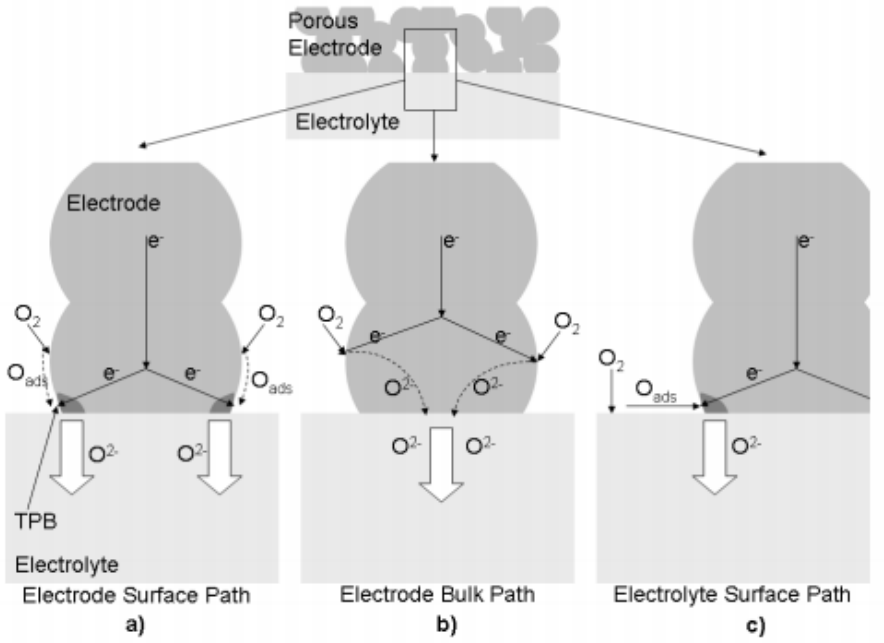

Fig. 1. 9 Possible reaction pathways at cathode side for oxygen reduction reaction (23).

The extension of electrocatalytic region active for ORR is a crucial point to improve cathode performance; to achieve this goal several strategies have been proposed, and among them production of composite electrode (24) or the employment of mixed ionic and electronic conductor (MIEC) (25) are the most common. In this last scheme, reaction can take place far from TPB at electrode/electrolyte interface as reported in Fig. 1. 9 (b). MIEC materials provide both electronic and ionic conductivity and then all the electrode/gas interface should be suitable for oxygen reduction. In fact when oxygen ion is formed, it can be transport through electrode bulk to cathode/electrolyte interface. Nevertheless the complete comprehension of kinetic mechanism involved at cathode side for ORR it is far to be achieve, due to the system complexity and large number of phenomena involved (26).

Introduction of these new materials, allow to achieve acceptable performance even lowering the operating temperature. Among cathode properties, oxygen surface

exchange *k* (cm/s) and oxygen ion diffusion coefficient *D* (cm^2/s) are important factors to evaluate electrode performance. These two properties are fundamental to determine the net oxygen flux crossing the gas – electrode interface and the diffusion of oxygen ion – electron hole pairs in the bulk of the MIEC, respectively (27). As a function of their values system can be controlled by surface or bulk diffusion phenomena, but even both processes can controlled the kinetic rate. Fig. 1. 10 shows possible steps involved in oxygen reduction reaction (Fig. 1. 10 (a)) and parameters involved in surface and solid-state diffusion phenomena (Fig. 1. 10 (b)).

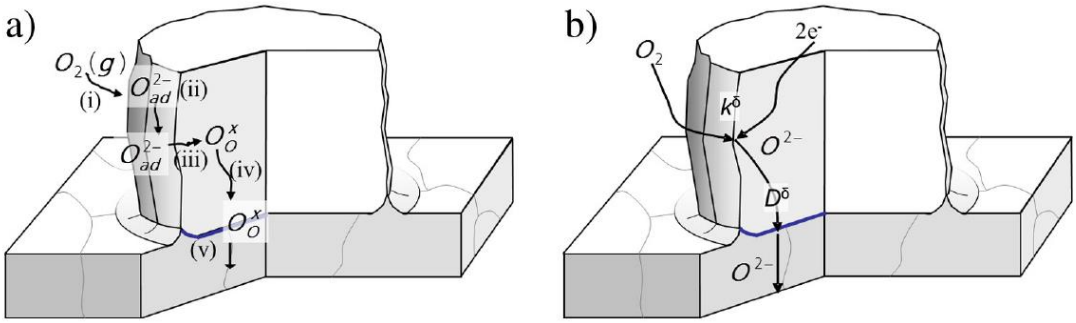

Fig. 1. 10 (a) Steps involved in oxygen reduction reaction **(b)** material parameters involved in the different steps (27).

Fig. 1. 11 reports as an example the strong effect that parameters *k* and *D* have on polarization resistance for a $La_{0.8}Sr_{0.2}CoO_{3-x}$ electrode (21).

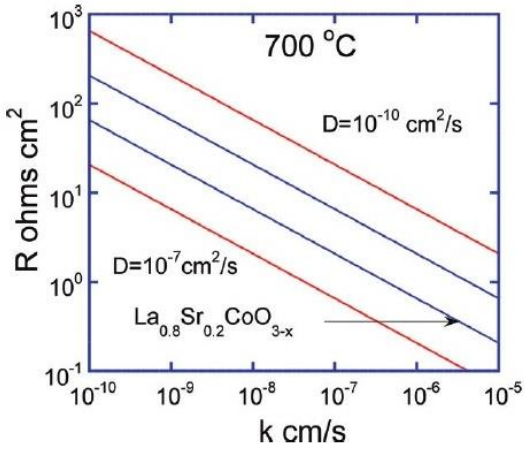

Fig. 1. 11 Evaluation of effect of *k* and *D* on polarization resistance of $La_{0.8}Sr_{0.2}CoO_{3-x}$

Perovskite is a class of materials, which received a high attention in the last decades as cathode for IT-SOFC, and many works have been focused on Doped $LaCoO_3$, $BaCoO_3$ or $LaFeO_3$. Their structure can be general represented as ABO_3, where A is rare earth or earth alkaline cation, B is a transition metal. The structure defects, oxygen stoichiometry and charge transport could be significantly modified, introducing an acceptor in the A-site and both acceptor and donor in the B-site, altering the oxygen vacancy concentration, then the oxygen diffusivity. A general formula for a double – substituted perovskite with an oxygen deficiency is $A_{1-x}A'_xB_{1-y}B'_yO_{3-\delta}$. Many studies dealing with the effect of A and B site substitutions are reported in literature (28) evaluating defect structure and oxygen transport.

Among these substituted perovskite materials, a well investigated compound is $La_{1-x}Sr_xFe_{1-y}Co_yO_{3-\delta}$ (LSCF). For this electrode dopant addition (e.g x=0.4 and y=0.2) provides a noteworthy enhancement in the total conductivity and electrochemical activity. Indeed, the presence of acceptor-type cations enhances the concentration of oxygen vacancies and *p*-type electronic charge carries. Nevertheless, increasing Sr^{2+}content above 50% and decreasing average cation radius in A (A=La, Ba …) sites promote vacancy – ordering with a negative influence on transport properties (29). Best performance for LSCF electrode have been achieved with $La_{0.6}Sr_{0.4}Fe_{0.8}Co_{0.2}O_{3-\delta}$ (LSCF64) stoichiometry in anode-supported cell made on Ni – YSZ/YSZ/SDC/LSCF (30). The presence of Ceria interlayer between YSZ electrolyte and LSCF electrode is required to avoid interdiffusion among the phases. The mentioned cell is able to produce a power density of 2.6 W cm^{-2} at 0.7 V at 750 °C in flowing oxygen.

Further manganite and ferrite-based electrodes, also cobalts-based materials have been developed; they show a good ionic and electronic conductivity and astonishing electrochemical activity. On the other hands the presence of cobalt introduce a severe problem related with thermal expansion coefficient, higher than 20 x 10^{-6} K^{-1}, limiting the compatibility with electrolyte.

Extremely remarkable performance obtained by Shao et al. (25) with a $Ba_{0.5}Sr_{0.5}Co_{0.8}Fe_{0.2}O_{3-\delta}$ (BSCF) electrode currently remains the target value for polarization resistance. The Area Specific Resistance (ASR) associated to this material by Shao's group is close to 0.05 Ω cm^2 at 600 °C and 0.5 at 500 °C in a symmetric

BSCF/SDC cell configuration. Tested in Ni-SDC/SDC/BSCF cell configuration the power density obtained at 600 °C and 500 °C are 1.01 W cm^2 and 0.402 W cm^2, respectively, that are extremely promising considering the working temperature range.

1.3 Scope of the thesis

A lowering of operating temperature is a key factor to improve durability of SOFCs and make these devices more competitive on the market. To do that electrocatalytic material active for desired reactions are required. Up to now cathode – side represents one of the main bottle neck that curbs SOFCs expansion. Then, the development of electrocatalytic material active for oxygen reduction reaction and stable for a long time at temperature below 700 °C is a must.

$La_{1-x}Sr_xMnO_3$ is extremely suitable for its stability and it remains the state of art for high temperature cells; nevertheless, at the intermediate range if used alone is not able to provide a sufficient catalytic activity.

More performing materials at 500 – 700 °C are mixed ionic and electronic conductor (MIEC), extending the active surface available for ORR far from the three phase boundary at electrode/electrolyte interface. Among these materials ($La_{0.8}Sr_{0.2}FeO_3$, $La_{0.8}Sr_{0.2}CoO_3$, $La_{0.6}Sr_{0.4}CoO_{3-\delta}$), many efforts were focused on $La_{1-x}Sr_xFe_{1-y}Co_yO_{3-\delta}$ (LSCF) and $Ba_{0.5}Sr_{0.5}Co_{0.8}Fe_{0.2}O_{3-\delta}$ (BSCF) (14, 31). The first have an extraordinary ionic conductivity, the latter has one of the most active oxygen surface activity ever reported in literature (25, 31).

Unfortunately the outstanding catalytic properties of LSCF and BSCF are not followed by stability during the time. Problems related with LSCF are mostly linked with reactions at cathode/electrolyte interface, when YSZ is used as electrolyte. La and Sr interdiffusion through YSZ occurs, forming less conductive phases such as $La_2Zr_2O_7$ or $SrZrO_3$. On the other hand BSCF is affected by a structural instability below 900 °C, with a phase transition from cubic to hexagonal structure characterized by a lower catalytic activity (32).

An important puzzle piece in material optimization is occupied by technique used to investigate electrode behavior. Electrochemical Impedance Spectroscopy (EIS) is largely employed because of it is not a destructive test and for the large amount of information obtainable. In fact it is possible to analyze EIS data with proper models like distribution of relaxation time (DRT), equivalent circuit model (ECM) or physically-based model extrapolating material parameters.

Based on this considerations this thesis presents results about improvement of performance and stability of well – known cathode materials (LSM, LSCF, BSCF), and at the same time particular attention has been paid on tools for EIS interpretation. The work is divided in four main chapters summarized here:

- Chapter 2 deals with Electrochemical Impedance Spectroscopy and on its basis. After a brief introduction, attention is focused on models to analyze EIS measurement. Distribution of relaxation time (DRT) and Equivalent Circuit Modeling (ECM) are introduced, with a particular interest for characteristic frequency determination.

- Chapter 3 faces a revaluation of LSM as cathode material. In fact, experimental section shows a kinetic transition driven by the applied overpotential. Electrode change from a surface path (well-known for electronic conductors) to a bulk path (typical of MIEC conductors). This hypothesis is confirmed by a physically-based model. Then, these results show a new way to exploit LSM and a first application is proposed in the second part of this Chapter, where LSM is used as infiltrated gent on LSCF and BSCF scaffold to stabilize their performance

- Chapter 4 presents a new route to increase LSCF and BSCF stability without renounce to performance. Two materials are mixed in different volume ratio and tested as cathode material on SDC electrolyte. During the sintering stage a phase transition occurs. Nevertheless obtained new electrodes work better than two commercial reference material, with very promising performance. Also degradation tests highlight an improvement in stability.

- Chapter 5 reports results obtained for thin film electrodes made by $La_{0.6}Sr_{0.4}FeO_3$ and $La_{0.6}Ba_{0.4}CoO_3$ and their mixtures, using a single layer and bi-layer electrode system. Electrode are deposited by Pulse Laser Deposition (PLD) technique. The interaction between LSF and LBC is strong with the formation of a new perovskite phase which is more active than two reference materials

1.4 References

1. P. Arunkumar, U. Aarthi, S. Rengaraj, C. S. Won and M. S. B. Krishna, *Nanomaterials and Energy*, 8, 1 (2019).
2. K. Chen and S. P. Jiang, *Journal of The Electrochemical Society*, 163, F3070 (2016).
3. N. Mahato, A. Banerjee, A. Gupta, S. Omar and K. Balani, *Progress in Materials Science*, 72, 141 (2015).
4. S. J. Cooper and N. P. Brandon, 1 (2017).
5. Y. Zheng, J. Wang, B. Yu, W. Zhang, J. Chen, J. Qiao and J. Zhang, *Chemical Society Reviews*, 46, 1427 (2017).
6. https://www.doitpoms.ac.uk/tlplib/fuel-cells/printall.php, in.
7. W. H. Kan, A. J. Samson and V. Thangadurai, *Journal of Materials Chemistry A*, 4, 17913 (2016).
8. P. S. Manning, J. D. Sirman, R. A. De Souza and J. A. Kilner, *Solid State Ionics*, 100, 1 (1997).
9. M. Sahibzada, B. C. H. Steele, D. Barth, R. A. Rudkin and I. S. Metcalfe, *Fuel*, 78, 639 (1999).
10. M. Sahibzada, B. C. H. Steele, K. Zheng, R. A. Rudkin and I. S. Metcalfe, *Catalysis Today*, 38, 459 (1997).
11. M. Sahibzada, B. C. H. Steele, K. Hellgardt, D. Barth, A. Effendi, D. Mantzavinos and I. S. Metcalfe, *Chemical Engineering Science*, 55, 3077 (2000).
12. F. Tietz, Ionics, 5, 129 (1999).
13. V. V. Kharton, F. M. Figueiredo, L. Navarro, E. N. Naumovich, A. V. Kovalevsky, A. A. Yaremchenko, A. P. Viskup, A. Carneiro, F. M. B. Marques and J. R. Frade, *Journal of Materials Science*, 36, 1105 (2001).

14. S. Sameshima, T. Ichikawa, M. Kawaminami and Y. Hirata, *Materials Chemistry and Physics*, 61, 31 (1999).

15. H. Ullmann, N. Trofimenko, F. Tietz, D. Stöver and A. Ahmad-Khanlou, *Solid State Ionics*, 138, 79 (2000).

16. J. W. Fergus, *Journal of Power Sources*, 162, 30 (2006).

17. S. Wang, T. Kato, S. Nagata, T. Kaneko, N. Iwashita, T. Honda and M. Dokiya, *Solid State Ionics*, 152-153, 477 (2002).

18. S. P. Jiang and S. H. Chan, *Journal of Materials Science*, 39, 4405 (2004).

19. W. Z. Zhu and S. C. Deevi, *Materials Science and Engineering*: A, 362, 228 (2003).

20. C. Sun and U. Stimming, *Journal of Power Sources*, 171, 247 (2007).

21. A. J. Jacobson, *Chemistry of Materials*, 22, 660 (2010).

22. A. Fuerte, R. X. Valenzuela, M. J. Escudero and L. Daza, *Journal of Power Sources*, 196, 4324 (2011).

23. J. Fleig, *Annual Review of Materials Research*, 33, 361 (2003).

24. A. Giuliano, M. P. Carpanese, M. Panizza, G. Cerisola, D. Clematis and A. Barbucci, *Electrochimica Acta*, 240, 258 (2017).

25. Z. Shao and S. M. Haile, *Nature*, 431, 170 (2004).

26. Y. Li, R. Gemmen and X. Liu, *Journal of Power Sources*, 195, 3345 (2010).

27. C. Endler-Schuck, J. Joos, C. Niedrig, A. Weber and E. Ivers-Tiffée, *Solid State Ionics*, 269, 67 (2015).

28. A. Y. Zuev, A. N. Petrov, A. I. Vylkov and D. S. Tsvetkov, *Journal of Materials Science*, 42, 1901 (2007).

29. E. V. Tsipis, E. A. Kiselev, V. A. Kolotygin, J. C. Waerenborgh, V. A. Cherepanov and V. V. Kharton, *Solid State Ionics*, 179, 2170 (2008).

30. Z. Lu, J. Hardy, J. Templeton and J. Stevenson, *Journal of Power Sources*, 196, 39 (2011).

31. W. Araki, Y. Arai and J. Malzbender, *Materials Letter*s, 132, 295 (2014).

32. Z. Yáng, J. Martynczuk, K. Efimov, A. S. Harvey, A. Infortuna, P. Kocher and L. J. Gauckler, *Chemistry of Materials*, 23, 3169 (2011)

CHAPTER 2

Electrochemical Impedance Spectroscopy

"With great power comes great responsibility"

HIGHLIGHTS

- *Electrochemical Impedance Spectroscopy (EIS) as a powerful tool for SOFC material investigation*
- *Importance to find reliable methods to model experimental EIS data*
- *Distribution of Relaxation Times (DRT) and Equivalent Circuit Model (ECM): two approaches to evaluate processes involved in electrode kinetic*

2.1 Electrochemical impedance spectroscopy – Basic principles

Electrochemical Impedance Spectroscopy (EIS) is a widespread technique used to characterize electrode process in several field. In SOFC system analysis is extremely used to optimize this kind of electrochemical device at different length scales. A possible optimization routine for EIS application is reported in (1)

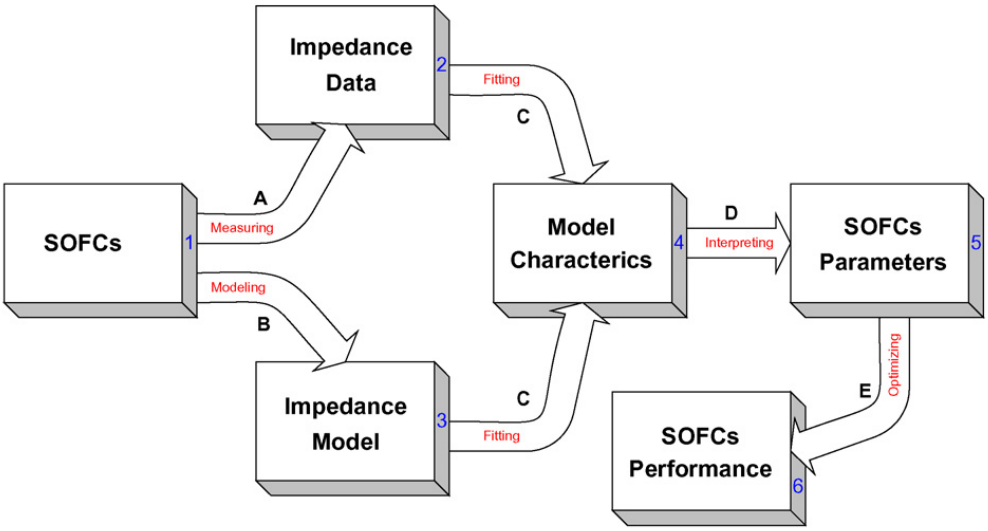

Fig. 2. 1 Flow diagram of EIS diagnosis for SOFC (1)

A strength of this method is that it is non-destructive and preserve system conditions. Impedance measurements are made in the time domain applying a small amplitude sinusoidal perturbation of potential to an electrochemical system measuring the output response of current. The first point is the selection of a working point on the polarization curve, which is the steady-state current response as a function of the applied potential (Fig. 2. 2).

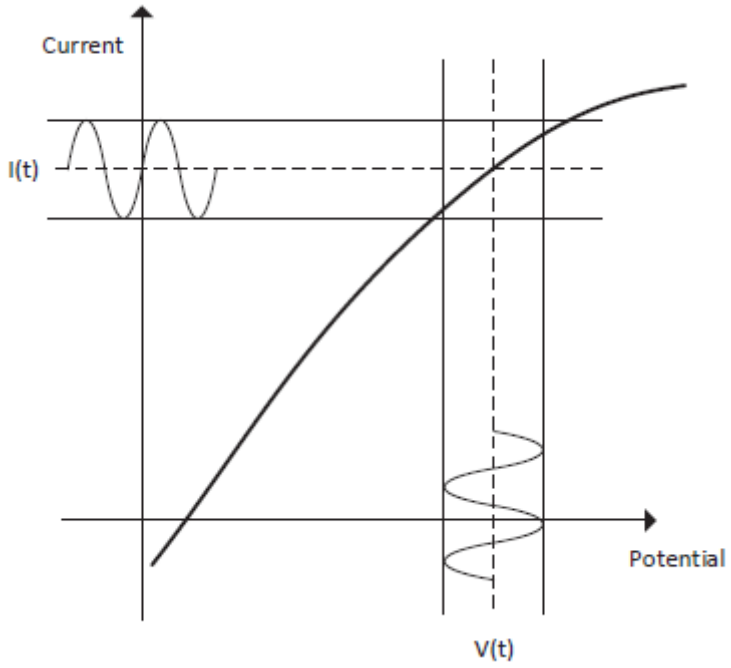

Fig. 2. 2 Polarization curve with a selected working point at steady state and the applied sinusoidal perturbation (2)

The sinusoidal perturbation is applied in a range of frequencies and the measured output provides the impedance results. The input signal is represented by:

$$V(t) = \bar{V} + |\Delta V|\cos(\omega t) \quad (2.1)$$

then the corresponding output is

$$I(t) = \bar{I} + |\Delta I|\cos(\omega t + \varphi) \quad (2.2)$$

$\bar{V}$ and $\bar{I}$ are the steady terms, $|\Delta V|$ and $|\Delta I|$ are the magnitude of the oscillating part of the part, ω is the angular frequency, φ is the phase lag and t the time. As introduced above, the magnitude of oscillation must be small, to have a linear response and the same form of the input and occur at the same frequency. Then, the output response is a complex quantity, with real and imaginary parts, function of frequency, and impedance is defined as the ratio of potential and current as reported in Eq. 2.3:

$$Z(\omega) = \frac{\tilde{V}(\omega)}{\tilde{I}(\omega)} = Z_{re} + jZ_j \quad (2.3)$$

Where Z_{re} and Z_j are the real and imaginary parts of the impedance, $\tilde{V}(\omega)$ and $\tilde{I}(\omega)$ are called phasors and are complex quantities function of frequency but independent of time defined as:

$$\tilde{V}(\omega) = |\Delta V|\exp(j\varphi_V) \tag{2.4}$$

$$\tilde{I}(\omega) = |\Delta \mathrm{I}|\exp(j\varphi_I) \tag{2.5}$$

and the phase difference between the potential and current is $\varphi = \varphi_V - \varphi_I$.

Impedance data are complex values and usually presented in a complex plane, called Nyquist plot (Fig. 2. 3 (a)), which reports the real part on the x-axis and imaginary part of impedance on the y-axis. Each point represents a different frequency measurement. To show the impedance directly as a function of frequency, Bode plot (Fig. 2. 3 b) is used, reporting the magnitude (blue line) and the phase angle (black line), respectively:

$$|Z| = \sqrt{Z_{Re}^2 + Z_j^2} \tag{2.6}$$

$$\varphi = tanh^{-1}\left(\frac{Z_j}{Z_{Re}}\right) \tag{2.7}$$

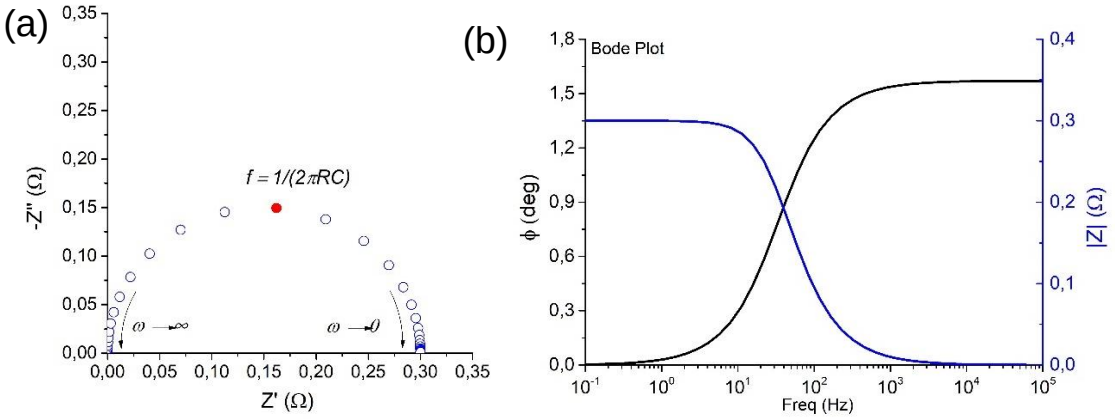

Fig. 2. 3 Example of **(a)** Nyquist plot and **(b)** Bode plot for impedance data corresponding to a RC circuit

2.2 Modeling electrochemical impedance spectroscopy

2.2.1 Basic and general concepts

Interpretation of EIS measurements can provide many information regarding processes involved in electrode kinetic, but their identification and separation can result extremely complicated. As reported in Fig. 2. 4, many phenomena occurs inside an electrochemical cell and their time scale are overlapped, and their evaluation it is not trivial. Based on literature (3-5) it is possible to define some frequency range and the related processes as proposed below:

$10^3 \div 10^4$ Hz: fuel electrode charge transfer

$10^2 \div 10^3$ Hz: oxygen and fuel electrode transport processes

$10^1 \div 10^2$ Hz: gas conversion

$10^0 \div 10^1$ Hz: gas conversion

$10^{-1} \div 10^0$ Hz: oxygen electrode adsorption/desorption

The number of cell parameters and operating variables involved makes extremely complicated the direct description of a process only through peak frequency, but this kind of analysis can help to localized frequency region of main phenomena and then to build some preliminary hypothesis.

In the following part of this chapter the most common approaches to modeling electrochemical impedance spectroscopy will be introduced. Moreover, in the last part of this Chapter a possible integration and coupling among different methods will be introduced

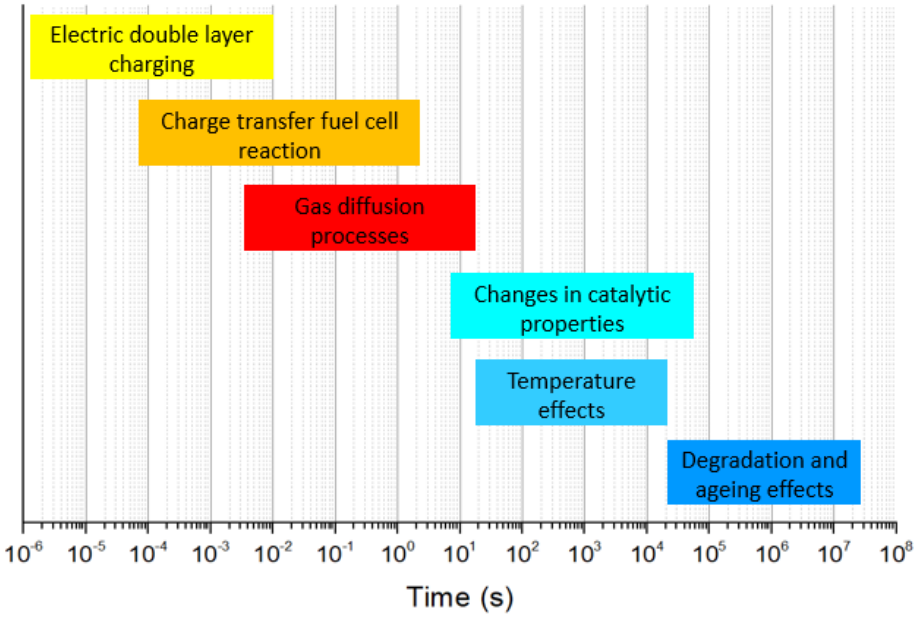

Fig. 2. 4 Characteristic time domain range for processes involved in a SOFC. Adapted from (6)

2.2.2 Equivalent circuit

Impedance measurements can be described as a composition of electrical elements, named equivalent circuit modeling. Here the description of the equivalent circuit elements used in this thesis has been reported, such as resistance, capacitance, constant phase element and Gerischer element.

Resistor: it is used to describe ohmic resistance related to electronic and ion conduction. The impedance of resistor is made by only real part as:

$$Z_R = R \qquad (2.8)$$

Capacitor: it is usually used to describe a double layer capacitance at electrode/electrolyte interface. Nevertheless when this parameter assume larger values [C >10^{-4} 10^{-3} F cm^{-2}] it is no longer related with the formation of a double layer, but it is associated to the charge stored in bulk electrode, in particular as oxygen vacancies. In this case, it is defined as *chemical capacitance* and represents a quantitative measure of the capability of the material of storing such charges (7). Capacitor impedance is described by imaginary part as:

$$Z_C = \frac{1}{j\omega C} \quad (2.9)$$

Constant phase element (CPE): to better described the response of a real electrode and its distribution of frequency, constant phase element has been introduced and its impedance expression is given by:

$$Z_Q = \frac{1}{(j\omega)^n Q} \quad (2.10)$$

In most of cases resistance is used in parallel with capacitance or constant phase element as reported in Fig. 2. 5 (a) and (b), respectively.

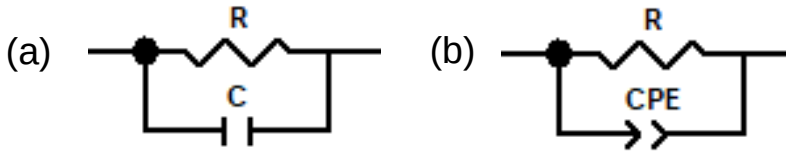

Fig. 2. 5 (a) RC circuit element **(b)** RQ circuit element

These circuit configurations can described interfacial processes of electrochemical systems. RC circuit is represents by a semicircle in Nyquist plot, as in Fig. 2. 6. Generally, data are reported to have frequency decreasing from the left to the right side and the semicircle peak is characterized by a time constant $\tau = RC$ which is the inverse of angular frequency $\omega = 2\pi f$

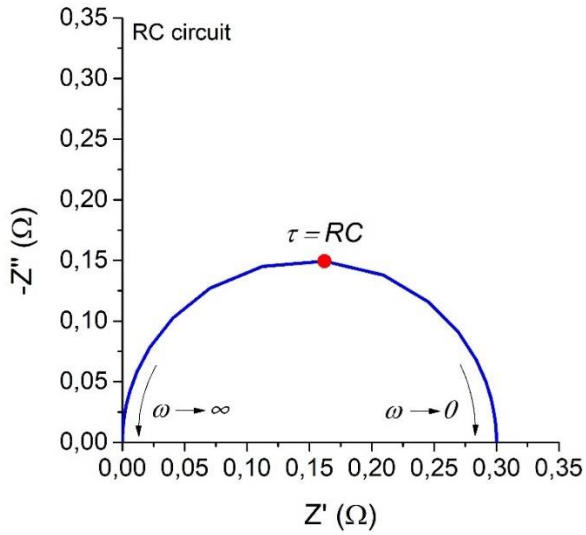

Fig. 2. 6 Nyquist plot of a RC circuit

RQ circuit element has the same behavior of RC circuit when the exponent of CPE element is n = 1, otherwise its shape change as function of these parameter as reported in Fig. 2. 7

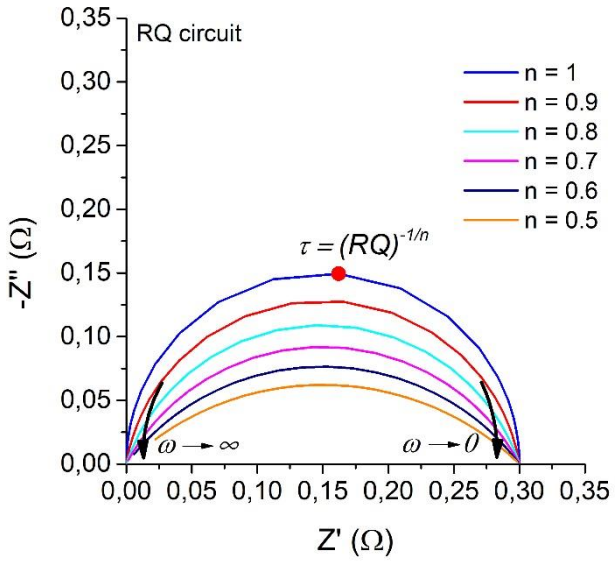

Fig. 2. 7 Nyquist plot of a RQ circuit for different value of n

Another important element used in equivalent circuit analysis is the *Gerischer impedance*, used especially to model electrode behavior for mixed ionic and electronic conductor (8-10). In case of porous MIEC cathode with a good electronic conductivity (such as LSCF) electrode impedance is mainly controlled by oxygen surface exchange and solid-state oxygen ion diffusion. Adler et al. (11) derived the following impedance expression to described an electrode dominated by this two processes:

$$Z_G(\omega) = \frac{R_{chem}}{\sqrt{1+j\omega t_{chem}}} \tag{2.11}$$

Where R_{chem} and t_{chem} are a characteristic resistance and time constant respectively, related to surface kinetic and transport properties of material and defined as:

$$R_{chem} = \left(\frac{RT}{2F^2}\right)\sqrt{\frac{\tau_s \cdot \gamma_{TD}^2}{(1-\varepsilon)\cdot a_s \cdot C_{mc}^2 \cdot k^{\delta} \cdot D^{\delta}}} \tag{2.12}$$

$$t_{chem} = \frac{c_v(1-\epsilon)}{Aar_0(\alpha_f+\alpha_b)} \tag{2.13}$$

Where ε a_s and τ_s are the porosity, electrochemical active surface area and solid-phase tortuosity, respectively. C_{mc} the concentration of oxygen lattice sites, δ the fraction of oxygen vacancies and γ_{TD} is the called thermodynamic enhancement factor. $k^{\delta}$and D^{δ} are the oxygen surface exchange and chemical diffusion coefficient, respectively. c_v is the oxygen vacancies concentration, ε is the porosity, A the thermodynamic factor, a the surface area, r_0 the exchange neutral flux density and finally α_f and α_b are the constants of order od unit that depend on the specific mechanism of the exchange reaction.

Gerischer impedance has a characteristic shape on Nyquist plot called “drop curve” as illustrated in Fig. 2. 8.

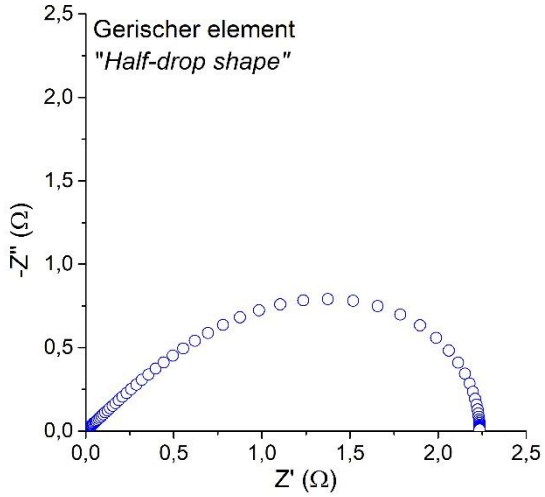

Fig. 2. 8 Nyquist plot of Gerischer element

2.2.3 Complex Nonlinear Least Squares (CNLS) fit

Elements and circuits proposed above can be properly combined to describe impedance measurements by means of Equivalent Circuit Model (ECM). The choice of circuit needed to maintain a physical meaning. To determine EC parameters a fitting algorithm is required, and one of the most diffuse is Non – linear Last Squares (NLS) fitting algorithm. Fit procedure operates in order to find a set of fit parameter able to minimize the sum:

$$Sum = \sum_{k=1}^{n} w_k \left[\left(Z_{k,r} - Z'_{k,r}(\omega) \right)^2 + \left(Z_{k,j} - Z'_{k,j}(\omega) \right)^2 \right] \qquad (2.14)$$

where subscript *k* are referred to *k-th* data point in impedance plot, and $Z_{k,r}$ and $Z'_{k.r}$ are the real part of the experimental impedance and the theoretical prediction of the real part of EIS response, respectively. $Z_{k,i}$ and $Z'_{k.r}$ are the same quantity attributed to imaginary part. w_k is a weighting factor.

CNLS algorithm requires an initial estimation of fit parameters and then the target function is minimized as proposed by Eq. (2.7) In Fig. 2. 9 are reported an example of fit through an equivalent circuit. EC used is made by R_0, a pure ohmic resistance identified by the shifting along x-axis, and two RQ subcircuit. CNLS fit allows to extrapolate parameter values, obtaining information regarding identified processes and decoupling in the $(RQ)_i$ curves (dash curves in Fig. 2. 9)

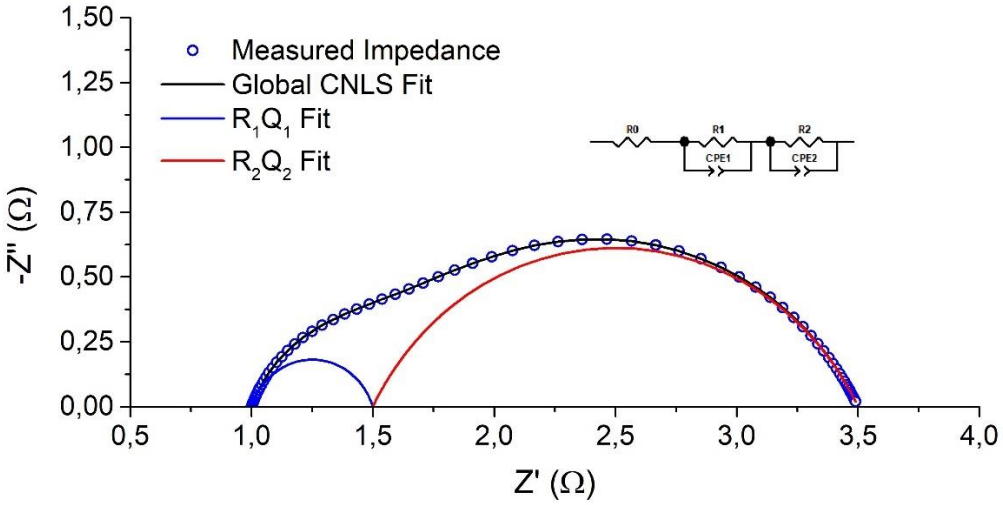

Fig. 2. 9 CNLS fit results of EIS measurement

2.2.4 Distribution of Relaxation Time (DRT)

Distribution of Relaxation Time (DRT) is a useful technique able to separates processes with different time constants directly impedance measurements by means a mathematical treatment of experimental data (12-14). Then, this approach allows to extrapolate preliminary information regarding processes without physical assumption. The principle at the basis of DRT is that impedance data can be represented as sum of infinitesimal RC-elements as reported in Fig. 2. 10.

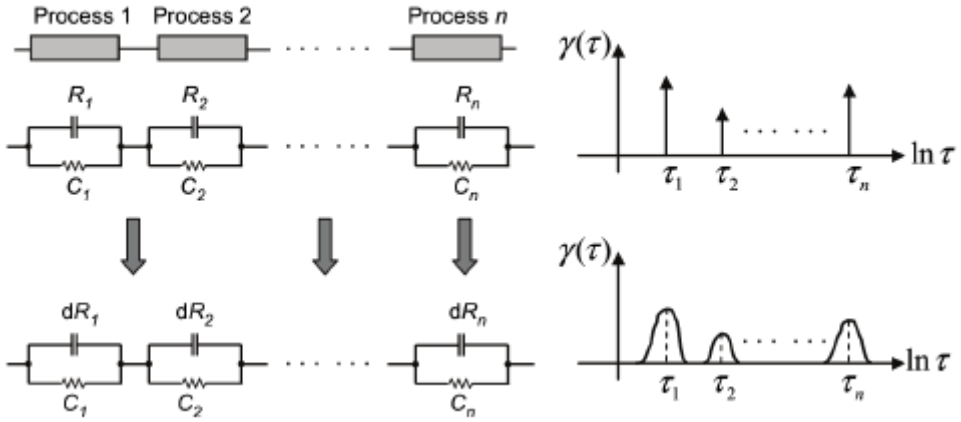

Fig. 2. 10 Interpretation of EIS data in terms of equivalent circuit models and DRT

Impedance can be expressed by an integral containing the approximated distribution function *γ(τ)* which satisfies Eq. 2.15

$$Z_{DRT}(\omega) = R_s + R_P \int_0^{\infty} \frac{\gamma(\tau)}{1+j\omega\tau} d\tau \qquad (2.15)$$

$$\int_0^{\infty} \gamma(\tau)\, d\tau = 1 \qquad (2.16)$$

where R_s represents the ohmic resistance and R_P is the total polarization resistance. The ratio $\gamma(\tau)/(1 + j\omega\tau)$ is the fraction of the global electrode resistance with relaxation time between τ and $\tau + d\tau$. Thus, the DRT method consists in solving integral Eq. 2.16 with respect to the unknown function $\gamma(\tau)$. As a consequence area under peak is equal to the polarization resistance of the corresponding process (15).

For practical reasons the integral of Eq. 2.15 is approximated by a discrete function as reported here:

$$Z(\omega) = R_s + R_P \sum_{n=1}^{N} \frac{\gamma_n}{1+j\omega\tau_n} \quad (2.17)$$

Nevertheless, resolution of DRT curve from EIS data, which are affected by noise, is an ill-posed problem. An ill-posed problem is a mathematical definition meaning that at least one of these requirements is not fulfilled:

- solution of equation is stable with respect to small changes in the known terms;
- equation has solution and it is unique.

The first condition is not respect, because the noise of impedance data is sufficient to make DRT solution unstable. Then, to find solution of an ill-posed problem solution regularization method have been developed, and the most well-known is the Tikhonov method (16-18).

Tikhonov regularization is based on to change the initial ill-posed problem in a well-posed problem but dependent by a numeric parameter λ, called *coefficient of regularization*. In the case of coefficient of regularization and errors in the observed data tend to zero in accordance, the solution of the new well-posed problem tends to the exact solution of the corresponding incorrect problem (19)

$$\boldsymbol{x}_\lambda = (A^T A + \lambda I)^{-1} A^T \boldsymbol{b} \quad (2.18)$$

The choice of the coefficient of regularization has a strong influence on problem solution. Indeed, λ affect solution of Eq. 2.18; for a too low value ($\lambda \rightarrow 0$) the noise grow up its weight in solution. On the other hand, increasing λ value decreases the noise but leads to a losses of information. Therefore, it is fundamental to find the optimal λ (λ_{opt}) defined as the value for which the smallest deviation is achieved between the theoretical function of DRT and the function obtained from solving Eq. 2.18,

$$\lambda_{opt} = \min_{0<\lambda<\infty} \left(\sum_i (\gamma_{exact}(\tau_i) - \gamma_\lambda(\tau_i))^2\right) \quad (2.19)$$

where γ_{exact} is the theoretical DRT, γ_λ is the DRT calculated for the given λ. The approach proposed above is not applicable because it requires to know the exact solution of Eq. 2.18 based only measured data.

A possible approach to find regularization coefficient is the L-curve method (19). It is based on a plot which reports the second order norm of the regularized solution ($\|x_\lambda\|_2$) as a function of the second norm of the corresponding residual ($\|Ax_\lambda - b\|_2$) for different values of the regularization parameter. Fig. 2. 11 illustrates the characteristic plot used to evaluate λ properly. In fact, the corner identified separation between two different regions: in the first the solution is dominated by regularization error, in the second one data errors are the main contribution.

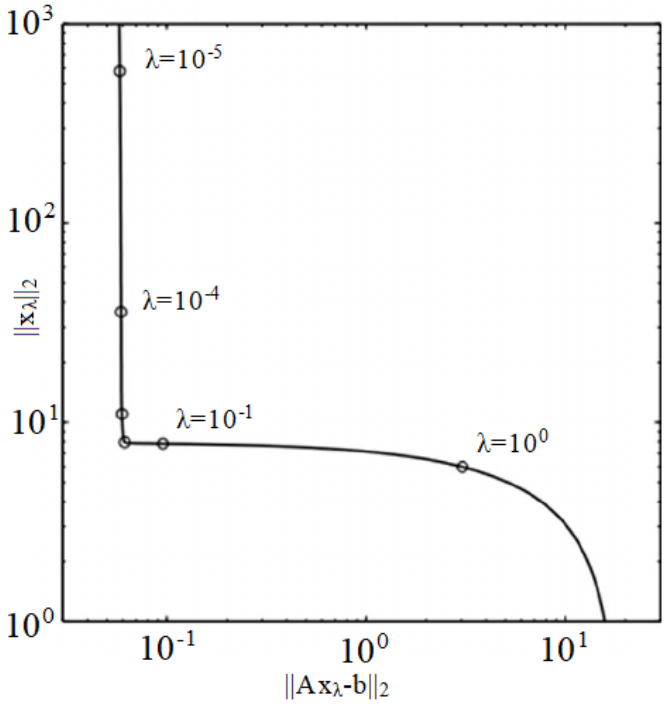

Fig. 2. 11 Example of L-curve to find λ optimal value

2.3 DRT and EC analysis – Handle with care

Two methods introduced above, DRT and EC, are powerful tools to gain information about electrode kinetic. They must be used take care for results interpretation, because of there are several error sources. In EC analysis the choice of the circuit can lead to a wrong interpretation of phenomena, while DRT peaks separation

is not always trivial. In this section some problems will be faced looking a useful integration between the methodologies.

The discussion is divided in two sections:

i. the first deals with impedance analysis of equivalent circuit made by a RQ circuit (Fig. 2. 12 (a)) considering the influence of n-parameter on frequency distribution.

ii. the second section takes into account a $(RQ)_1(RQ)_2$ circuit (Fig. 2. 12 (b)).

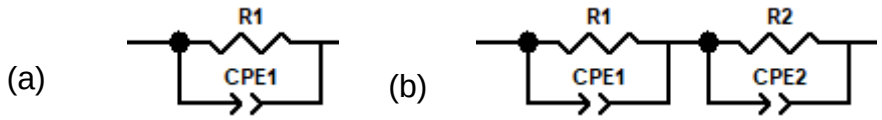

Fig. 2. 12 Equivalent circuit used to simulate impedance spectra

- RQ circuit

RQ equivalent circuit is characterized by an impedance spectra as reported in Fig. 2. 7. The diameter of arc is fixed by resistance value that remains constant for all EIS simulation. The curves differ for n-parameter value, while other parameters remain constant (R_1 = 0.3 Ω; Q_1 = 0.015 F s^{n-1}); its increasing leads to a depression of arc. Parameter "n" is included from 0 to 1, but in this case the range 0 ÷ 0.5 has been considered because describes two important limit behaviors. For n = 1, CPE is an ideal capacitor, while n = 0.5 represents a Warburg process.

Fig. 2. 13 shows the corresponding DRT curve for RQ circuit reported in Fig. 2. 7. For n = 1, curve has a symmetric peak; moving at n = 0.5, frequency distribution becomes more spread and progressively lost symmetry, meaning that a diffusive process could be recognizable by a wider DRT curve. Then, the presence of diffusion phenomena, can caused a more complicated identification of characteristic frequency of process (f_c) (Fig. 2. 14). A small deviation from expected value is already observable in this simple case. Fig. 2. 14 compares DRT curve with Bode representation, and reports on the DRT curves the

characteristic frequency of RQ circuit calculated. For n = 1 and 0.8 DRT is able to identified the frequency in accordance with expected value (and Bode diagram); for low n-value DRT recognized a larger range close the real peak value.

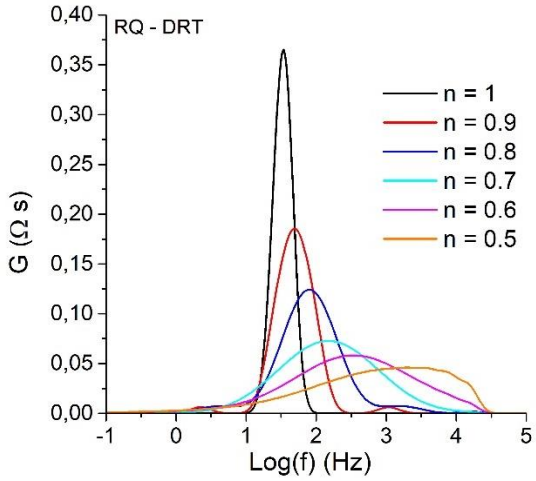

Fig. 2. 13 DRT curves for RQ circuit for different n-value

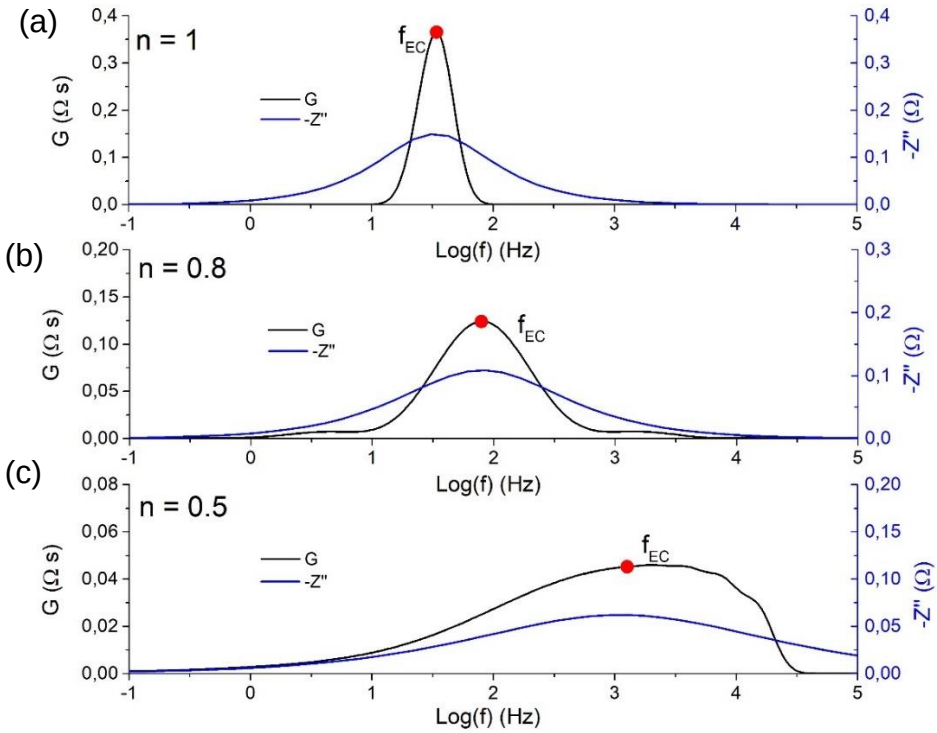

Fig. 2. 14 Comparison between Bode plot and DRT curve for 3 n-parameters

- $(RQ)_{HF}(RQ)_{LF}$ circuit

Identification of characteristic frequency becomes more complicated increasing number of processes involved. In this paragraph impedance spectra obtained with a $(RQ)_{HF}(RQ)_{LF}$ are analyzed. Simulated measurements are obtained change n-parameter of CPE at lower frequency (n_{LF}), while other parameters remain constant (R_{HF} = 0.4 Ω; Q_{HF} = 0.05 F s^{n-1}; n_{HF} = 1; R_{LF} = 1 Ω; Q_{LF} = 0.2 F s^{n-1}). Then, if HF process is considered as an ideal capacitance, the second changes is nature from capacitive to diffusive nature.

The effects of this change on impedance curves are well visible in Fig. 2. 15 (a – f). For n=1 the presence of at least two processes is recognizable directly from EIS curves. Decreasing the n-value of $(RQ)_{LF}$, separation of two processes is less trivial and application of DRT can help to make some preliminary hypothesis.

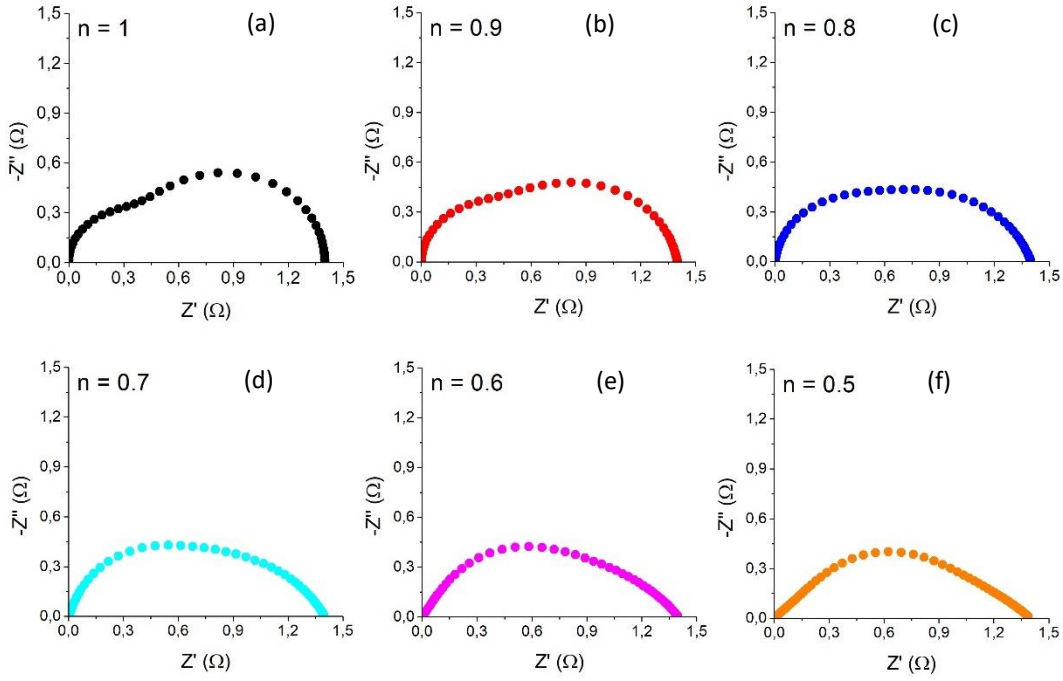

Fig. 2. 15 Impedance curves for $(RQ)_{HF}(RQ)_{LF}$ varying CPE n-parameter for $(RQ)_{LF}$ circuit. (Circuit parameters: R_{HF} = 0.4 Ω; Q_{HF} = 0.05 F s^{n-1}; n_{HF} = 1; R_{LF} = 1 Ω; Q_{LF} = 0.2 F s^{n-1})

Fig. 2. 16 compares Bode plot with DRT curve for different CPE n-parameter values. Moreover, on DRT curves expected characteristic frequency of two subcircuits are reported. In Fig. 2. 16 (a), both CPE – n are equal to 1, and Bode plot well highlights only the peak of $(RQ)_{LF}$. This peak is in agreement with the expected one and with the main DRT peak. On the other hand, in Bode's representation the second process is hidden (there is only a slight shoulder close to 10 Hz as expected). The second capacitive process $(RQ)_{HF}$ is well recognized by DRT measure with a symmetric peak centered on f_{RQ}^{HF}.

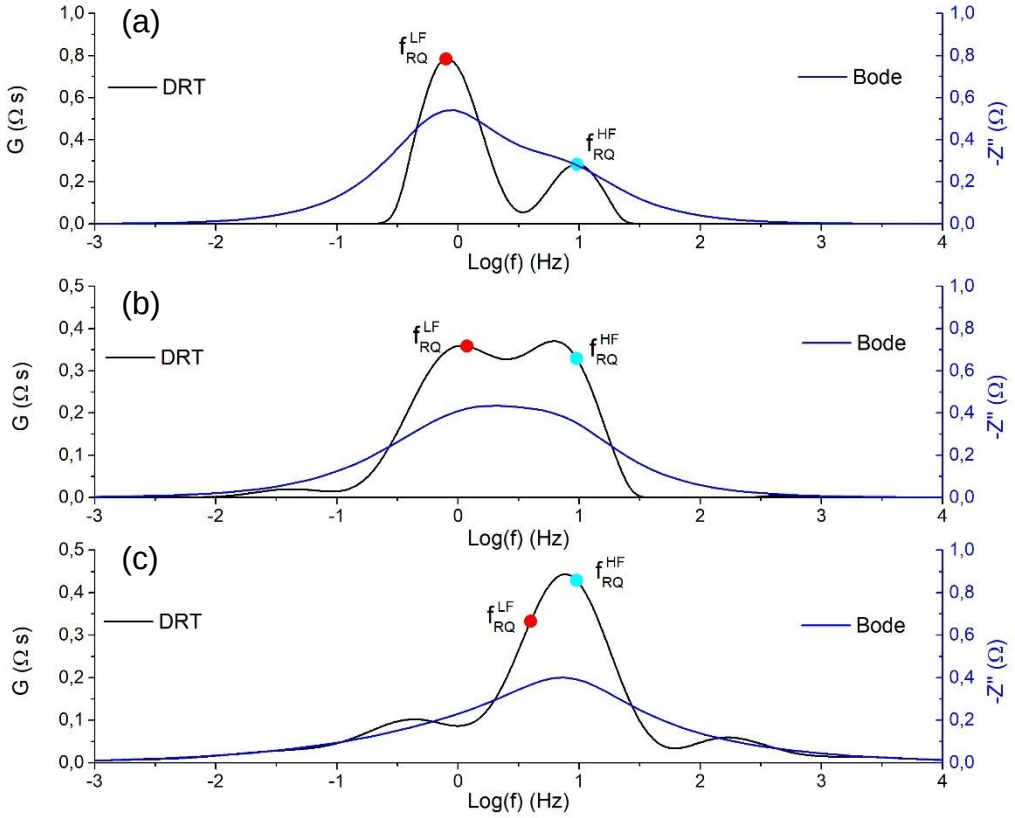

Fig. 2. 16 Comparison of Bode plot (blue line), DRT curves (Black line) and expected characteristic frequency for the two processes at different CPE n-parameter (n_{LF}) values **(a)** n_{LF} = 1; **(b)** n_{LF} = 0.8; **(c)** n = 0.5;

The decreasing of $(CPE - n)_{LF}$ to simulate the introduction of diffusive process complicates their separation (Fig. 2. 16 (b) – (c)). Fig. 2. 16 (b) show that for CPE – n =0.8, Bode's plot peak has a large frequency distribution, but not make possible process separation. Their identification becames possible using DRT, with two clear peaks; nevertheless also in this case the results (determination of f_{RQ}^{HF} and f_{RQ}^{LF}) are affected by n-parameter, introducing a deviation from expected values as introduce above for one single circuit.

An accurate determination of characteristic frequency is harder when CPE – n = 0.5 (Fig. 2. 16 (c)). Previously, in single RQ circuit section, it has been introduced how such n-value can influence frequency distribution. Then, a so wider frequency distribution for $(RQ)_{LF}$ can dramatically alters the distribution of the other one, which maintains a constant behavior.

Therefore, results presented here, about simulated impedance spectra, are useful to underline the task that DRT could have in EIS interpretation and its limit. In fact, it can provide additional information than Bode plot, without requesting physical assumption due to its sensitivity, however it can be handle with care to avoid a wrong system interpretation. Information extrapolated can be used to elaborate an appropriate equivalent circuit or a physically-based model.

2.4 References

1. Q.-A. Huang, R. Hui, B. Wang and J. Zhang, *Electrochimica Acta*, **52**, 8144 (2007).
2. M. S. Harding, Mathematical Models for Impedance Spectroscopy, in, University of Florida (2017).
3. A. Kromp, Model-based Interpretation of the Performance and Degradation of Reformate Fueled Solid Oxide Fuel Cells, in, Karlsruher Institut fur Technologie (2013).
4. M. Kornely, A. Neumann, N. H. Menzler, A. Weber and E. Ivers-Tiffée, *ECS Transactions*, **35**, 2009 (2011).
5. Z. Wuillemin, Y. Antonetti, C. Beetschen, O. Millioud, S. Ceschini, H. Madi and J. Van herle, *ECS Transactions*, **57**, 561 (2013).
6. Wagner, Theory and Application of Electrochemical Impedance Spectroscopy for Fuel Cell Characterization, in.
7. J. Jamnik and J. Maier, *Physical Chemistry Chemical Physics*, **3**, 1668 (2001).
8. L. Almar, J. Szász, A. Weber and E. Ivers-Tiffée, *Journal of The Electrochemical Society*, **164**, F289 (2017).
9. M. B. Effat and F. Ciucci, *Electrochimica Acta*, **247**, 1117 (2017).
10. Y. Zhang, Y. Chen, M. Yan and F. Chen, *Journal of Power Sources*, **283**, 464 (2015).
11. S. B. Adler, J. A. Lane and B. C. H. Steele, *Journal of The Electrochemical Society*, **143**, 3554 (1996).
12. H. Schichlein, A. C. Müller, M. Voigts, A. Krügel and E. Ivers-Tiffée, *Journal of Applied Electrochemistry*, **32**, 875 (2002).
13. A. Leonide, V. Sonn, A. Weber and E. Ivers-Tiffée, *Journal of The Electrochemical Society*, **155**, B36 (2008).
14. V. Sonn, A. Leonide and E. Ivers-Tiffée, *Journal of The Electrochemical Society*, **155**, B675 (2008).
15. A. Leonide, SOFC Modelling and Parameter Identification by means of Impedance Spectroscopy, in, Karlsruher Institute fur Technologie (2010).

16. A. L. Gavrilyuk, D. A. Osinkin and D. I. Bronin, *Russian Journal of Electrochemistry*, **53**, 575 (2017).
17. F. Ciucci and C. Chen, *Electrochimica Acta*, **167**, 439 (2015).
18. A. Mertens and J. Granwehr, *Journal of Energy Storage*, **13**, 401 (2017).
19. D. Calvetti, S. Morigi, L. Reichel and F. Sgallari, *Journal of Computational and Applied Mathematics*, **123**, 423 (2000).

CHAPTER 3

LSM as cathode for IT-SOFC: A second chance?*

HIGHLIGHTS

- *$La_{0.8}Sr_{0.2}MnO_{3-x}$ electrodes were sintered at different temperature to obtained different morphology*
- *Electrochemical impedance measurements show a kinetic transition from surface path to a bulk for oxygen reduction reaction as a function of applied overpotential*
- *Geometric Index was introduced to explain kinetic regime transition from a morphological point of view*
- *Physically-based model confirmed the change in kinetic regime*
- *LSM material was applied as infiltrated phase in LSCF and BSCF cathode to increase their performance and stability*

* The content of this Chapter has been published in:

- *Solid State Ionics, Volume 301, 2017, Pages 106-115*
- *Solid State Ionics, Volume 303,2017, Pages 181-190*
- *Journal of Electrochemical Society, Volume 164(10), 2017, pages F3114-F3122*

3.1 Introduction

Strontium – doped Lanthanum Manganite ($La_{1-x}Sr_xMnO_{3-\delta}$) has been a valid actor as a cathode material for SOFC. Moving at intermediate and low temperature, its characteristics seem to be no longer completely exploitable, due to its lower conductivity in the range temperature now considered. New materials with a mixed ionic and electronic conductivity, such as $La_{1-x}Sr_xCo_yFe_{1-y}O_{3-\delta}$ and $Ba_{1-x}Sr_xCo_yFe_{1-y}O_{3-\delta,}$ show a higher electrocatalytic activity at temperature between 500 – 700 °C (1-8).

Now a question arises: Does LSM change its role in SOFC architecture? Up to now, this material has been used as main cathode material (backbone electrode). Can its properties be exploit using LSM in a new away, such as stabilizing material? LSM can provide key properties for oxygen electrode, and among them redox stability and compatibility with other cells components are non-negligible points.

Nevertheless, even if in literature are reported several works that support this approach showing enhanced performance and stability, it is evident the importance to completely understand LSM features under operating conditions (9-12). In fact, several different interpretations have been proposed for the reaction kinetics in LSM – based systems and a comprehensive understanding is still missing.

Works reported in literature proposed a wide choice of limiting phenomena for ORR: i) oxygen ion transfer at electrode/electrolyte interface (13), ii) adsorption and/or dissociative adsorption of oxygen at LSM surface (14), iii) first and second electron transfer (15). Literature also underlined a possible modifications in the kinetic mechanism (10) depending on cell preparation, testing conditions and preparation history.

Based on these facts this chapter faces LSM electrocatalytic behavior, with the aim to get further insight into LSM peculiarities, opening new promising solutions for the next generation of SOFC cathodes.

3.2 Experimental

The supporting electrolytes were produced by uniaxial pressing the YSZ powders (TZ-8Y Tosoh) followed by sintering at 1500 °C for 1 h. The shaping of the YSZ powder was carefully designed in order to obtain pellets with diameter equal to 35 mm and thickness equal to 3 mm after sintering. A so thick electrolyte was used to meet the geometric requirements to avoid any artefacts due to possible electrode misalignment in the impedance measurements, in agreement with indications reported by other works (16, 17).

For the electrodes deposition, a suitable screen printing ink was produced by adding the proper amount of solvent, deflocculant and binder to the $(La_{0.8}Sr_{0.2})MnO_{3-x}$ powder (LSM20-P FuelCell materials) following the procedure reported by Sanson et al. (18). Films were screen printed (squeegee speed = 0.12 m/s, squeegee load = 4.5 kgF, snap off = 0.9 mm, AUREL 900, AUREL Automation S.p.A., Italy) onto the YSZ pellets and dried at 353 K for 30 min into an infrared furnace. Suitable masks were used to print two types of cell: i) Cell-A: working electrode (WE) and counter electrode (CE) diameter equal to 3 mm; ii) Cell-B: WE and CE diameter equal to 8 mm. The films were finally sintered at temperatures of 1050 °C and 1150 °C for 2 h.

The thickness of the sintered porous LSM electrodes was in the order of 3 μm. The cells were placed inside an in-house built apparatus for the electrochemical investigation. Two platinum nets were applied on both the WE and CE electrodes surfaces in order to optimize the electrical contact. The system was heated at a rate of 0.9 K min^{-1} up to testing temperature (700-800 °C). The measurements were carried out in two and three-probe configuration, using a potentiostat coupled to a frequency response analyzer (Autolab PGSTAT302N). During the testing procedure, the cathode was exposed to ambient atmosphere or fed with pure oxygen mixed with nitrogen using mass flow meters (Bronkhorst El-flow type). Overpotential, temperature and oxygen partial pressure were modulated to approach the real operating conditions of SOFCs similarly to previous study (19, 20) without exposing the electrode to very low oxygen partial pressures. In fact, as shown by several authors (21, 22), at low oxygen partial pressure (p_{O2} value around 10^{-4} – 10^{-1} atm) Sr segregates on the LSM electrode surface,

causing the formation of oxygen vacancy with a remarkable change of the surface activity.

Impedance measurements at open circuit voltage (OCV) in a frequency range of 10^6 – 10^{-1} Hz were carried out in a potentiostatic mode. Before starting any systematic analysis, the linearity of the current response to the input voltage perturbation was checked. This was verified by ranging the voltage perturbation amplitude from 5 to 50 mV and checking that the current perturbation varied linearly with the voltage perturbation, that is, that the measured impedance was independent of the voltage perturbation amplitude. Short circuit measurements of the cell rig were performed under the same conditions of the impedance analysis and the obtained data were used to correct inductance in the impedance spectra.

A microstructural investigation of the cells both before and after testing was carried out by the SEM (LEO1450 VP Scanning Electron Microscope).

3.3 Results and discussion

3.3.1 Effects of cell geometry

Some preliminary measurements were performed on the symmetrical cells prepared with the two geometric configurations, namely Cell – A and Cell – B, in order to quantify the effect of cell geometry on the impedance results at different overpotentials. Cell – A was made according to the geometric requirements suggested in literature (16) (Fig. 3. 1):

- the working electrode (WE), diameter of 3 mm, was accurately aligned to the counter electrode (CE);
- reference electrode is co-planar around WE at a distance greater than three times the electrolyte thickness.

All the electrodes (WE, CE and RE) were made with same LSM material. As regards Cell – B, it was similar to Cell – A, but with a smaller distance between WE and RE due to the bigger WE (diameter equal to 8 mm), as illustrated in Fig. 3. 2.

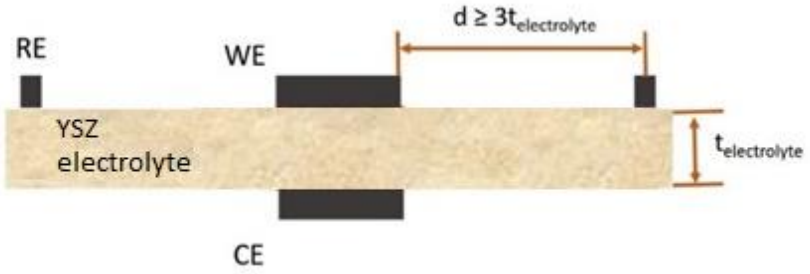

Fig. 3. 1 Sketch of cell geometry used for Cell – A

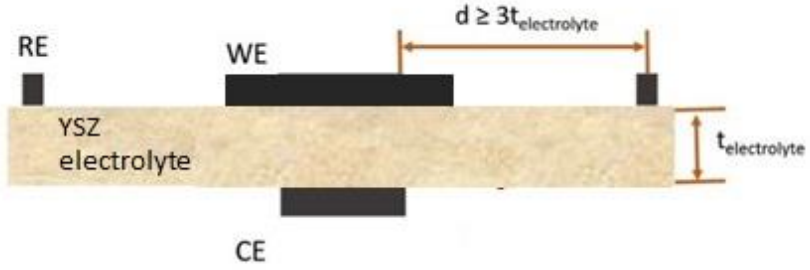

Fig. 3. 2 Sketch of cell geometry used for Cell – B

Fig. 3. 3 reports the comparison of polarization resistance (R_P) obtained in the two cell geometries. In this figure it is possible to observe that in case of OCV and for small overpotential (lower than 0.15 V), the two cells geometry (Cell – A and Cell – B) show R_P values very close each other, pointing out that it is possible to obtain reliable results with both cell geometries in such operating conditions. If the applied overpotential increases beyond 0.15 V the experimental polarization resistance measured in Cell – A and Cell – B diverge. Fig. 3. 4 shows polarization resistance obtained from further investigation on Cell – A carried out at different temperature and oxygen partial pressure. Results confirmed that the cell is effectively symmetric and that the location of the reference electrode chosen is appropriate to obtain reliable impedance measurements. In fact, the Rp values obtained in two-electrode configuration, excluding the RE, match close to values obtained with the same cell in the three – electrode configuration (using RE). Then, this comparison confirms a key factor for impedance

measurements: the distance between WE and RE must be greater than 3 electrolyte thickness in order to get reliable impedance results. Based on these results Cell – A was considered in the following sections of the study.

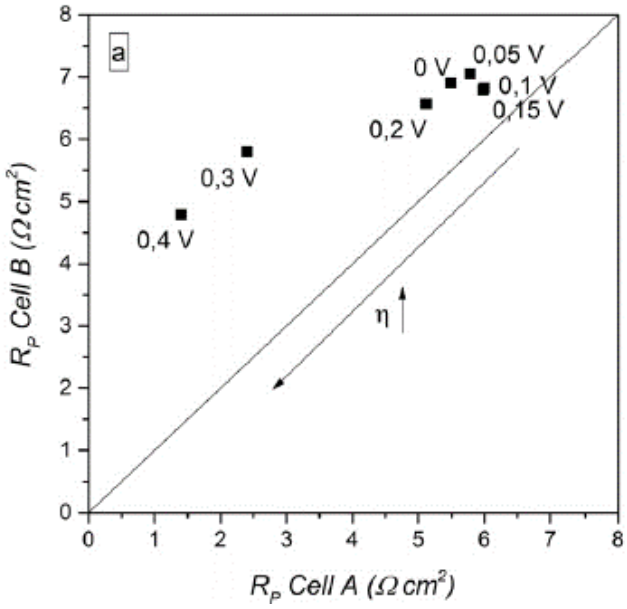

Fig. 3. 3 Comparison of polarization resistance (R_P) measured in Cell – A and Cell – B (three electrode configuration) at 700 °C, 100 % O2 and different bias (0 – 0.4 V)

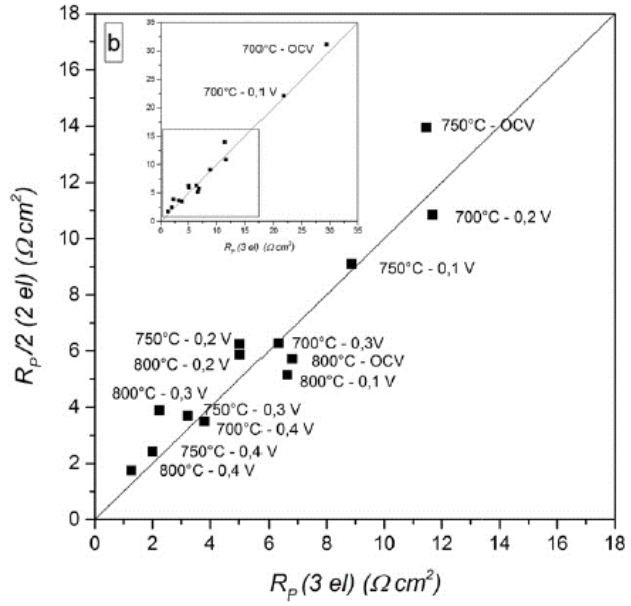

Fig. 3. 4 Comparison of polarization resistance (R_P) measured in Cell – A in two and three – electrode configuration at different temperature and oxygen partial pressure.

3.3.2 Effects of electrode microstructure

The effect of electrode microstructure was addressed by sintering porous LSM electrodes at two different temperatures, 1050 °C and 1150 °C for 2 h. The former temperature was chosen according to previous experience and supplier specification. The sintering temperature of 1150 °C was selected in order to obtain bigger particle size and smaller electrode porosity. Samples sintered at 1050 °C was characterized by a structure with an average particle size of 0.5 – 0.7 μm and a porosity around 49% (Fig. 3. 5 a). The sintering at 1150 °C led to a structure with an average particle size of 1.5 – 2 μm and a porosity of ~ 34% (Fig. 3. 5 b).

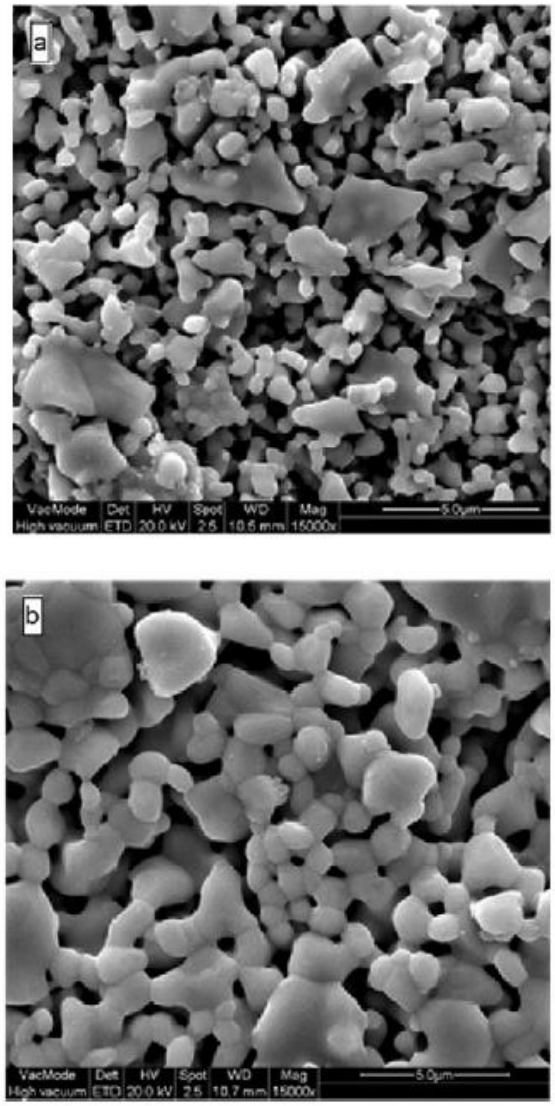

Fig. 3. 5 SEM top-views of LSM electrodes sintered at **(a)** 1050 °C and **(b)** 1150 °C.

Porosity was evaluated from analysis of SEM cross section images (Fig. 3. 6) with ImageJ software.

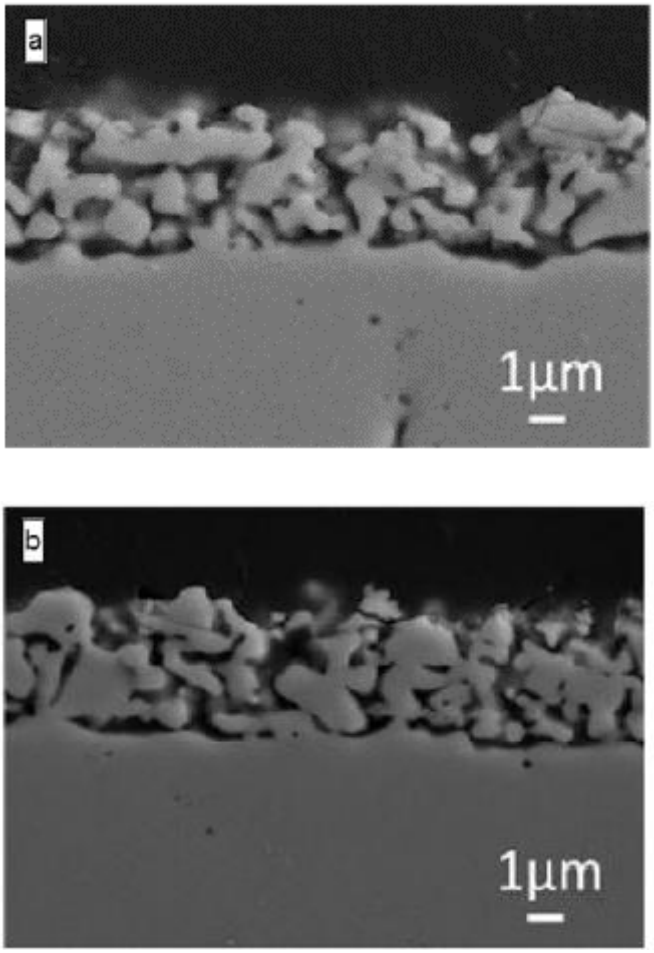

Fig. 3. 6 SEM cross-sections of LSM electrodes sintered at **(a)** 1050 °C **(b)** 1150 °C.

A detailed observation in backscattered mode did not highlight any evident formation of secondary phases at electrode/electrolyte interface in both the electrodes. For all the sintering temperature, porous electrodes showed a good necking among the particles and a well interconnected structure (Fig. 3. 5 and Fig. 3. 6). Fig. 3. 6 also revealed that both the electrodes had a regular and homogeneous thickness of 3 µm. This thickness value is sufficient to ensure even current distribution and good reproducibility with screen-printing as reported in literature (23-25). Indeed, all the relevant electrochemical phenomena are expected to take place within the electrode thickness. In particular is reported that the extension of reaction zone is typically no over 60 nm from

the 3-PB (three phase boundary) for the surface reaction path (26) and within of 1 μm from the YSZ interface as concern the oxygen reduction reaction controlled by bulk reaction mechanism (27). Both the mechanisms will be discussed in detail in next section.

Based on the small electrode thickness and the relatively high electrode porosity it is reasonable to assume that the gas transport of molecular oxygen does not play a significant role in the cathode polarization, as has been demonstrated even in thicker and more active electrodes (28). A further confirmation about this derived also from theoretical evaluation of polarization resistance related with this kind of phenomena. In fact, even considering an effective O_2 diffusivity (D_{eff}) of 0.16 $cm^2\ s^{-1}$ (this value is one order of magnitude lower than the binary O_2 diffusivity as a consequence of the microstructure influence on gas transport), the resistance associated to gas diffusion evaluate as:

$$R_{Gd} = \left(\frac{RT}{4F}\right)^2 \frac{L}{D_{eff} P_{O_2}} \qquad (3.1)$$

where L = 3 μm thick electrode at 700 °C and oxygen partial pressure of 0.21 atm is 4 * 10^{-5} Ω cm^2, which is 5 order of magnitude lower than the polarization resistance measured in the samples (e.g. Fig. 3. 2).

From Fig. 3. 7 it is well clear the high influence of structural differences on cathodic activity due to the remarkable change in the three – phase boundary length and gas/surface area available for the reaction. The figure (a,b and c) shows polarization resistance value obtained from electrochemical impedance measurements in a 3 – electrode configuration, as a function of applied cathodic overpotential (range 0 – 0.4 V) at two different temperature (700 – 800 °C). In the whole overpotential range the value of R_P is lower for the sample sintered at 1050 °C than the cathode sintered at 1150 °C. This is due to the contact of LSM particles with the electrolyte: the smaller the particle size, the higher the three-phase boundary, thus the smaller the polarization resistance. Globally, as the overpotential increases, R_P globally decreases for both the samples.

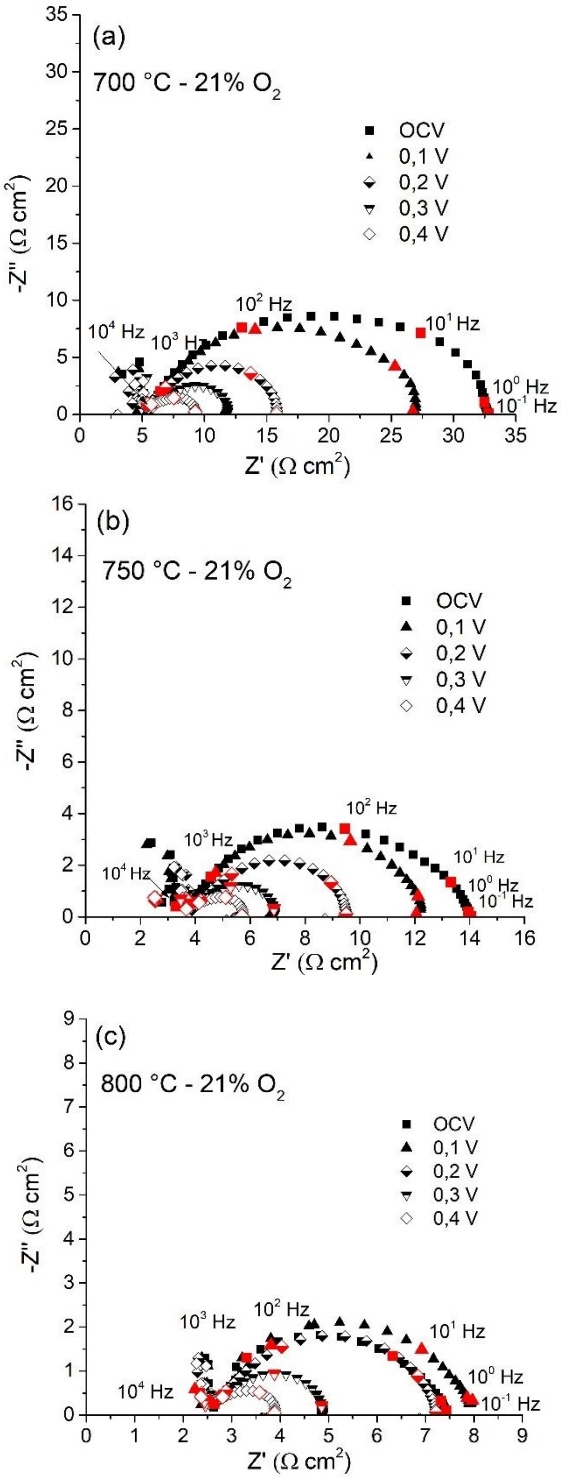

Fig. 3. 7 Impedance spectra at different cathodic overpotentials (OCV to 0.4 V) and temperatures for the sample type Cell – A sintered at 1050 °C. **(a)** 700 °C **(b)** 750 °C **(c)** 800 °C. Tests carried out in three – electrode configuration.

The explanation of this behavior is not trivial and requires considering the equilibrium between electrode surface and the gas phase. At OCV condition oxygen is adsorbed on the cathode surface (O_{ad}) and the same T and p_{O2}, the absolute amount of O_{ad} is higher for the sample sintered at 1050 °C, which presents a larger gas/solid surface area. Moreover, the sample sintered at 1050 °C has a more extensive three – phase boundary length at LSM/YSZ interface, which is expected to facilitate the charge-transfer reaction as reported in previous works (29-32). Then, the impact of microstructure at OCV is that the sample with a lower 3-PB extension (sintered at 1150 °C) shows a larger polarization resistance than the other (sintered at 1050 °C) in the whole temperature range. This conclusion suggests that at OCV the oxygen reduction reaction is dominated by the processes occurring on LSM surface and at the 3–PB, in accordance with previous experimental findings (10, 33) and also theoretical analyses presented in literature (30, 34).

It is reported that, applying a cathodic overpotential, oxygen vacancies in LSM are formed due to the reduction of Mn^{4+} to Mn^{3+} (35, 36). In fact, a high cathodic polarization produces analog effects of a decrease in oxygen partial pressure (19, 37), as well highlighted by the following Nernst equation:

$$\eta = \frac{R\,T}{4F} \ln\left(\frac{p_{O_{2,gas}}}{p_{O_{2,ref}}}\right) \qquad (3.2)$$

The reduction of manganese cations leads to the activation of a new reaction path involving the LSM bulk, with a shift from three phase boundary (3-PB) and surface-dominated regime to a two phase boundary (2-PB) and bulk-dominated regime (27, 30, 33, 36). This regime transition is highlighted in Fig. 3. 8 for overpotential over 0.2 V. At each temperature (700 – 750 – 800 °C) an asymptotic R_P value is observed at 0.4 V, very close for both the samples. This behavior points out, that over a overpotential threshold the bulk path is activated in LSM electrode, and then the determining factor of the overall ORR is no more the 3-PB length, but the extension of contact area between the two phases (2-PB, at LSM/YSZ interface) as sketched in Fig. 3. 9.

It is also interesting to evaluate and discuss the increase of R_P at low overpotential ($0 \leq \eta \leq 0.1$ V) before dropping for $\eta \geq 0.2$ V as described above. This behavior is consistent with the transition from surface – dominated path to bulk –

dominated path. Close to OCV condition ($\eta \leq 0.1$ V) the bulk path is not yet activated (30, 31, 33, 38), then the ORR process is controlled by oxygen adsorbed on LSM and charge-transfer reaction occurring at the 3-PB (33). Working at higher overpotential, the surface concentration of oxygen adsorbed on LSM is expected to decrease close to YSZ interface as predicted by different mechanistic models (29-31, 39). The consume of oxygen adsorbed causes an increase in polarization resistance until the bulk path is activated by the formation of oxygen vacancies in LSM bulk (30, 31, 33, 39).

The opening of this new transport mechanism provides a parallel reaction pathway reducing the polarization resistance for $\eta \geq 0.2$ V. For the electrode sintered at 1150 °C the higher is the working temperature, the higher is the starting increase in polarization resistance for $\eta \cong 0.1$ V; this is reasonable because the equilibrium oxygen surface concentration is expected to decrease as the temperature goes up (32). Moreover the initial increase of R_P in the overpotential range of 0 – 0.1 V, has been theoretically predicted by Gong et al. (30) as a consequence of current density, produced by the surface and 3-PB-dominated mechanism, when the bulk path has not yet been activated by higher cathodic overpotentials. Sample sintered at 1050 °C shows an increase in R_P at low overpotential ($\eta \cong 0.1$ V) only at high operating temperature (800 °C). Its larger surface area and 3-PB length compensate the depletion of adsorbed oxygen and thus maintain current close to OCV value thanks to the 3-PB-dominated path even before the activation of parallel bulk path. Therefore, these impedance results are consistent with the transition of oxygen reduction reaction regime from surface to bulk path and in agreement with previous literature.

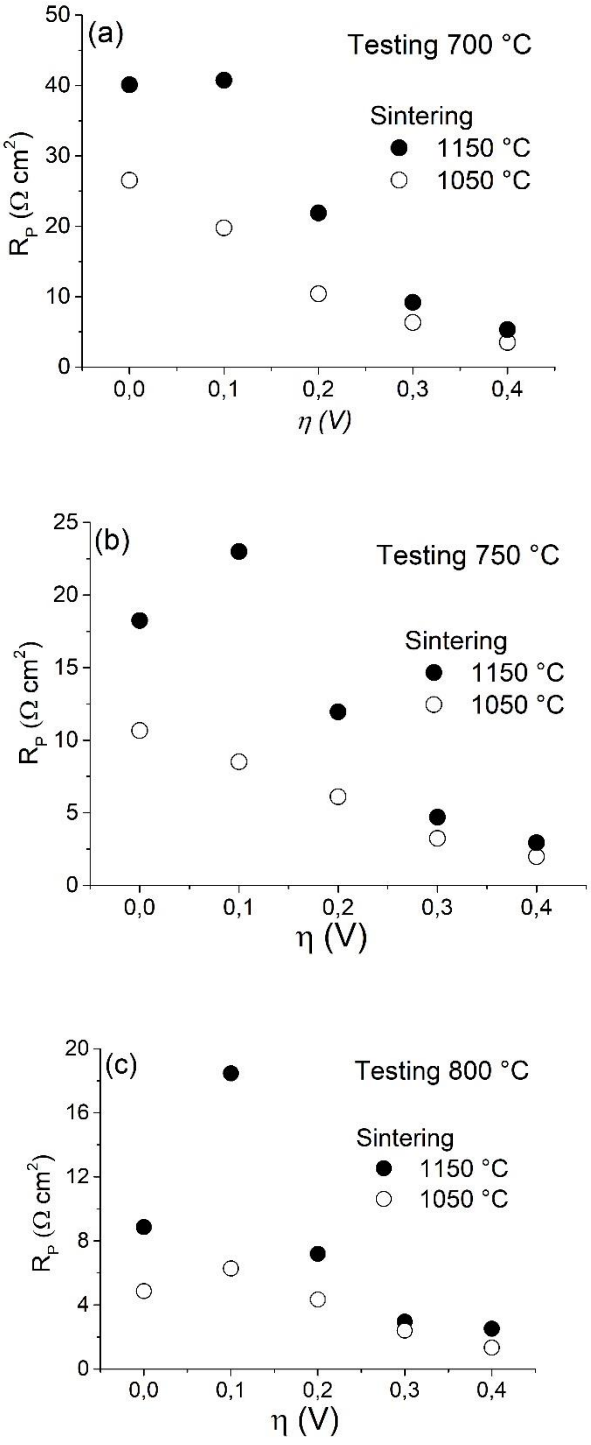

Fig. 3. 8 Trends of polarization resistance (RP) at different temperatures **(a)** 700 °C **(b)** 750 °C and **(c)** 800 °C for samples sintered at 1050 °C and 1150 °C

In order to support the interpretation given above about the global drop in polarization resistance as a function of overpotential some geometric considerations are performed under the following assumptions:

i. LSM particles at the electrode/electrolyte interface are spherical and partially sunk in the electrolyte in order to simulate the necking of the two phases;

ii. the total number of particles at the electrode/electrolyte interface is estimated coherently with the electrode porosities and average LSM particle sizes.

Based on these assumptions a *geometric index GI* is introduced taking into account the total active area that includes two possible contributions:

i. the LSM particle perimeter $\widetilde{C_\iota}$ in contact with the electrolyte, that in principle is a one dimensional line (3-PB)

ii. the surface extension if the active area enlarges on LSM/YSZ contact area $\widetilde{A_\iota}$at the electrode/electrolyte interface (Fig. 3. 9)

Therefore the geometric index is defined as:

$$GI = \widetilde{C_\iota} + \widetilde{A_\iota} \tag{3.3}$$

Both *GI*, $\widetilde{C_\iota}$ and $\widetilde{A_\iota}$ are dimensionless quantities, and the discussion addresses the problem from a geometric side, and a derivation is reported below. For the samples sintered at 1150 °C and 1050 °C, spherical particles with radius R and r, respectively, are considered. The circumference at electrode – electrolyte interface is evaluated taking into account an apparent radius equal to:

$$\hat{R}_i = R \cdot x \tag{3.4}$$

$$\hat{r}_i = r \cdot y \tag{3.5}$$

with $0 < x, y < 1$ and then the contact area $A_i^{interface}$ $(i = 1, 2)$ is:

$$A_i^{interface} = \pi * \hat{R}_i^2 \tag{3.6}$$

The total number of particles n_i at electrode – electrolyte interface is equal to:

$$n_i = (1 - \phi_i) \frac{A_{geo}}{\pi \widehat{R_i^2}} \tag{3.7}$$

where A_{geo} is the geometric area of the cathode ($7.1 * 10^{-6}$ m^2) and ϕ_i is the porosity.

At open circuit voltage (OCV) conditions, which is related to the surface path, only the three phase boundary (3-PB) at electrode – electrolyte interface is considered as active region, so a linear contribution C_i^{active} is identified:

$$C_i^{active} = 2\pi \hat{R}_i n_i \tag{3.8}$$

The ratio $\tilde{C}_i$ between the active circumference and its maximum value C_i^{max}(for x, y = 1) is defined as follows:

$$\widetilde{C}_\iota = \frac{C_i^{active}}{C_i^{max}} \tag{3.9}$$

The application of overpotential leads to an extension of reaction area, defined as a penetration depth δ within electrode-electrolyte contact area. This active area variation is defined as:

$$A_i^{active} = n_i \cdot \pi \left(\hat{R}_i^2 - \left(\hat{R}_i - \delta \right)^2 \right) \tag{3.10}$$

It was assumed that δ depended only on the applied overpotential, and the maximum penetration corresponds to $\delta_i^{max} = \hat{R}_i$. For $\delta = \delta_i^{max}$ the active surface is equal to the total contact area between LSM – electrolyte interface ($A_i^{interface}$, i = 1,2). Defined these quantities the ratio between the two value, $\tilde{A}_i$, is introduced as follows:

$$\widetilde{A}_\iota = \frac{A_i^{active}}{A_i^{max}} \tag{3.11}$$

Then two different contributions are taken into account: the first one related to the 3-PB length (C_i^{active}), the latter linked with the activation for oxygen reduction reaction of particle surface (A_i^{active}), and their sum determined the *geometric index* presented above. Based on all previous points, it is expected that the surface path and bulk path scale with $\widetilde{C}_\iota$ and $\widetilde{A}_\iota$, respectively.Table 3. 1, reported parameters used to calculate the geometric index for sample sintered at 1150 °C (Sample A) and 1050 °C (Sample B).

Parameters		**Description**
Sample #1 (1150 °C)	**Sample #2** (1050 °C)	
R = 1 µm	r = 0.35 µm	Average particle radius
$0 < x < 1$	$0 < y < 1$	Tuning parameter
$R \cdot x$	$r \cdot y$	Radius of circumference electrode/electrolyte interface
$\Phi_1 = 0.34$	$\Phi_2 = 0.49$	Electrode porosity
C_1	C_2	Circumference at interface
N	n	Number of particles
δ	δ	Penetration depth

Table 3. 1 Parameters used to calculated geometric index for sample sintered at 1150 °C (Sample A) and 1050 °C (Sample B)

The values assumed by *GI* are compared for the two electrodes sintered at 1050 °C and 1150 °C as a function of δ, which represents the penetration depth associated to the extension of ORR at the electrode/electrolyte interface as a consequence of a transition from a 3-PB to a 2-PB-based reaction mechanism (Fig. 3. 9).

Fig. 3. 9 shows that in absence of penetration of the oxygen reduction reaction (ORR) to the LSM/YSZ contact area (δ=0), the *GI* value for the sample sintered at 1050 °C is twice larger than the *GI* calculated in the sample sintered at 1150 °C. Based on our assumptions, for δ = 0 only the linear 3-PB contribution is considered for the charge-transfer. Notably, the ratio between the experimental polarization resistances at OCV of samples sintered at 1050 °C and 1150 °C, and this suggests that at OCV the ORR scales with the 3-PB length.

Fig. 3. 9 also well highlights a progressive decrease in the difference of *GIs* as a function of δ. This behavior is coherent with the results reported above in Fig. 3. 8, where the difference between measured polarization resistance decreases as the

overpotential assume higher values. In fact, for $\delta > 0$ *GI* considers the enlargement of the 3-PB to the LSM/YSZ contact area, involving a bulk ion transport, recalling the behavior of a mixed ionic conductor (MIEC). The agreement between *GIs* trend and experimental polarization resistance highlights that under high cathodic overpotential a new possible bulk path for oxygen ions is activated in the LSM electrodes. This transition of the kinetic regime is further investigated by considering the whole impedance spectra of the cathode, as reported in the next paragraph.

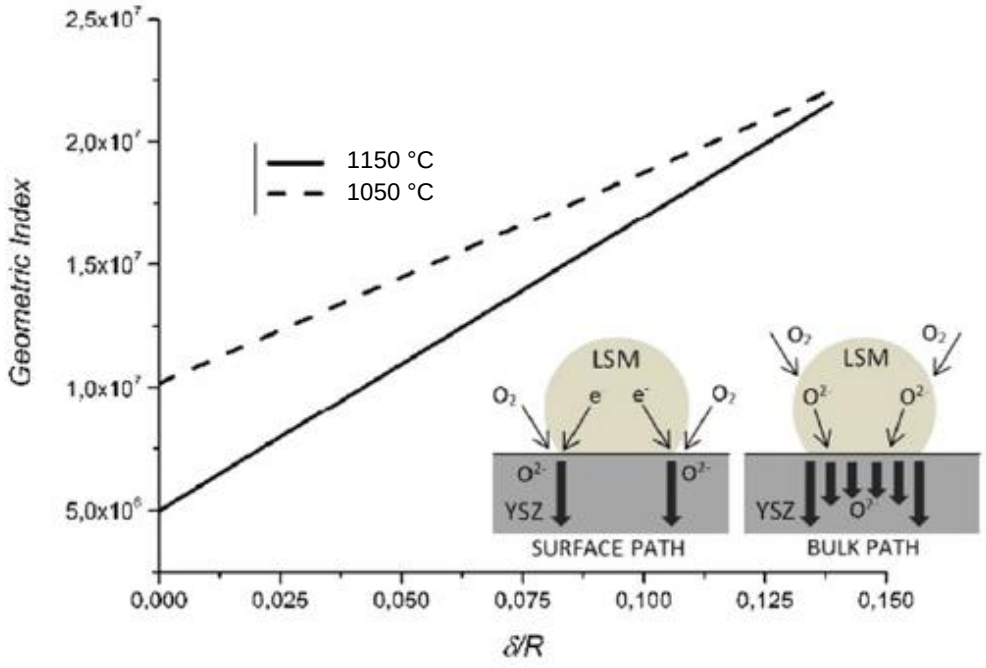

Fig. 3. 9 Variation of the calculated total active area for ORR, namely geometric index GI, with the increase in the 3-PB extension within LSM electrode of a distance δ (δ = penetration depth, R = average particles diameter,)

3.3.3 Effect of overpotential

As reported above overpotential plays a key role in the transition from a surface path (3-PB) to (2-PB) and in this section a deeper analysis about its effects is reported. Fig. 3. 7, that reports the effect of cathodic bias (up to -0.4 V) at different temperature (700, 750, 800 °C), clearly show a depressed capacitive feature, strongly depending by overpotential increases.

Analysis of impedance results starts from the evaluation of distribution relaxation time (DRT), with the aim to identify the main processes involved and their characteristic frequency. Reports DRT analysis for the sample sintered at 1050 °C during the electrochemical test at 700 °C and oxygen partial pressure of 0.21 atm at different overpotential. DRT curves have two well defined peaks pointing out two different phenomena. Other preliminary information are obtained focusing on the behavior of low-frequency (LF) peak and high frequency (HF) peak. Firstly, the area under the LF peak is greater than those under HF part, and their ratio change as a function of applied overpotential. Moreover, the area itself and the characteristic frequency of LF peak are highly affected by bias, while the other peak remains stable after a starting shift from OCV to -0.2 V conditions.

Starting from DRT results an equivalent circuit described by $R_{el}(R_{LF}Q_{LF})(R_{HF}C_{HF})$ is chosen, where R_{el} describes electrolyte resistance, R_{LF} and R_{HF} the resistance at low and high frequency, respectively; Q_{LF} is the constant phase element, while at high frequency a pure capacitive behavior it is represented by C_{HF}. The low error fitting (< 10 % for all the parameters) and the information extrapolated from equivalent circuit analysis in agreement with those obtained by DRT, support the reliability and then the use of the proposed EC in the whole conditions range investigated.

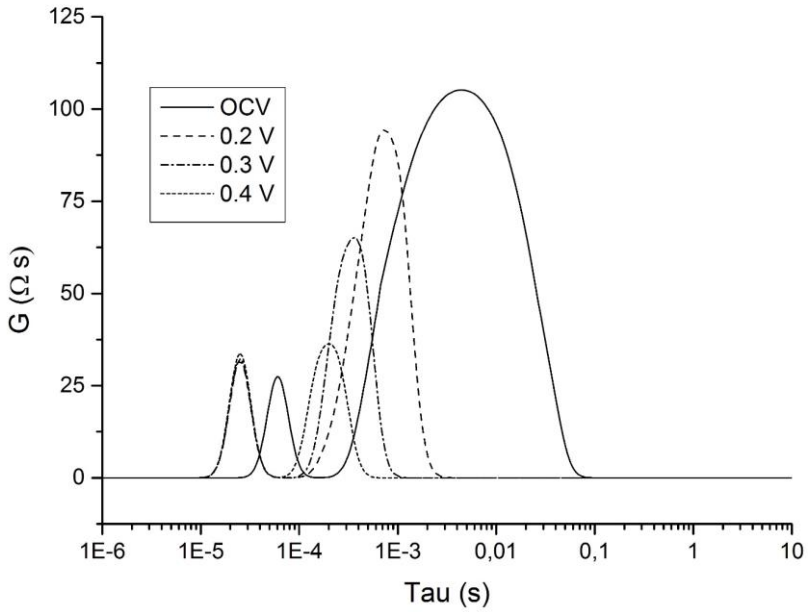

Fig. 3. 10 Distribution of relaxation times (DRT) for the sample sintered at 1050 °C, tested at 700 °C, 0.21 atm O_2, at different overpotentials.

Going more in detail LF subcircuits can be related with surface transport phenomena, while the HF subcircuit required to be carefully considered, but in principle, it is reasonable related to charge - transfer process. As shown in Fig. 3. 11 R_{LF} has a remarkable drop as a function of temperature, and this behavior can be explained by an increased mobility of adsorbed specie. In fact, at OCV and at low bias (< 0.15 V), the decrease in R_{LF} when the temperature grows up is justified by an enhancement of oxygen diffusion coefficient. Over this threshold value of 0.15 V, process kinetic is improved, and then followed by a significant increase of ln ($1/R_{LF}$); moreover is noteworthy that the lower the temperature the higher the positive effect of overpotential on the low frequency resistance. The increase in ln($1/R_{LF}$) as a function of applied bias points out a transition in the ORR towards a bulk reaction path, in agreement with the previous results from the geometric index (GI) and confirmed by other results reported in literature (30, 38, 40).

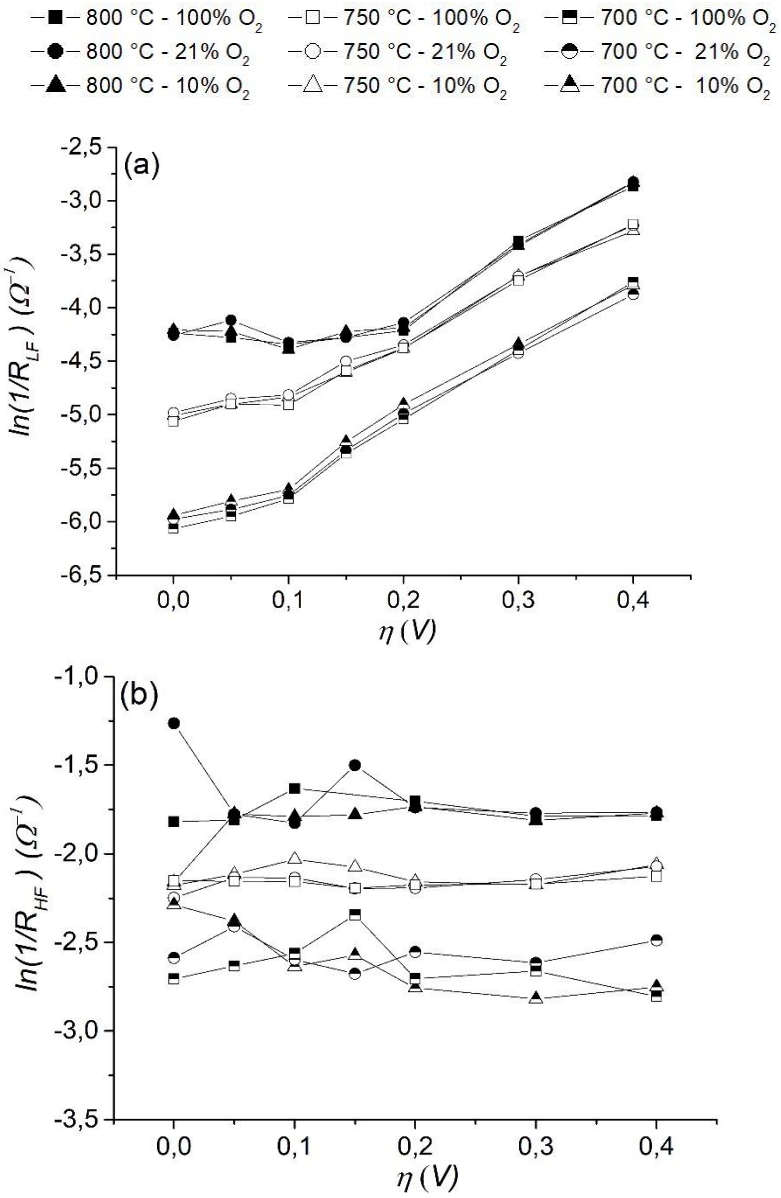

Fig. 3. 11 (a) ln(1/R_{LF}), **(b)** ln(1/R_{HF}) for the sample sintered at 1050 °C

As regards low frequency capacitance from R_{LF}//CPE element, it shows a slow lowering trend as reported in Table 3. 2. Moving to the high frequency range, from impedance spectra the high frequency capacitance (C_{HF}) has an initial increase, reaching a maximum close to 0.15 – 0.20 V, and then decreases. This peculiar behavior can be explained by an accumulation of charges in the active polarized sites at low overpotential. At higher bias (from 0.2 V) charge is progressively drawn by the enhancement of transport phenomena driven by the increase in the potential gradient.

The related resistance R_{HF} does not show a clear trend, especially for low polarization value (< 0.15 V), while over 0.2 V the almost constant value of R_{HF} is obtained in accordance with high frequency peak of DRT analysis that varies only with the temperature.

η [V]	R_Ω [Ω cm^2]	R_{HF} [Ω cm^2]	C_{HF} [F cm^{-2}]	R_{LF} [Ω cm^2]	Q [F s^{n-1}]	n	C_{LF} [F cm^{-2}]
800 °C – 21% O_2							
0	2.4	0.25	$1.69*10^{-5}$	5.01	$3.2*10^{-5}$	0.79	$9.15*10^{-5}$
0.05	2.4	0.42	$8.03*10^{-6}$	4.36	$2.6*10^{-5}$	0.82	$9.44*10^{-6}$
0.1	2.3	0.44	$6.20*10^{-6}$	5.37	$2.6*10^{-5}$	0.80	$8.03*10^{-6}$
0.15	2.6	0.31	$2.25*10^{-5}$	5.12	$1.8*10^{-5}$	0.83	$6.62*10^{-5}$
0.2	2.5	0.40	$1.39*10^{-5}$	4.46	$1.3*10^{-5}$	0.86	$5.92*10^{-5}$
0.3	2.5	0.41	$1.25*10^{-5}$	2.15	$1.0*10^{-5}$	0.89	$5.92*10^{-5}$
0.4	2.4	0.41	$1.14*10^{-5}$	1.19	$1.0*10^{-5}$	0.92	$6.34*10^{-5}$
750 °C – 21% O_2							
0	3.13	0.62	$4.37*10^{-6}$	10.61	$3.9*10^{-5}$	0.76	$1.11*10^{-4}$
0.05	3.24	0.58	$6.20*10^{-6}$	9.55	$3.4*10^{-5}$	0.78	$1.01*10^{-4}$
0.1	3.32	0.54	$8.73*10^{-6}$	8.95	$2.6*10^{-5}$	0.79	$8.73*10^{-5}$
0.15	3.46	0.56	$1.83*10^{-5}$	7.09	$1.6*10^{-5}$	0.85	$7.46*10^{-5}$
0.2	3.71	0.61	$1.14*10^{-5}$	5.67	$1.4*10^{-5}$	0.85	$6.48*10^{-5}$
0.3	3.70	0.62	$1.27*10^{-5}$	2.88	$1.0*10^{-5}$	0.89	$6.20*10^{-5}$
0.4	3.54	0.55	$8.03*10^{-5}$	1.89	$1.7*10^{-5}$	0.83	$5.21*10^{-5}$
700 °C -21% O_2							
0	4.85	0.70	$9.44*10^{-6}$	26.99	$4.1*10^{-5}$	0.73	$1.32*10^{-4}$
0.05	4.88	0.76	$1.15*10^{-6}$	23.63	$3.2*10^{-5}$	0.76	$1.14*10^{-4}$
0.1	4.60	0.99	$4.93*10^{-6}$	21.24	$2.8*10^{-5}$	0.77	$9.44*10^{-5}$
0.15	4.96	0.93	$1.55*10^{-5}$	13.59	$1.6*10^{-5}$	0.84	$7.32*10^{-5}$
0.2	4.98	1.11	$1.97*10^{-5}$	9.59	$9.4*10^{-6}$	0.90	$6.34*10^{-5}$
0.3	5.36	1.19	$1.55*10^{-5}$	5.45	$7.3*10^{-6}$	0.90	$5.63*10^{-5}$
0.4	5.15	1.11	$9.86*10^{-6}$	3.14	$7.2*10^{-6}$	0.91	$4.79*10^{-5}$

Table 3. 2 Summary of fitting parameters at 700, 750, 800 °C and 0.21 atm of oxygen partial pressure for the chosen equivalent circuit for sample sintered at 1050 °C

3.3.4 A Further confirmation: physically-based model of ORR in LSM electrode

To confirm all the assumptions made above regarding changes in kinetic mechanism of oxygen reduction reaction in LSM electrode a physically-based model was developed. This part of the project was in collaboration with the Department of Civil and Industrial Engineering of University of Pisa, which was the main actor in model development (41) with Professor Antonio Bertei.

In this model only a surface path was taken into account, considering adsorption/diffusion of oxygen and the charge-transfer reaction as co-limiting processes. Fig. 3. 12 sketches phenomena considered by the model.

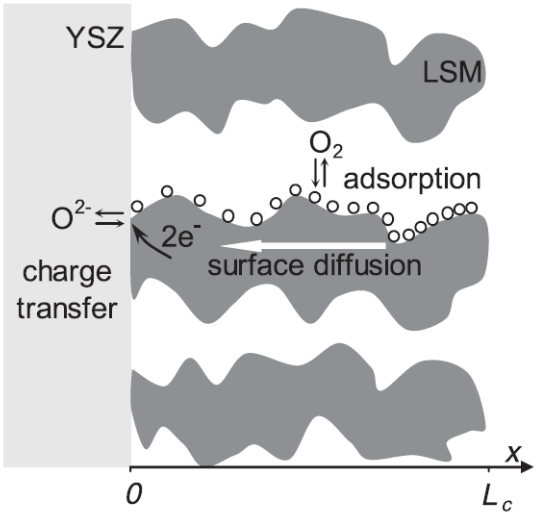

Fig. 3. 12 Sketch of surface path considered by the model (41)

The global process can be split in two steps:

- molecular oxygen is adsorbed onto LSM electrode surface following a dissociative adsorption mechanism:

$$O_{2(g)} \leftrightarrow 2O_{(el,s)} \tag{3.12}$$

Adsorbed oxygen diffuse on the surface of the cathode reaching the Three Phase Boundary (TPB) at electrode/electrolyte interface;

- at TPB a charge-transfer reaction occurs with formation of oxygen ions:

$$O_{(el,s)} + 2e^-_{(el)} \leftrightarrow O^{2-}_{(io)} \quad (3.13)$$

Then oxygen ions are incorporated into the electrolyte.

Moreover, the main model assumptions are:

- adsorption/desorption reaction follows a dissociative Langmuir kinetic (31);
- surface diffusion of oxygen adatoms is described by Fick law (42);
- charge – transfer reaction takes place only at TPB, following a Butler – Volmer kinetic;
- electron transport and gas transport along thickness are neglected, because they are considered to be faster than other processes involved;
- temperature is consider uniform in the model;
- microstructure is treated as a continuum of LSM and porous phase. Material properties are assumed to be uniform, then the model is 1D along the cathode thickness.

In the Appendix of Chapter 3 are reported the model equations used to simulate EIS curve of a porous LSM electrode.

Model Results

Model was calibrated at OCV conditions by comparing model simulation with experimental data at different temperature and oxygen partial pressure. Fig. 3. 13 (a) presents model calibration at OCV, 21% O_2, and different temperatures, while Fig. 3. 13 (b) reports calibration at different partial pressure (750 °C – OCV). Model fits quite well the shape in the whole range conditions. Model deviations from experimental data can be attributed to two main reasons:

i) model is a simplified description of reality

ii) a global calibration approach was used, with a single set of parameters for all the spectra analyzed, without searching for the best fit of each single spectra analyzed.

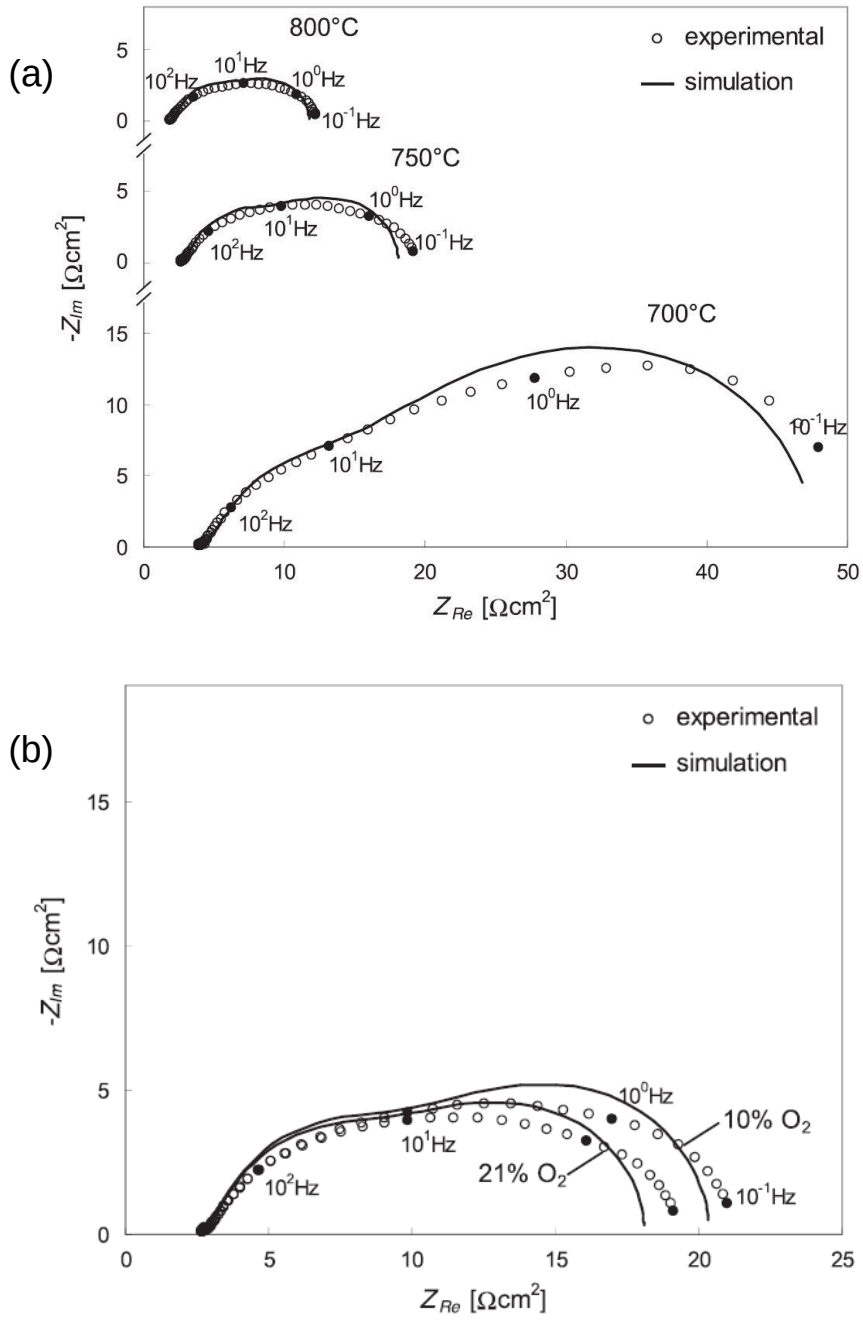

Fig. 3. 13 Model calibration with experimental data at **(a)** different temperatures (OCV and 21% p_{O2}) **(b)** different oxygen partial pressure (OCV and 750 °C) (41)

Calibrated model was used to evaluate the transition of kinetic regime due to the application of dc bias to the cathode material, as hypothesized above from experimental

data. Fig. 3. 14 (a) and (b) report impedance for different bias at 700 °C and 750 °C, respectively.

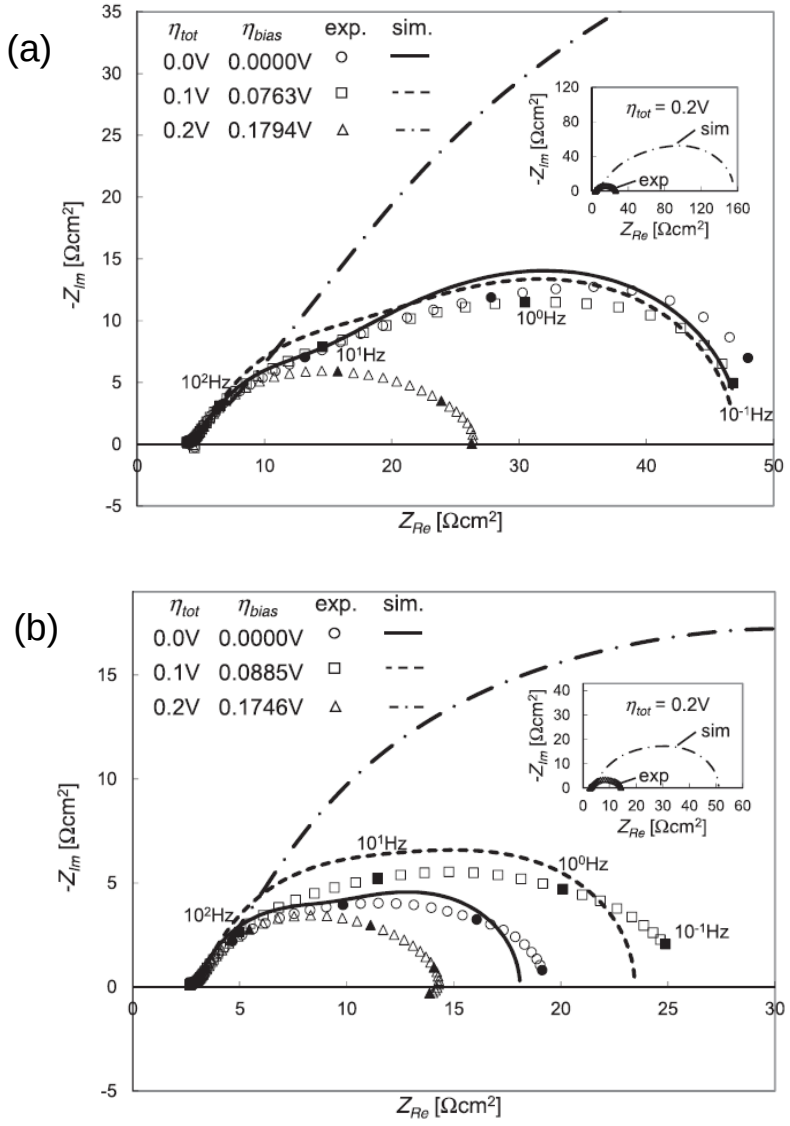

Fig. 3. 14 Impedance for different bias, 21% O_2 at **(a)** 700 °C and **(b)** 750 °C to evaluate kinetic transition (41)

Discussion starts considering overpotential range 0 – 0.1 V. At 700 °C (Fig. 3. 14 (a)), moving from OCV to 0.1 V experimental EIS show a slight variation of polarization resistance and the model is able to follow this behavior. The same overpotential variation causes a strong R_P variation at 750 °C, and also in this case the

model response is in accordance with experimental one. This agreement between experimental data and model curves is achieved without adjusting any parameters, pointing out a reliability of the model itself.

Fig. 3. 14 also highlights that for a bias equal to 0.2 V model strongly deviates from experimental impedance curves. In fact the simulated curve continue to increase as a function of applied overpotential, while experimental data show a decrease in polarization resistance. This divergence can be attributed to the transition from a surface path to a bulk path, completely neglected in the model. The value of 0.2 V as a threshold overpotential for the regime transition is in accordance with other works reported in literature (17, 29, 33, 36).

3.4 An application: LSM – infiltrated cathodes

In this last part of Chapter 3 is presented a possible application of LSM based on the results presented above. This section is the result of the efforts of our group (especially Dr. Alice Giuliano) and the product of a collaboration with Polytechnic Department of Engineering and Architecture of University of Udine and Institute for Studies on Nanostructured Materials at Italian National Research Council (43). Here LSM material is no longer used as backbone material but as impregnating agent on $La_{0.6}Sr_{0.4}Co_{0.2}Fe_{0.8}O_3$ (LSCF) and $Ba_{0.5}Sr_{0.5}Co_{0.8}Fe_{0.2}O_3$ (BSCF) electrodes. In fact, these two materials provide excellent performance at intermediate temperature, but they are missing in stability.

3.4.1 Experimental

$La_{0.6}Sr_{0.4}Co_{0.2}Fe_{0.8}O_3$ (LSCF) and $Ba_{0.5}Sr_{0.5}Co_{0.8}Fe_{0.2}O_3$ (BSCF) backbone electrodes were deposited on SDC electrolyte (SDC20 – HP, Fuel Cell Materials). The electrolyte powders was cold pressed at 60 MPa, and then sintered at 1500 °C for 5 hours. LSCF and BSCF powders were synthesized by a solution combustion synthesis process, with the collaboration of other research group (44), and deposited on SDC electrolyte using a slurry coating technique. Then, a sintering cycle was carried out with an initial heating at 200 °C to evaporate the organics, followed by a sintering step at 1100 °C for 2 hours

Both materials were tested in a symmetric configuration, and the electrodes have a geometric area of 0.28 Ω cm^2.

Working electrode (WE) and counter electrode (CE) were infiltrated by a solution of LSM 2 M prepared by using a Glycine – Nitrate sol-gel combustion synthesis. A proper amount of LSM precursors ($La(NO_3)_3 \cdot 6H_2O$ (99%), $Sr(NO_3)_2$ (>99%) and $Mn(NO_3)_2 \cdot 4H_2O$ (98%) (Sigma Aldrich)) was dissolved in distilled water at room temperature. To control phase formation and morphology, a chelating agent (glycine, with a volume ratio of glycine to LSM ~ 2.5:1) and a surfactant (Polyvinyl pyrrolidone PVP, Sigma Aldrich) were added to metal nitrates solutions. Hence, solution

was heated to 200 °C and stirred until the gel was obtained, followed by a combustion reaction to obtain LSM powder.

Prepared LSM powder was dissolved in water and infiltrated (3 μm) into the porous electrodes. To promote air elimination form LSCF and BSCF, cell was placed under vacuum for 1 hour. After that, the cell was heated to 700 °C for 1 hour, to obtain the desired crystalline phase of LSM.

3.4.2 Results and discussions

Microstructural results

LSM powder, calcinated at 700 °C, was analyzed by XRD and compared with a commercial LSM pattern (Fig. 3. 15). Perovskite phase is formed and any secondary phases were detected. XRD analysis of LSM-infiltrated LSCF and BSCF samples confirmed the presence of desired phase as reported in Fig. 3. 16; also in this case no secondary phases were found.

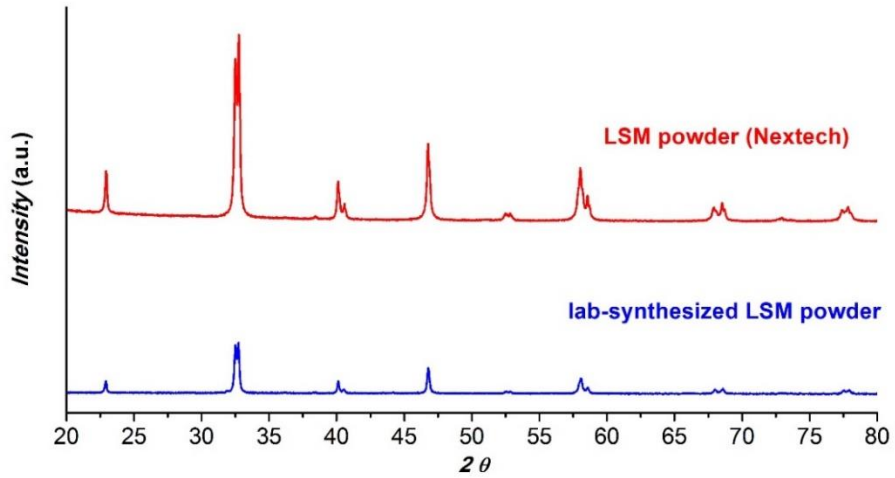

Fig. 3. 15 XRD pattern of LSM powder calcinated at 700 °C, compared with a commercial LSM powder (Nextech).

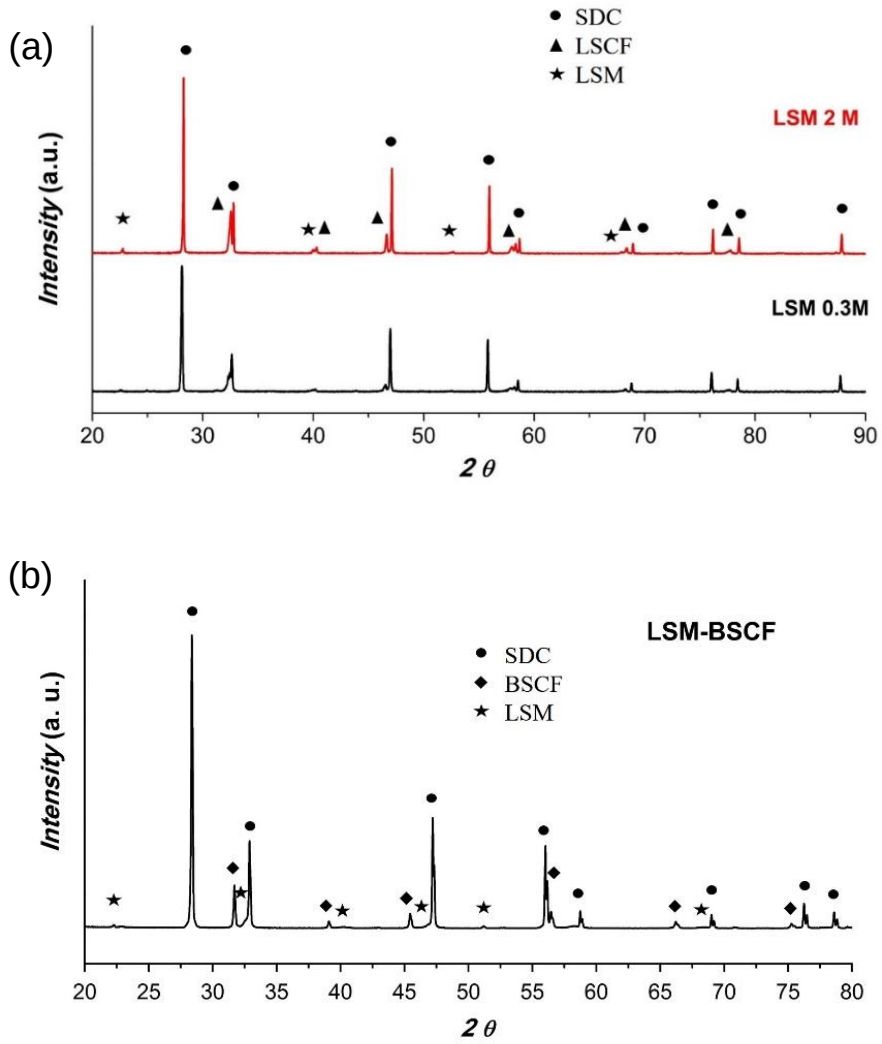

Fig. 3. 16 XRD patterns of **(a)** LSM – infiltrated LSCF and **(b)** LSM – infiltrated BSCF electrodes deposited on SDC electrolyte

The presence of LSM on electrode backbones was also confirmed by Scanning Electronic Microscopy (SEM) analysis reported in Fig. 3. 17. The infiltrated LSM phase has nanoparticles in the order of 100 nm in both samples.

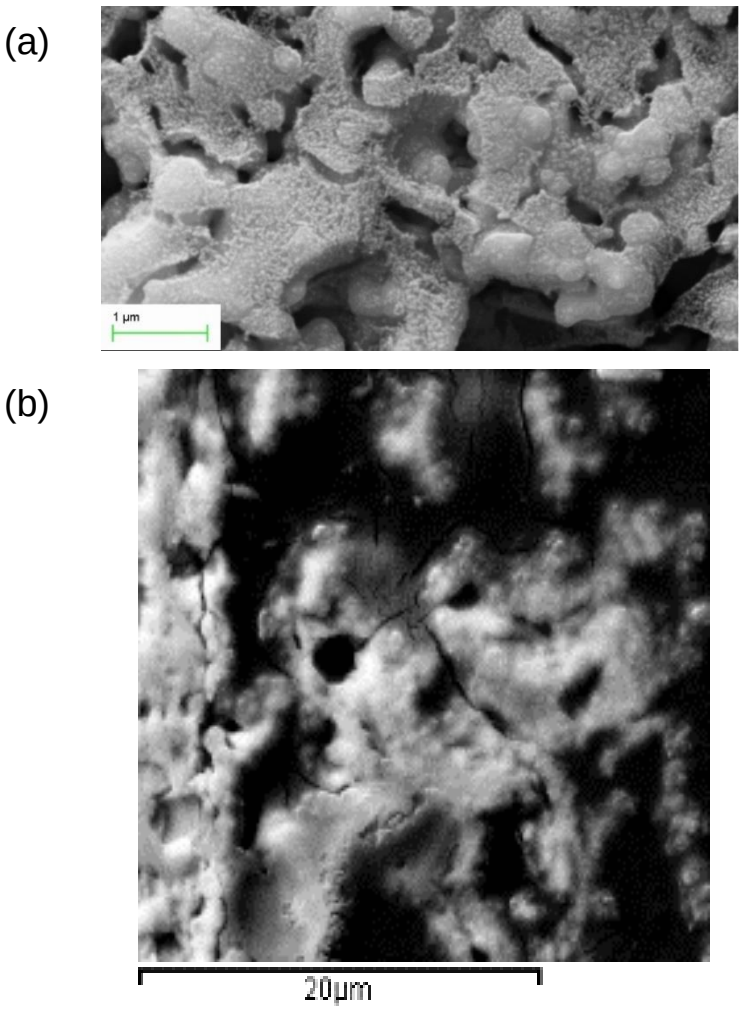

Fig. 3. 17 Top-view SEM images for **(a)** LSCF and **(b)** BSCF LSM – infiltrated

Electrochemical results

Infiltrated electrode were electrochemically tested by means of electrochemical impedance spectroscopy; performance and stability were compare with LSCF and BSCF reference electrodes.

To extrapolate apparent activation energy, LSCF electrodes were investigated in a temperature range of 500 – 800 °C, and BSCF – based electrode in a range of 400 – 700 °C, at OCV and air.

Fig. 3. 18 firstly highlights that BSCF has a polarization resistance one order of magnitude lower than LSCF electrode. Furthermore, the presence of LSM infiltrated

particles produce a benefit effect on performance of both cathodes. In fact, despite LSCF and BSCF are MIEC the presence of thin LSM film on their surface introduces extra specific surface area available for oxygen reduction reaction.

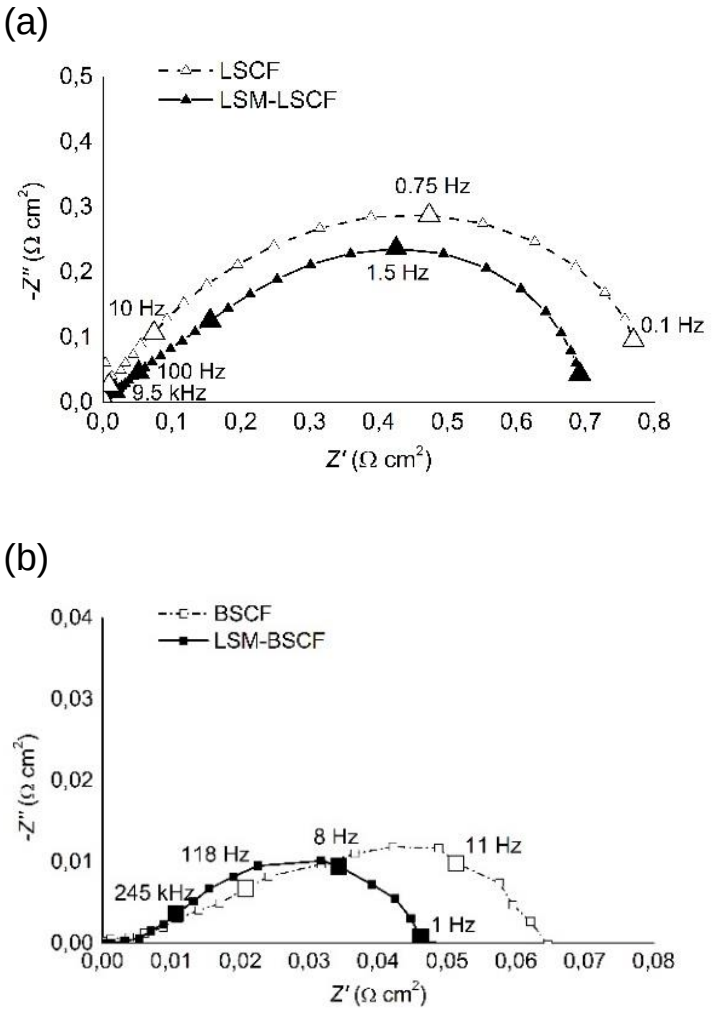

Fig. 3. 18 Nyquist plot of **(a)** LSCF and LSM-LSCF cathodes and **(b)** BSCF and LSM-BSCF cathodes, at 700 °C, in air and open circuit voltage (OCV).

Determination of R_P in the whole temperature range provides data to build Arrhenius plot and calculate activation energy for four electrodes (Fig. 3. 19). The E_{act} for BSCF electrode is unaffected by LSM infiltration (value of 0.99 eV for both electrodes), while LSCF and LSM-LSCF electrodes have an activation energy of 1.45

eV and 1.41 eV, respectively. For all the electrodes data are in agreement with literature values (19, 45).

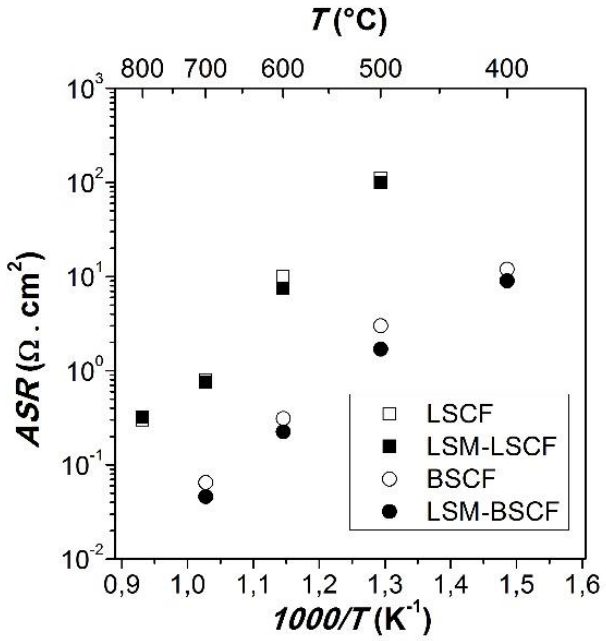

Fig. 3. 19 Arrhenius plot for LSCF and BSCF based electrodes

Impedance data were analyzed by using two different equivalent circuits, proposed in Fig. 3. 20

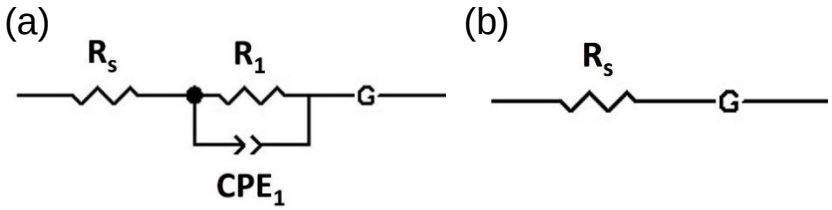

Fig. 3. 20 Equivalent circuits used for the impedance measurements fitting.

The choice of equivalent circuit is based on Adler – Lane – Steele model (ALS) (46, 47) able to describe kinetic for porous mixed conducting oxygen electrodes. Circuit (a) has been used to fit BSCF, LSM – BSCF and reference LSCF electrodes; it is made by a resistance R_s which represents the electrolyte ohmic losses, in series with a RQ circuit and a Gerischer element. Subcircuit RQ describes the high frequency of

impedance arc, associated to the oxygen ion transfer at electrode-electrolyte interface. Gerischer elements was attributed both to the chemical reaction at electrode surface and to the diffusion process inside bulk. From fitting parameters such as chemical resistance (R_{chem}), chemical capacitance (C_{chem}) were extrapolated.

C_{chem} has been attributed to charge stored by the oxygen vacancies in electrode volume (48-50), then for ALS model C_{chem} is directly proportional to the concentration of vacancies.

Equivalent circuit reported in Fig. 3. 20 (b) was used to fit LSM – LSCF data. In this case the lacking of RQ circuit means that process is highly dominated by surface phenomena and solid-state diffusion, and the oxygen ion transfer at electrode/electrolyte interface is negligible.

Further information about infiltrated systems were provided by impedance tests applying a cathodic overpotential. Fig. 3. 21 (a) – (c) show the effect of a bias on LSCF-based electrode at 700 °C. Cathodic polarization has a positive effect on R_P for both electrodes, with a stronger R_p reduction for the infiltrated one. BSCF electrodes (Fig. 3. 21 (b) – (d)) have an opposite behavior than LSCF cathodes, with a progressive increase of polarization resistance as a function of overpotential.

A possible explanation of electrode behaviors is the effect of applied DC bias on the two references materials. In fact is reported that LSCF forms new oxygen vacancies promoting ion transport (19, 51-53). On the contrary, for BSCF a possible formation of cluster of oxygen vacancies is proposed in literature (54, 55).

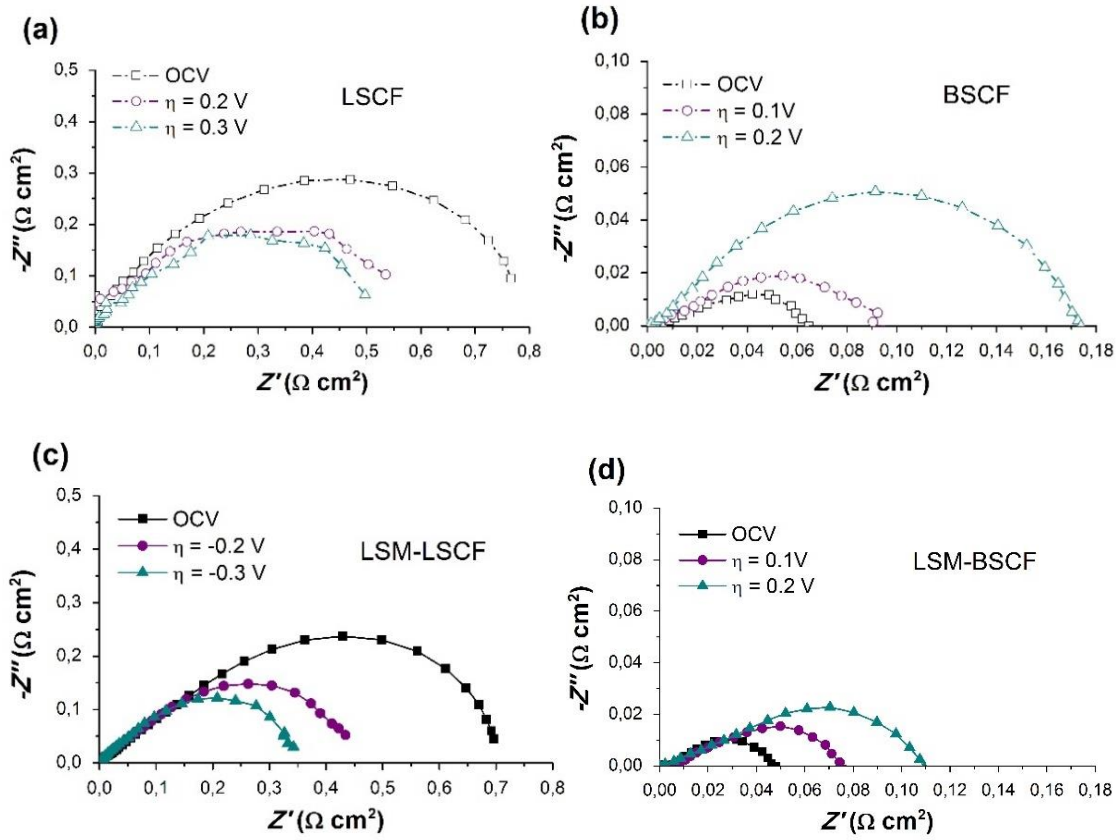

Fig. 3. 21 Nyquist plot for impedance measurements under cathodic overpotential for **(a)** LSCF **(b)** BSCF **(c)** LMS-infiltrated LSCF and **(d)** LSM-infiltrated BSCF electrodes at 700 °C in air.

To make the discussion more completed further information can be obtained by parameters of equivalent circuit. From ALS model quantities such as R_1, R_{chem}, C_{chem}, t_{chem} can be extrapolated.

Regarding t_{chem}, this quantity is directly proportional to the vacancies concentration as reported in the following equation:

$$t_{chem} = \frac{c_v(1-\epsilon)}{Aar_0(\alpha_f+\alpha_b)} \qquad (3.14)$$

where c_v is the oxygen vacancies concentration, ε is the porosity, A the thermodynamic factor, *a* the surface area, r_0 the exchange neutral flux density and finally α_f and α_b are the constants of order od unit that depend on the specific mechanism of the exchange reaction.

From Eq. 3.12, only c_v and A (which is inversely proportional to $\ln(c_v)$, can be considered as variable in this punctual measurements, then the trend of t_{chem} is useful to describe the change of vacancy concentration. Fig. 3. 22 reports trend of t_{chem} for all the samples; the presence of LSM surface layer on LSCF scaffold produce a lower t_{chem} value, suggesting an initial increase in oxygen vacancy concentration. Applying a bias t_{chem} grows up due to the formation of new oxygen vacancies as proposed above.

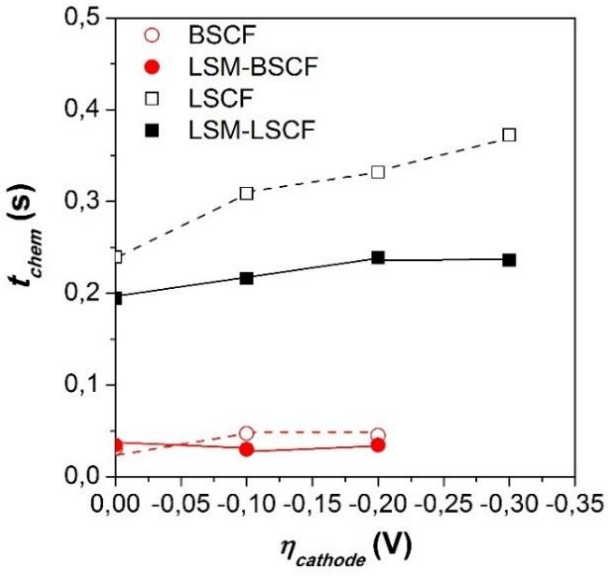

Fig. 3. 22 Time constant trends as function of the overpotential obtained from the fitting parameters for reference and infiltrated electrodes.

Results from Fig. 3. 22 also confirm that BSCF has a higher oxygen surface activity than LSCF, with a consequent lower t_{chem}. Nevertheless the application of cathodic overpotential does not affect this parameter for BSCF – based electrodes.

Gerischer element provides new information regarding R_{chem} and C_{chem} as illustrated in Fig. 3. 23 (a) and (b). R_1 is related with the ion transfer at electrode/electrolyte interface and is presented only for the reference LSCF. R_{chem} is associated with the process at electrode surface, while as already suggested C_{chem} represents concentration of ion carries. This cathodic behavior with formation of new vacancies occurs both on LSCF and LSM material, and for this reason LSM-infiltrated LSCF has a higher decreasing in R_P than reference one.

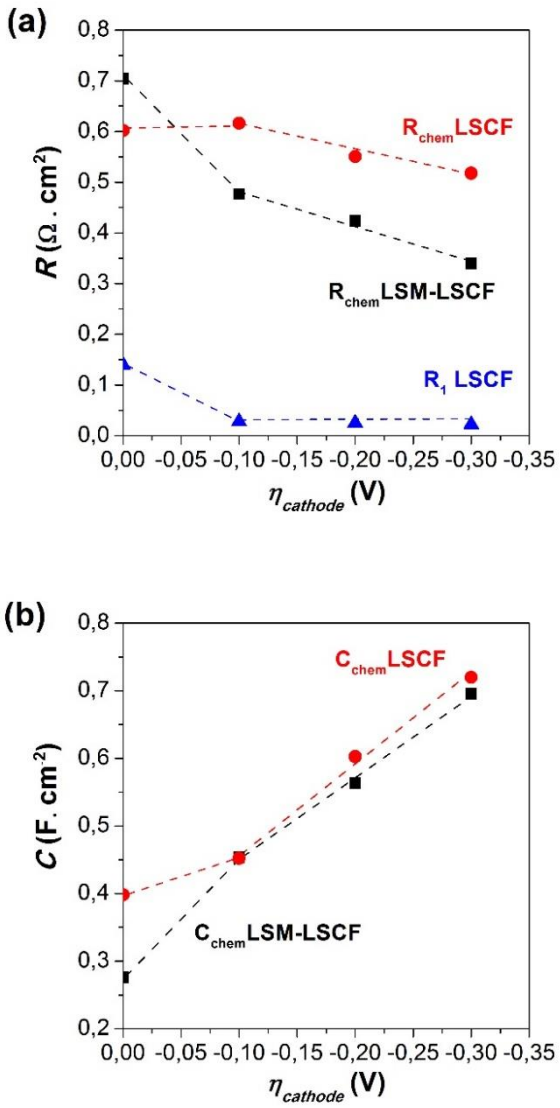

Fig. 3. 23 (a) Resistance and **(b)** chemical capacitance as a function of overpotentials for LSCF – based cathodes.

BSCF – based electrodes have a completely opposite behavior. R_{chem} and C_{chem} rises up and falls down, respectively, as a function of overpotential as illustrated in Fig. 3. 24. A possible explanation is that under cathodic overpotential the large amount of vacancies available in BSCF electrode decrease due to their agglomeration that decrease the c_v available for oxygen reduction process. Nevertheless, also for BSCF the presence of LSM is positive, lowering the worsening performance for infiltrated cathode.

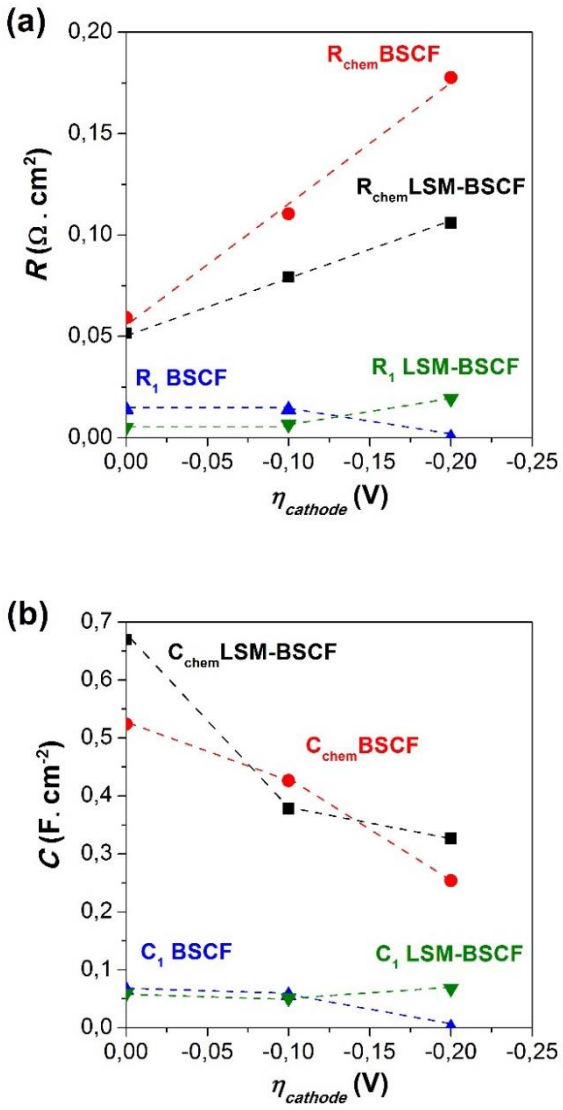

Fig. 3. 24 (a) Resistance and **(b)** chemical capacitance as a function of overpotentials for BSCF – based cathodes.

The last, but fundamental step, was the evaluation of stability of infiltrated electrodes under operating conditions. Reference and infiltrated cathode were tested under a cathodic current load of 200 mA cm^{-2} at 700 °C and at 21% of oxygen partial pressure. Periodically the current was interrupted to evaluate degradation by means EIS measurements Fig. 3. 25.

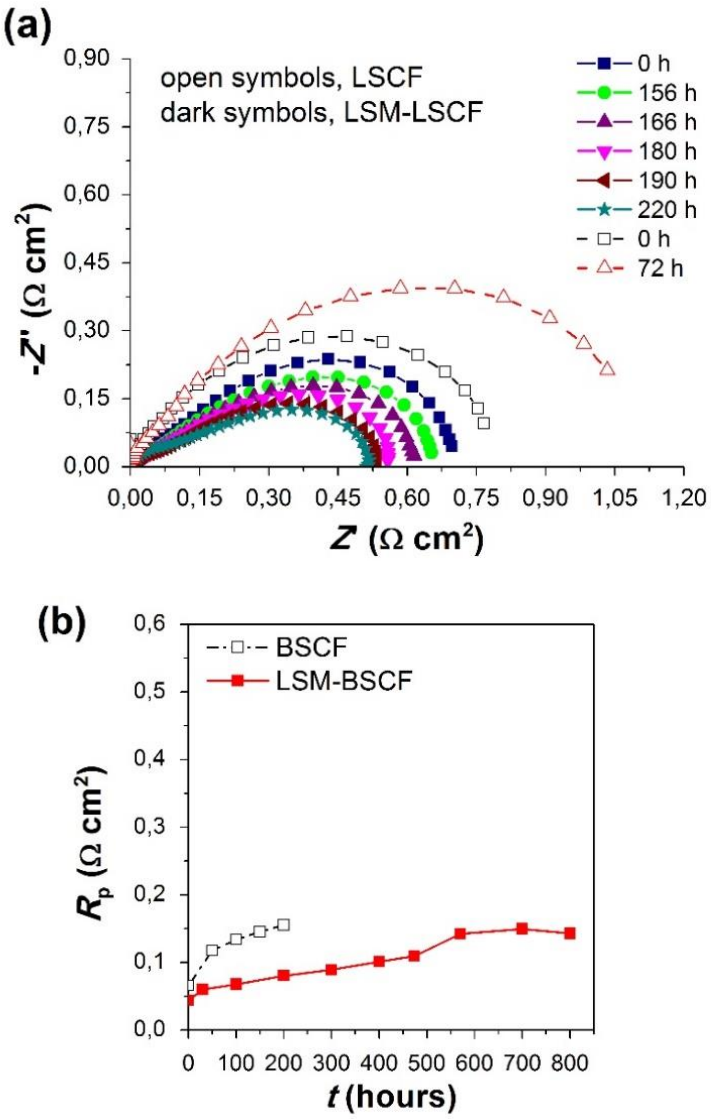

Fig. 3. 25 Degradation behavior of **(a)** LSCF and LSM – LSCF and **(b)** BSCF and LSM – BSCF electrodes during the ageing test under cathodic current load of 200 mA cm^{-2} at 700 °C and 21% O_2 partial pressure.

LSCF electrode show a strong R_P increase (29% of degradation) in the first 72 hours, and this degradation rate is in agreement with literature values (7, 56-59). For infiltrated LSCF sample, R_P progressively decreases reaching a final value of 0.51 Ω cm^2, with a gain close 26% (initial R_P is 0.7 Ω cm^2). The enhancement of performance can be ascribed to an effect of the current on LSM structure; it has been proven that the

application of a cathodic current causes a modification of LSM porosity and of its microstructure (35, 58).

LSM effect on BSCF is noteworthy, because even if it is not able to prevent degradation phenomena on BSCF electrode, it can decrease degradation rate. In fact in the first 200 hours the blank BSCF electrode has a degradation of 98% (from 0.081 Ω cm^2 to 0.16 Ω cm^2), while the infiltrated one stop to 74% (0.046 Ω cm^2 up to 0.08 Ω cm^2). The R_P of 0.16 Ω cm^2 obtained for the reference BSCF electrode after 200 hours has been measured only after 800 hours of ageing test for the LSM-infiltrated BSCF sample.

The results presented in this last section show how the features of LSM can be still exploit in SOFC cathode to improve performance and stability of other electrocatalytic materials.

3.5 Summary

The results presented in this chapter underline that with a tailored electrode microstructure LSM-based electrode can be exploited as cathode material for SOFCs. In fact. Its electrocatalytic activity is also strongly affected by operating conditions which influence the path followed by oxygen reduction reaction.

Firstly, impedance measurements carried out with different cell geometry confirm the key role played by it in order to obtain reliable measurements, in particular under overpotential application.

As regards oxygen reduction reaction mechanism, it is controlled by two predominant phenomena such as a charge transfer process at high frequency and a transport process at medium-low frequency range. The contribution of these processes on the global resistance change as a function of operating conditions (temperature and applied overpotential).

Among the parameters, overpotential has a remarkable effect on the determination of the main process, and analysis of impedance measurements highlights an increase of ionic transport with the activation of electrode bulk pathway for bias

higher than 0.2 V. This mechanism transition is identified coupling the distribution of relaxation time (DRT) and equivalent circuit (EC) analysis. Both identified two main processes at high and low frequency range, respectively. In accordance with literature. Moreover the analysis is refined introducing a geometric index (GI) which considers the penetration of oxygen reduction reaction from the TPB to LSM-YSZ contact area.

Conclusions of experimental part were confirmed by a physically-based model developed with a collaboration with the Department of Civil and Industrial Engineering of University of Pisa. Model based on a co-limited adsorption/diffusion of oxygen and charge-transfer at TPB process, is able to describe experimental data for an overpotential lower than 0.2 V. For higher values model diverge from experimental impedance data suggesting a bulk path activation, not considered in the model itself.

In the final part of this Chapter, infiltration of LSCF and BSCF scaffold has been presented as a strategy to exploit LSM properties for IT – SOFC cathodes. Results are promising both for performance and stability, in particular for LSCF – based electrode. In fact, for this material LSM infiltration caused a decreasing of polarization resistance and an improvement of electrode stability, due to the presence of infiltrated phase on the electrode surface. Results on BSCF electrode show a positive effect, even if for such material degradation is not blocked but only limited. Nevertheless the presence of LSM as discrete thin film at electrode surface can be extremely useful to control electrode degradation.

3.6 References

1. F. Dong, M. Ni, Y. Chen, D. Chen, M. O. Tadé and Z. Shao, *Journal of Materials Chemistry A*, **2**, 20520 (2014).
2. F. Dong, M. Ni, W. He, Y. Chen, G. Yang, D. Chen and Z. Shao, *Journal of Power Sources*, **326**, 459 (2016).
3. B. Liu, Y. Zhang and L. Zhang, *International Journal of Hydrogen Energy*, **34**, 1008 (2009).
4. E. Mutoro, E. J. Crumlin, M. D. Biegalski, H. M. Christen and Y. Shao-Horn, *Energy & Environmental Science*, **4**, 3689 (2011).
5. D. Rembelski, J. P. Viricelle, L. Combemale and M. Rieu, *Fuel Cells*, **12**, 256 (2012).
6. Z. Shao and S. M. Haile, *Nature*, **431**, 170 (2004).
7. S. P. Simner, M. D. Anderson, M. H. Engelhard and J. W. Stevenson, *Electrochemical and Solid-State Letters*, **9**, A478 (2006).
8. L. Wang, R. Merkle and J. Maier, *Journal of The Electrochemical Society*, **157**, B1802 (2010).
9. K. V. Hansen, K. Norrman, T. Jacobsen, Y. Wu and M. B. Mogensen, *Journal of The Electrochemical Society*, **162**, F1165 (2015).
10. T. M. Huber, M. Kubicek, A. K. Opitz and J. Fleig, *Journal of The Electrochemical Society*, **162**, F229 (2015).
11. E. Navickas, T. M. Huber, Y. Chen, W. Hetaba, G. Holzlechner, G. Rupp, M. Stöger-Pollach, G. Friedbacher, H. Hutter, B. Yildiz and J. Fleig, *Physical Chemistry Chemical Physics*, **17**, 7659 (2015).
12. A. K. Opitz, M. Kubicek, S. Huber, T. Huber, G. Holzlechner, H. Hutter and J. Fleig, *Journal of Materials Research*, **28**, 2085 (2013).
13. S. Wang, X. Lu and M. Liu, *Journal of Solid State Electrochemistry*, **6**, 384 (2002).
14. E. C. Thomsen, G. W. Coffey, L. R. Pederson and O. A. Marina, *Journal of Power Sources*, **191**, 217 (2009).
15. A. C. Co and V. I. Birss, *The Journal of Physical Chemistry B*, **110**, 11299 (2006).
16. M. Cimenti, A. C. Co, V. I. Birss and J. M. Hill, *Fuel Cells*, **7**, 364 (2007).
17. H. Lauret and A. Hammou, *Journal of the European Ceramic Society*, **16**, 447 (1996).

18. A. Sanson, E. Mercadelli, E. Roncari, R. Licheri, R. Orrù, G. Cao, E. Merlone-Borla, D. Marzorati, A. Bonavita, G. Micali and G. Neri, *Ceramics International*, **36**, 521 (2010).

19. A. Esquirol, N. P. Brandon, J. A. Kilner and M. Mogensen, *Journal of The Electrochemical Society*, **151**, A1847 (2004).

20. K. Miyoshi, T. Miyamae, H. Iwai, M. Saito, M. Kishimoto and H. Yoshida, *Journal of Power Sources*, **315**, 63 (2016).

21. R. Herger, P. R. Willmott, C. M. Schlepütz, M. Björck, S. A. Pauli, D. Martoccia, B. D. Patterson, D. Kumah, R. Clarke, Y. Yacoby and M. Döbeli, *Physical Review B*, **77**, 085401 (2008).

22. H. Jalili, Y. Chen and B. Yildiz, *Journal of Physics: Condensed Matter*, **28**, 60301 (2016).

23. A. Bertei, B. Nucci and C. Nicolella, *Chemical Engineering Science*, **101**, 175 (2013).

24. J.-h. Myung, H. J. Ko, H.-G. Park, M. Hwan and S.-H. Hyun, *International Journal of Hydrogen Energy*, **37**, 498 (2012).

25. F. Tietz, H. P. Buchkremer and D. Stöver, *Solid State Ionics*, **152-153**, 373 (2002).

26. J. Fleig, *Journal of Power Sources*, **105**, 228 (2002).

27. T. Horita, K. Yamaji, N. Sakai, Y. Xiong, T. Kato, H. Yokokawa and T. Kawada, *Journal of Power Sources*, **106**, 224 (2002).

28. A. Bertei, A. Barbucci, M. P. Carpanese, M. Viviani and C. Nicolella, *Chemical Engineering Journal*, **207-208**, 167 (2012).

29. M. Gong, R. S. Gemmen and X. Liu, *Journal of Power Sources*, **201**, 204 (2012).

30. M. Gong, R. S. Gemmen, D. S. Mebane, K. Gerdes and X. Liu, *Journal of The Electrochemical Society*, **161**, F344 (2014).

31. B. Kenney and K. Karan, *Journal of The Electrochemical Society*, **157**, B1126 (2010).

32. E. A. Kotomin, Y. A. Mastrikov, E. Heifets and J. Maier, *Physical Chemistry Chemical Physics*, **10**, 4644 (2008).

33. S. B. Adler, *Chemical Reviews*, **104**, 4791 (2004).

34. F. H. van Heuveln, H. J. M. Bouwmeester and F. P. F. van Berkel, *Journal of The Electrochemical Society*, **144**, 126 (1997).

35. X. J. Chen, K. A. Khor and S. H. Chan, *Solid State Ionics*, **167**, 379 (2004).

36. E. Siebert, A. Hammouche and M. Kleitz, *Electrochimica Acta*, **40**, 1741 (1995).

37. D. Mantzavinos, A. Hartley, I. S. Metcalfe and M. Sahibzada, *Solid State Ionics*, **134**, 103 (2000).

38. J. T. S. Irvine, D. Neagu, M. C. Verbraeken, C. Chatzichristodoulou, C. Graves and M. B. Mogensen, *Nature Energy*, **1**, 15014 (2016).

39. A. M. Svensson, S. Sunde and K. Nis¸ancioĞlu, *Journal of The Electrochemical Society*, **145**, 1390 (1998).

40. V. Brichzin, J. Fleig, H. U. Habermeier, G. Cristiani and J. Maier, *Solid State Ionics*, **152-153**, 499 (2002).

41. A. Bertei, M. P. Carpanese, D. Clematis, A. Barbucci, M. Z. Bazant and C. Nicolella, *Solid State Ionics*, **303**, 181 (2017).

42. M. Z. Bazant, *Accounts of Chemical Research*, **46**, 1144 (2013).

43. A. Giuliano, M. P. Carpanese, D. Clematis, M. Boaro, A. Pappacena, F. Deganello, L. F. Liotta and A. Barbucci, *Journal of The Electrochemical Society*, **164**, F3114 (2017).

44. F. Deganello, L. F. Liotta, G. Marcì, E. Fabbri and E. Traversa, *Materials for Renewable and Sustainable Energy*, **2**, 8 (2013).

45. S. Lee, Y. Lim, E. A. Lee, H. J. Hwang and J.-W. Moon, *Journal of Power Sources*, **157**, 848 (2006).

46. S. B. Adler, J. A. Lane and B. C. H. Steele, *Journal of The Electrochemical Society*, **143**, 3554 (1996).

47. A. Flura, C. Nicollet, V. Vibhu, B. Zeimetz, A. Rougier, J.-M. Bassat and J.-C. Grenier, *Journal of The Electrochemical Society*, **163**, F523 (2016).

48. F. S. Baumann, J. Fleig, H. U. Habermeier and J. Maier, *Solid State Ionics*, **177**, 3187 (2006).

49. J. Jamnik and J. Maier, *Physical Chemistry Chemical Physics*, **3**, 1668 (2001).

50. W. Lai and S. M. Haile, *Journal of the American Ceramic Society*, **88**, 2979 (2005).

51. C. R. Kreller, T. J. McDonald, S. B. Adler, E. J. Crumlin, E. Mutoro, S. J. Ahn, G. J. la O', Y. Shao-Horn, M. D. Biegalski, H. M. Christen, R. R. Chater and J. A. Kilner, *Journal of The Electrochemical Society*, **160**, F931 (2013).

52. M. Kuhn, Y. Fukuda, S. Hashimoto, K. Sato, K. Yashiro and J. Mizusaki, *Journal of The Electrochemical Society*, **160**, F34 (2013).

53. D. N. Mueller, M. L. Machala, H. Bluhm and W. C. Chueh, *Nature Communications*, **6**, 6097 (2015).

54. S. Gangopadhyay, A. E. Masunov, T. Inerbaev, J. Mesit, R. K. Guha, A. K. Sleiti and J. S. Kapat, *Solid State Ionics*, **181**, 1067 (2010).

55. E. V. Tsipis, E. N. Naumovich, M. V. Patrakeev, A. A. Yaremchenko, I. P. Marozau, A. V. Kovalevsky, J. C. Waerenborgh and V. V. Kharton, *Solid State Ionics*, **192**, 42 (2011).

56. L. dos Santos-Gómez, J. M. Porras-Vázquez, E. R. Losilla, F. Martín, J. R. Ramos-Barrado and D. Marrero-López, *Journal of Power Sources*, **347**, 178 (2017).

57. Z.-P. Li, M. Toshiyuki, G. J. Auchterlonie, J. Zou and D. John, *ACS Applied Materials & Interfaces*, **3**, 2772 (2011).

58. M. Shah, P. W. Voorhees and S. A. Barnett, *Solid State Ionics*, **187**, 64 (2011).

59. H. Yokokawa, H. Tu, B. Iwanschitz and A. Mai, *Journal of Power Sources*, **182**, 400 (2008).

Appendix to section 3.2.4

In this appendix model equations developed by Dr. Bertei (Department of Civil and Industrial Engineering, University of Pisa) are reported with a brief comment. System boundary are identified at x = 0 (electrode/electrolyte interface) and at x = L_c (cathode thickness).

The Faradic contribution of the charge – transfer reaction occur at the TPB (x=0) and follows Butler – Volmer kinetic:

$$i_{TPB} = i_{00}\left(\frac{\theta_0}{1-\theta_0}\right)^{1-\alpha}\left\{exp\left[\alpha\frac{2F}{RT}\eta_{act}\right] - exp\left[-(1-\alpha)\frac{2F}{RT}\eta_{act}\right]\right\} \quad \text{(A3.1)}$$

$$\eta_{act} = -\frac{RT}{2F}ln\left(\frac{\theta_{eq}}{\theta_0}\frac{1-\theta_0}{1-\theta_{eq}}\right) - (V_{el} - V_{io}) \quad \text{(A3.2)}$$

LSM surface is treated as an ideal solution of free sites and adsorbed oxygen atoms, with activity equal to:

$$a_\theta = \frac{\theta}{1-\theta} \quad \text{(A3.3)}$$

Activation overpotential η_{act} is considered positive for cathodic current production and it takes into account the equilibrium potential difference (basically a concentration contribution). The difference $(V_{el} - V_{io})$ calculated at x=0 represents the overall overpotential applied to the cathode η_{cat}, because of the electron transport is neglected. η_{cat} in EIS model is the sum of a steady-state dc overpotential, η_{bias} and a sinusoidal ac perturbation $\Delta\eta_{ac}\cdot e^{j\omega t}$. Moreover due to the small contribution of activation overpotential, Butler – Volmer equations (A3.1) and (A3.2) can be simplified as:

$$i_{TPB} = i_{00}\left(\frac{\theta_0}{1-\theta_0}\right)^{1-\alpha}\frac{2F}{RT}\eta_{act} \quad \text{(A3.4)}$$

$$\eta_{act} = -\frac{RT}{2F}ln\left(\frac{\theta_{eq}}{\theta_0}\frac{1-\theta_0}{1-\theta_{eq}}\right) + \eta_{cat} \quad \text{(A3.5)}$$

With $\eta_{cat} = \eta_{bias} + \Delta\eta_{ac}\cdot e^{j\omega t}$

Oxygen dissociative adsorption and Fick surface diffusion were considered, and the conservation of adsorbed oxygen atoms along cathode thickness is:

$$\Gamma a_{el}^{v} = -\frac{\partial N_O^{surf}}{\partial x} + \Gamma a_{el}^{v} k_{des}(Kp_{O2}(1-\theta)^2 - \theta^2) \quad \text{(A3.6)}$$

$$N_O^{surf} = -\Gamma a_{el}^{v} D_s^{eff} \frac{\partial \theta}{\partial x} \quad \text{(A3.7)}$$

Eq. (A3.6) is the flux of adsorbed oxygen atoms per unit of electrode area. Γ is the number of adsorption sites per unit of LSM surface area, while a_{el}^{v} is the LSM surface area exposed to gas phase per unit of electrode volume. D_s^{eff} is the effective diffusivity and takes into account the surface diffusivity of oxygen adatoms corrected for surface tortuosity factor ($D_s^{eff} = D_s/\tau_s$)

The boundary conditions related with previous equations are:

$$x = 0 \quad N_O^{surf} = -\frac{i_{TPB}\lambda_{TPB}^{s}}{2F} - \frac{c_{TPB}\lambda_{TPB}^{s}}{2F}\frac{\partial \eta_{act}}{\partial t} \quad \text{(A3.8)}$$

$$x = L_c \;\; N_O^{surf} = 0 \quad \text{(A3.9)}$$

Eq. (A3.8) describes the flux that reaches the TPB is converted into two contributions: the first, a Faradaic contribution (related to charge – transfer reaction) and a capacitive contribution (formation of reaction intermediates at TPB). Both terms are assumed to be proportional to TPB length per unit of interfacial area between electrode and electrolyte.

Langmuir equilibrium defined the equilibrium surface coverage θ_{eq}at open circuit:

$$\theta_{eq} = \frac{\sqrt{Kp_{O2}}}{1+\sqrt{Kp_{O2}}} \quad \text{(A3.10)}$$

The current crossing the electrode/electrolyte interface is equal to the electrochemical contribution (Eq. (A3.8)), added to the current associated with the electric double-layer capacitance:

$$I = -N_O^{surf}\big|_{x=0} 2F + c_{dl} a_{dl}^{s} \frac{\partial (V_{io} - V_{el})}{\partial t} \quad \text{(A3.11)}$$

The steady-state solution neglects the time-dependent terms and provide the electrode response to the dc overpotential. Then, the related steady-solutions represented with a bar sign, solves the following equations:

$$0 = -\frac{d\bar{N}_O^{surf}}{dx} + \Gamma a_{el}^v k_{des}(Kp_{O2}(1-\theta)^2 - \theta^2) \quad \text{(A3.12)}$$

$$\bar{N}_O^{surf} = -\Gamma a_{el}^v D_s^{eff} \frac{\partial \bar{\theta}}{\partial x} \quad \text{(A3.13)}$$

$$x = 0\text{: } \bar{\imath}_{TPB} = i_{00}\left(\frac{\bar{\theta}_0}{1-\bar{\theta}_0}\right)^{1-\alpha} \frac{2F}{RT}\bar{\eta}_{act} \quad \text{(A3.14)}$$

$$\bar{\eta}_{act} = -\frac{RT}{2F} ln\left(\frac{\theta_{eq}}{\bar{\theta}_0}\frac{1-\bar{\theta}_0}{1-\theta_{eq}}\right) + \eta_{bias} \quad \text{(A3.15)}$$

$$\bar{N}_O^{surf} = -\frac{\bar{\imath}_{TPB}\lambda_{TPB}^s}{2F} \quad \text{(A3.16)}$$

$$x = L_c\text{: } \bar{N}_O^{surf} = 0 \quad \text{(A3.17)}$$

and allows for the calculation of dc current density circulating in the cathode upon the application of the bias η_{bias}, as follows:

$$\bar{I} = -\bar{N}_O^{surf}\big|_{x=0} 2F = \bar{\imath}_{TPB}\lambda_{TPB}^s \quad \text{(A3.18)}$$

Set equations just introduced is converted in frequency domain to compute electrode impedance. A small sinusoidal perturbation $\Delta\eta_{ac}$ to the cathode overpotential produces a small perturbation of $\Delta\theta$, $\Delta\eta_{act}$, Δi_{TPB}, ΔN_O^{surf} and then ΔI.

For a generic variable ξ the perturbation $\Delta\xi$ is defined as the local deviation from steady-state solution:

$$\xi - \bar{\xi} = \delta\xi \cdot e^{j(\omega t+\phi)} = \Delta\xi \cdot e^{j\omega t} \text{ with } \delta\xi \ll \bar{\xi} \quad \text{(A3.19)}$$

After linear Taylor expansion and upon subtraction of the steady – state solution, the system of equation in frequency domains results as follows:

$$j\omega\Gamma a_{el}^v \Delta\theta = -\frac{d\Delta N_O^{surf}}{dx} - 2\Gamma a_{el}^v k_{des}(Kp_{O2} + \bar{\theta}\,(1 - Kp_{O2}))\Delta\theta \quad \text{(A3.20)}$$

$$\Delta N_O^{surf} = -\Gamma a_{el}^v D_s^{eff} \frac{\partial \Delta\theta}{\partial x} \quad \text{(A3.21)}$$

$$x = 0\text{: } \Delta i_{TPB} = i_{00}\left(\frac{\bar{\theta}_0}{1-\bar{\theta}_0}\right)^{1-\alpha} \frac{2F}{RT}\Delta\eta_{act} + i_{00}\frac{(1-\alpha)}{\left(\frac{\bar{\theta}_0}{1-\bar{\theta}_0}\right)^{\alpha}(1-\bar{\theta}_0)^2}\frac{2F}{RT}\bar{\eta}_{act}\Delta\theta_0 \quad \text{(A3.22)}$$

$$\Delta\eta_{act} = \frac{RT}{2F}\frac{1}{\bar{\theta}_0(1-\bar{\theta}_0)}\Delta\theta_0 + \Delta\eta_{ac} \quad \text{(A3.23)}$$

$$\Delta N_O^{surf} = -\frac{\Delta i_{TPB}\lambda_{TPB}^S}{2F} - j\omega\frac{c_{TPB}\lambda_{TPB}^S}{2F}\Delta\eta_{act} \quad \text{(A3.24)}$$

$$x = L_c: \Delta N_O^{surf} = 0 \quad \text{(A3.25)}$$

The current perturbation is calculated as:

$$\Delta I = -\Delta N_O^{surf}\big|_{x=0} 2F + j\omega c_{dl} a_{dl}^S \Delta\eta_{ac} \quad \text{(A3.26)}$$

Then the impedance is determined as the ratio between the ac voltage perturbation and the current perturbation:

$$Z(\omega) = Z_{Re}(\omega) + jZ_{Im}(\omega) = \frac{\Delta\eta_{ac}}{\Delta I} \quad \text{(A3.27)}$$

CHAPTER 4

BSCF and LSCF: Looking the stability, preserving performance*

HIGHLIGHTS

- *$La_{0.6}Sr_{0.4}Co_{0.2}Fe_{0.8}O_{3-\delta}$ (LSCF) and $Ba_{0.5}Sr_{0.5}Co_{0.8}Fe_{0.2}O_{3-\delta}$ (BSCF) were mixed in different volume ratio to exploit their properties and improve stability*
- *LSCF and BSCF react during sintering stage.*
- *New electrode materials show a performance improvement with very low polarization resistance*
- *A transition in kinetic regime has been identified by Distribution of Relaxation Times and confirmed by Equivalen Circuit Models.*

* The content of this Chapter has been published in:

- *Electrochimica Acta, Volume 240 , 2017, Pages 258-266*
- *International Journal of Hydrogen Energy, 2019, Accepted*

4.1 Introduction

High electrocatalytic activity for oxygen reduction reaction (ORR) and slow degradation rate are two extremely important requirements in cathodes for intermediate temperature - solid oxide fuel cells (IT-SOFC). The main question, still unanswered, is whether it is possible to meet both of them in the same system. Many studies have been dedicated to the development of new materials, and in particular perovskites are attractive because of their high ionic and electronic conductivity, as well as for their high oxygen surface exchange coefficient (1-11). $La_{0.6}Sr_{0.4}Co_{0.2}Fe_{0.8}O_{3-\delta}$ (LSCF) and $Ba_{0.5}Sr_{0.5}Co_{0.8}Fe_{0.2}O_{3-\delta}$ (BSCF) are among the most studied perovskites for electrochemical application. In detail, LSCF is attractive for its high electronic and good ionic conductivities (12). However, at the operating temperature of zirconia-based SOFC, cation inter-diffusion (La, Sr) causes the formation of insulating phases such as $La_2Zr_2O_7$ or $SrZrO_3$, which negatively affect performance (13-18).

On the other hand, BSCF, which has a lower electronic conductivity if compared to LSCF, is very active toward ORR owing to its high oxygen vacancies concentration and oxygen diffusion rate, larger than 2 to 200 times the values of other perovskites (19, 20). However, BSCF is penalised by structural instability below 900 °C, with formation of different phases with cubic or hexagonal symmetry and with lower activity for oxygen reduction (21, 22). Besides, it is affected by carbonate formation in the presence of CO_2 (23), resulting in electrode deactivation (24, 25). Reaction with CO_2 reduces the ability of BSCF for oxygen transport (24) and is attributed to the presence of Ba bonds (25).

The approaches applied to reduce cation diffusion and/or phase transition of LSCF and BSCF are different, among these it is noteworthy to recall: (i) surface modification by means of infiltration by a second phase (26-28), (ii) introduction of A-site deficiency (12, 29, 30), (iii) in situ polarization-exsolution treatment (31), iv) use of composite electrodes to stabilise different phases (32, 33). While these methods have general applications a further strategy previously applied by some of the authors (34) and rarely reported in literature (35) is pursued in this paper.

It consists in the mixing of LSCF and BSCF in order to take advantage of their strengths and reciprocally compensate their aforementioned drawbacks. Solid state

inter-diffusion of elements during electrode sintering and even at operating temperature is expected to take place with possible formation of new phases. However, partial substitution of Barium with Lanthanum in BSCF has been reported as a reliable way to stabilize the cubic structure (36). Moreover, the mentioned preliminary investigation (34) has shown promising results. For these reasons, the system deserves a further investigation in order to have confirmation of the obtained results and to obtain new data on different LSCF/BSCF ratios.

It should be highlighted that, once proven high and stable activity toward ORR, further enhancement of the sought electrochemical properties might be obtained by applying some of the listed general methods, for instance infiltration.

Then, this study deals with structure, performance and stability of LSCF-BSCF-based cathodes. The structure and morphology of the electrodes were investigated by X-ray diffraction (XRD) and Scanning Electronic Microscopy (SEM). Electrochemical impedance spectroscopy (EIS) measurements at different temperatures and cathodic overpotentials were carried out to study the electrode performance and ORR kinetic mechanism. Ageing tests in simulated cathodic condition of operation were also performed to compare stability over time.

4.2 Experimental

Mixture of $Ba_{0.5}Sr_{0.5}Co_{0.8}Fe_{0.2}O_{3-\delta}$ (BSCF, Treibacher Industrie AG) and $La_{0.6}Sr_{0.4}Co_{0.2}Fe_{0.8}O_{3-\delta}$ (LSCF, FuelCell Materials) commercial powders with three different volume ratios 50-50 v/v% (BL50), 70-30 v/v% (BL70) and 30-70 v/v% (BL30), were prepared through low energy ball milling in distilled water for 20 h at room temperature. For each mixture (15 g in a 100 ml PE bottle), 5 g of distilled water was added and zirconia beads of three different diameters were used for ball milling: ϕ=15 mm (active material/zirconia mass ratio 1:2), ϕ=10 mm (active material/zirconia mass ratio 1:2.4) and ϕ=5 mm (active material/zirconia mass ratio 1:2.6).

After milling, the powders were freeze dried for 24 hours at -50 °C and 0.01 mbar (Labconco FreeZone 2.5) and sieved for 30 minutes to be separated from beads.

$Ce_{0.8}Sm_{0.2}O_{2-\delta}$ powder (SDC20 – HP Fuel Cell Materials) was used for electrolyte preparation; it was cold pressed at 60 MPa, sintered in one step at 1450°C for 5 hours in air, resulting in electrolyte disks with a diameter of 25 mm and a thickness of 1.2 mm.

An ink for slurry coating of the electrode on the electrolyte disks was prepared mixing the above powders in a mortar with alpha-therpineol (techn grade 90%, Sigma Aldrich; 50 drops in 15 g of powder). Cells were prepared in the three-electrode configuration and symmetry between working electrode (WE) and counter electrode (CE) was achieved by using a home-made mask system. The reference electrode (RE) was placed on the WE side of the cell at a distance of 3 times the electrolyte thickness, as suggested in the literature to avoid polarisation problems during impedance measurements (37, 38). All cathodes were sintered at 1100 °C for 2 hours, obtaining a geometric area of 0.28 cm^2 and a thickness between 50-70 μm after sintering.

In order to identify the crystalline phases and check the cathodes stability during operation, electrodes were analysed by X-ray diffraction (XRD, Cubix, Panalytical), using Cu-K_α incident radiation. Patterns were collected over the angular range $10° < 2\theta < 70°$, in a constant scan mode with steps of 0.02° and a counting time of 7 s. XRD analysis was carried out on cathodes deposited on SDC electrolyte (half cells). Polished cross sections of same samples were also analysed by Scanning Electron Microscopy (SEM, 1450-vp, LEO) and by an energy-dispersive electron microprobe (EDX, INCA 300, Oxford Instruments).

Electrochemical impedance spectroscopy (EIS) measurements were carried out in a three-electrode configuration to investigate the cathode catalytic activity; to this purpose, the cells were placed in a lab-manufactured test station (39, 40). A Pt mesh was placed on the surface of the WE and CE as current collector and Pt wires provided the connection to a potentiostat coupled to a frequency response analyser (Autolab PSSTAT302N). Impedance data were collected in the temperature range of 500 to 650°C at open circuit voltage (OCV) and at applied cathodic overpotentials (up to -0.3 V), with a perturbation of 10 mV in the 0.1-100 kHz frequency range.

Ageing tests were performed at 650 °C by applying a cathodic direct current (dc) of 200 mA cm^{-2} and checking the system evolution by impedance measurements at

OCV, after interruption of the dc load at different times. The cathode behaviour was investigated through the analysis of the impedance spectra following two different approaches: equivalent circuits (ZView® Scribner Associates Inc.) and distribution of relaxation time (DRT). In this Chapter the DRT technique was applied following Ciucci group's approach (41).

4.3 Results and discussion

4.3.1 Structural results

Fig. 4. 1 shows the XRD profile of BL30, BL50 and BL70 cathodes both as-sintered (AS) and after testing (AT). The profile of a 50-50 v/v% mixture of starting powders is also reported for comparison. The structures of starting powders are confirmed as cubic (space group: $Pm\bar{3}m$) for BSCF and trigonal (space group: $R\bar{3}c$: H) for LSCF. Fig. 4. 1 (b) focuses on one angular range where no peaks from the substrate are visible. In general, both cubic and trigonal structures can be identified in the pattern of all samples, indicated in Fig. 1b as vertical lines. In AS samples, the peaks of the trigonal structure are slightly shifted (<0.08 deg) with respect to the LSCF, while for the cubic phase a significant shift with respect to those of BSCF is observed. The 2θ shift is larger in BL30 (≅1.2 deg) than in BL50 (≅1.15 deg) and in BL70 (≅0.8 deg).

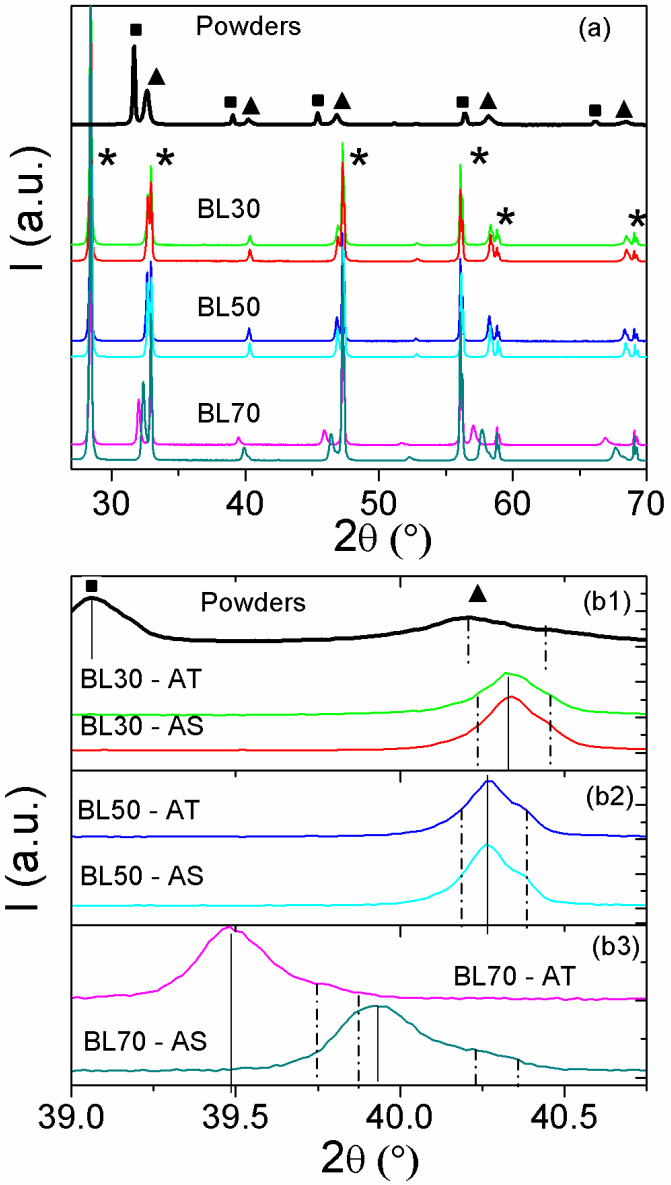

Fig. 4. 1 (a) XRD profiles of samples, listed from base to top of diagram: BL70 (AS, dark cyan), BL70 (AT, magenta), BL50 (AS, cyan), BL50 (AT, blue), BL30 (AS, red) BL30 (AT, green), Mixture of starting powders (black). AS= as sintered, AT=after electrochemical test. **(b)** Magnification. (□) = BSCF, (□) = LSCF, (*) = SDC, (—) = cubic and (— . —) = trigonal.

After testing, BL30 and BL50 are substantially unchanged. On the contrary, in BL70 the peaks of cubic phase are shifted back toward lower 2θ angles, while the trigonal phase almost disappeared (see Fig. 4. 1 (b3)).

These findings can be qualitatively explained by cationic interdiffusion between the two perovskite structures, taking place during sintering at 1100 °C. As a result, the stoichiometry of each phase might deviate from the nominal and cannot be determined from standard XRD.

Taking into account the incorporation of some smaller La^{3+} ions (r = 136 pm, CN = 12) replacing larger Sr^{2+} ions (r = 144 pm, CN = 12) at A-sites of BSCF, a unit cell volume decrease resulting in the positive shift of diffraction peaks position of the cubic structure might be expected. Similarly, the incorporation of Sr^{2+} replacing La^{3+} at A-sites of LSCF would cause lattice expansion, in this case balanced by shrinkage due to the formation of oxygen vacancies as charge compensation defect. The overall result is a small shift for the peaks of trigonal structure.

By increasing the starting volume fraction of BSCF, the cubic structure prevails with the same interdiffusion and incorporation phenomena taking place during sintering. On ageing, the observed backward shift of cubic phase peaks might be explained by progressive incorporation of La, i.e. formation of BLSCF, compensated by elimination of oxygen vacancies, causing lattice expansion.

SEM analyses showed that BL30 and BL50 electrode layers were adherent to the electrolyte substrate and with regular shape and thickness, in the range 50÷60 μm. The two phases appeared uniformly mixed although some areas with finer grain size, about 0.4 μm diameter, and others organised in larger clusters, about 2-4 μm diameter, can be observed. Given the particle size and shape of starting powders, i.e. 200 nm spherical for LSCF and about 3 μm faceted for BSCF (34), the two different morphologies observed can be respectively ascribed to LSCF-like or BSCF-like structure. Coherently, the relative amount of larger clusters increased with starting amount of BSCF.

These features were not affected by electrochemical testing and ageing and are clearly visible in Fig. 4. 2 (a) and (b). It is worth noting that the mean atomic number of $La_{0.6}Sr_{0.4}Co_{0.2}Fe_{0.8}O_3$ and $Ba_{0.5}Sr_{0.5}Co_{0.8}Fe_{0.2}O_3$, calculated by the Büchner formula, are very close and therefore will appear with the same grey tone in back scattered electron (BSE) images.

Sample BL70 showed good adhesion to the substrate (Fig. 4. 2 (c)), with irregular thickness, ranging between 50 and 70 μm. The microstructure is characterized by the presence of large clusters (> 30 μm), although about half of the volume showed grains and pores in the micron range. After testing the electrode layer was adherent to the electrolyte. Thickness was reduced, between 30 and 40 μm, due to further growth of clusters, with also formation of large voids (Fig. 4. 2 (d)). No secondary phases were detected and the composition obtained by EDX was quite homogeneous within each electrode and corresponding to the average nominal one. However, the formation of small amounts of secondary phases, below the detection limit of the technique and instrumentation used, cannot be ruled out in all samples.

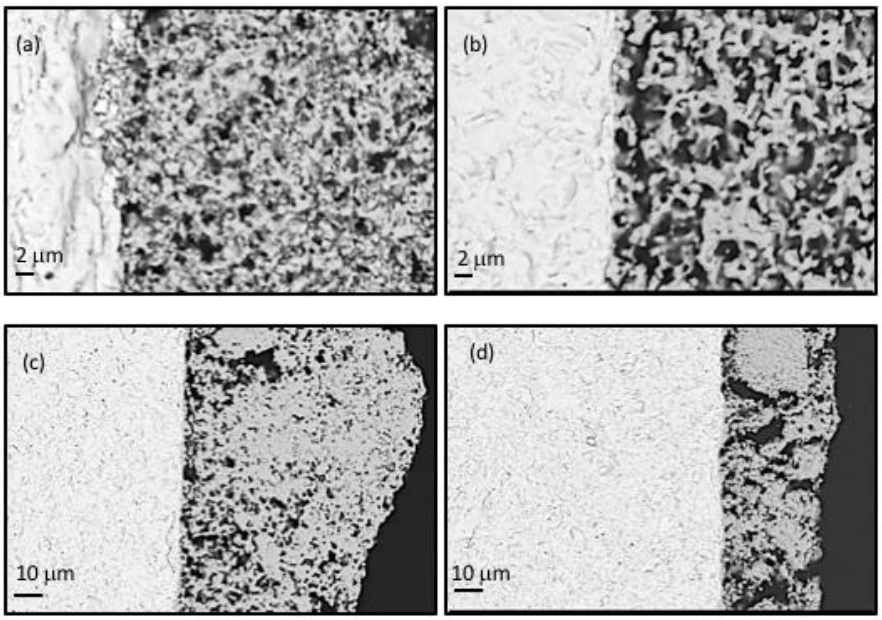

Fig. 4. 2 BSE images on cross section of samples: **(a)** BL30 as sintered, **(b)** BL50 after electrochemical testing, **(c)** BL70 as sintered and **(d)** BL70 after electrochemical testing.

4.3.2 Electrochemical results

Temperature effect

Electrochemical impedance spectroscopy investigation (EIS) was carried out in three-electrode configuration considering a temperature range between 500-650 °C (ΔT=25°C). Fig. 4. 3 (a) shows the typical impedance spectra for each composition at 650°C in air, compared to reference materials. In these operating conditions, the best performances were obtained by BL70 and BL50, with a R_P equal to 0.021 and 0.027 Ω cm^2, respectively. Nevertheless, also BL30 mixture provided a significant improvement of electrode activity with a R_P value equal to 0.045 Ω cm^2; indeed, for starting pure commercial LSCF and BSCF electrodes, measured R_P were, 0.46 Ω cm^2 and 0.21 Ω cm^2, respectively. All the R_P values obtained for new electrodes are competitive if compared with recent values reported in literature for optimized BSCF-based electrodes (42), which still remains the most active perovskite-based SOFCs cathode (2).

Activation energy (E_{act}) values calculated from Arrhenius plots are reported in Fig. 4. 3 (b). In spite of its higher resistivity, BL30 shows the lowest E_{act} (0.96eV), indicating that this composition becomes more competitive at low temperatures. The sample BL70 has an activation energy value of 1.17 eV close to the pure BSCF (1.18 eV) and lower than pure LSCF (1.52 eV), in agreement with those reported in literature (LSCF 1.45 eV (43), BSCF 1.20 eV (20, 44)). The E_{act} values confirm that all the three new compositions are prone to oxygen reduction reaction, with an enhanced electrocatalytic activity.

As reported in Fig. 4. 4, showing the Nyquist plots of sample BL70 as an example, a remarkable difference in the impedance shape was observed according to the temperature. This strong effect was detected for all the compositions and it indicates that not only polarisation resistance, but also the whole kinetic mechanism is very sensitive to this operating parameter, as confirmed by the analysis of distribution of relaxation time (DRT), performed on EIS data at OCV, and illustrated in Fig. 4. 4 (b).

This not trivial behavior prevented the use of a unique and reliable equivalent circuit able to describe all the experimental spectra in the whole temperature range. On the other hand, distribution of relaxation time (DRT) allowed recognition of the change in predominant phenomena for the two different regimes (500 and 650 °C).

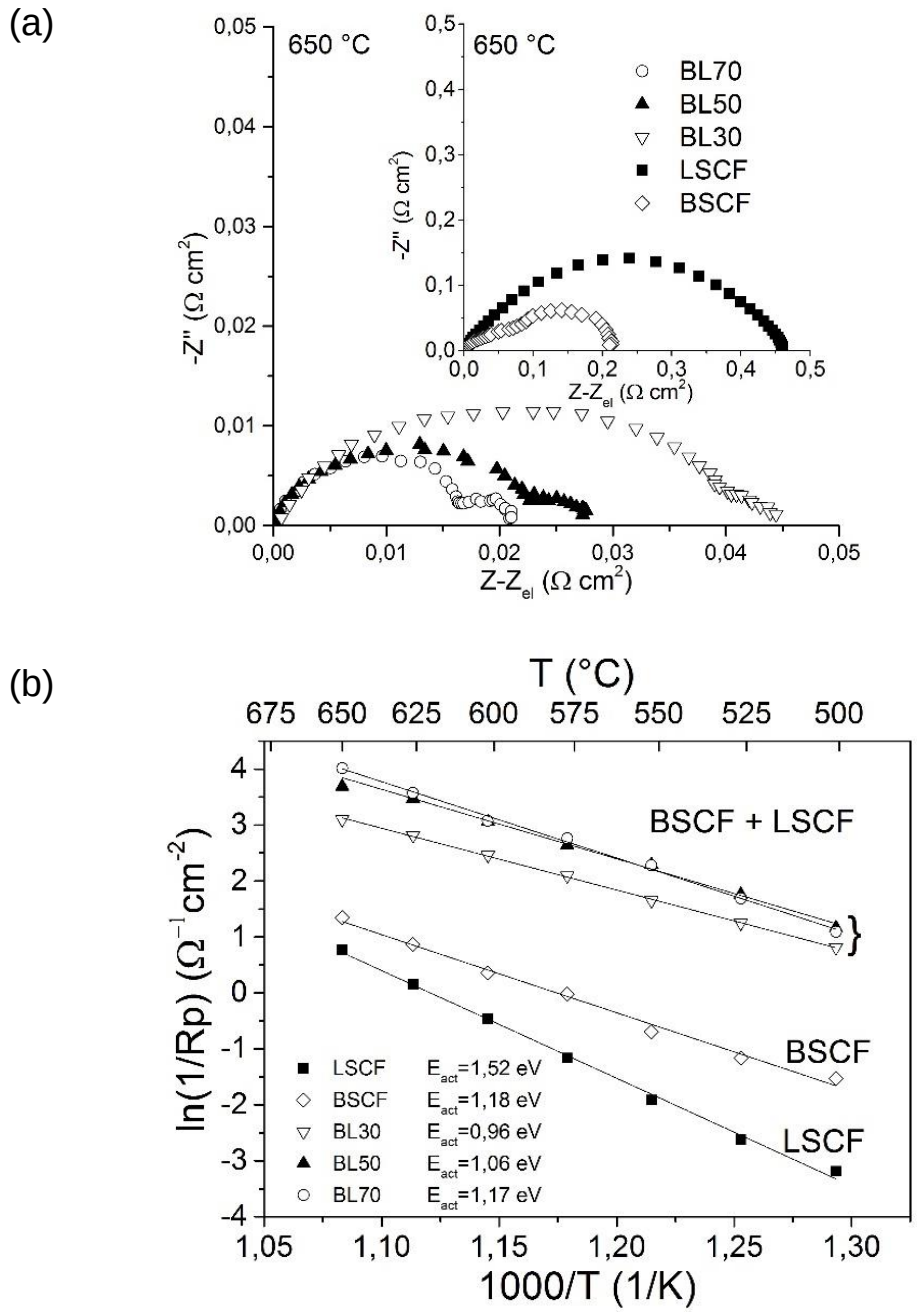

Fig. 4. 3 (a) Impedance spectra at 650 °C and OCV for BL30, BL50, BL70. The inset shows impedance spectra for pure BSCF and LSCF. **(b)** Arrhenius plot for the five cathodes and calculated activation energy: BL30 (0.95 eV), BL50 (1.06 eV), BL70 (1.17 eV), BSCF (1.18 eV) and LSCF (1.52 eV).

DRT spectra at 500°C showed a main peak at low frequencies (about 10 Hz, Fig. 4. 4 (b)), followed by a tail at medium-high frequencies. This is a typical Gerischer behavior, as reported in different studies (45, 46), which implies considering the system as co-controlled by coupled oxygen surface exchange and bulk diffusion, according to the following expression (47):

$$Z_G = R_{chem}/\sqrt{1 + j\omega t_{chem}} \quad (4.1)$$

R_{chem} being the chemical resistance and t_{chem} the characteristic time, strictly related to oxygen surface exchange and transport properties. Positive feedback for the Gerischer hypothesis came from the analysis of impedance data through an R_1G equivalent circuit fitting, as illustrated in Fig. 4. 5.

Increasing the temperature (typically at 600-650 °C) the main peak shifted to a medium-high frequency range (around 140 Hz, Fig. 4. 4 (b)) and its intensity significantly decreased, indicating a thermal activation of the process and a possible kinetic mechanism modification. Furthermore, at these higher temperatures a second well-defined peak appeared at lower frequency (around 1 Hz, Fig. 4. 4 (b)). Based on the peak frequency and data reported in literature, it is reasonable to consider this process related to surface phenomena, such as oxygen adsorption, or to oxygen diffusion at gas phase (1, 48, 49). Going more into detail, at 650 °C the total resistance decreases compared to 600 °C (Fig. 4. 4 (a)), but the area under low frequency peak (strictly linked to resistance phenomena) rises (inset in Fig. 4. 4 (b)), and its maximum value (P_{LF}) moves to lower frequencies, indicating a process hindered by the temperature increasing. The same temperature effect at low frequency was detected by Amin and Karan (50) for a $La_{0.5}Ba_{0.5}CoO_3$-based cathode; they suggested that this behavior it could be due to an unfavorable oxygen adsorption on the electrode surface, or a partial surface coverage at higher temperature. Nevertheless, the identification of the process in this frequency range is not trivial due to the complexity of the system and the multiplicity of phenomena involved, as also reported by Bidrawn et al. (51), it is extremely difficult to distinguish whether diffusion or oxygen adsorption is the rate-limiting step.

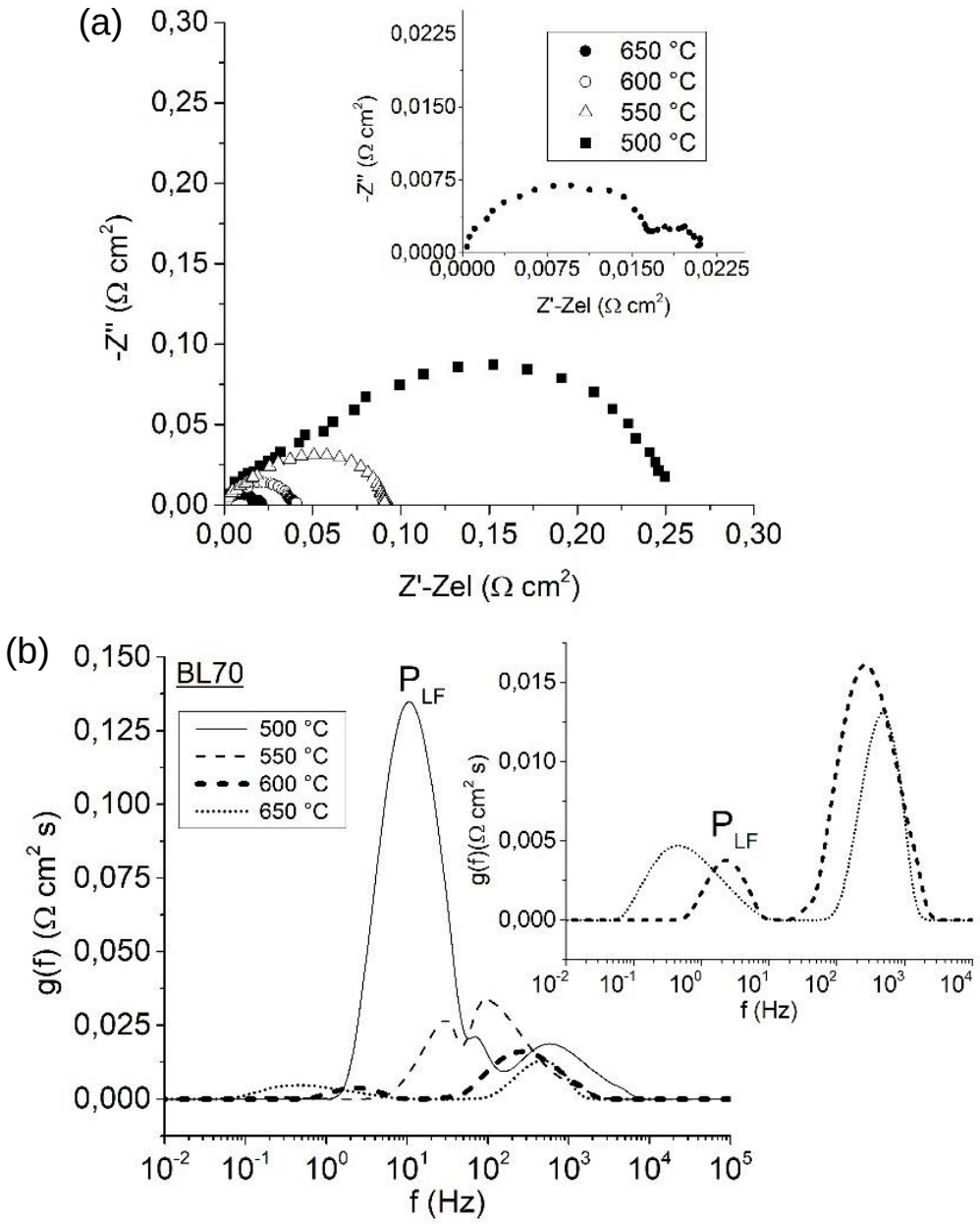

Fig. 4. 4 (a) Impedance spectra and **(b)** corresponding DRT patterns obtained for sample BL70 at OCV, in the range 500-650°C. The inset in (b) shows a magnification of the DRT curves at 600 and 650°C.

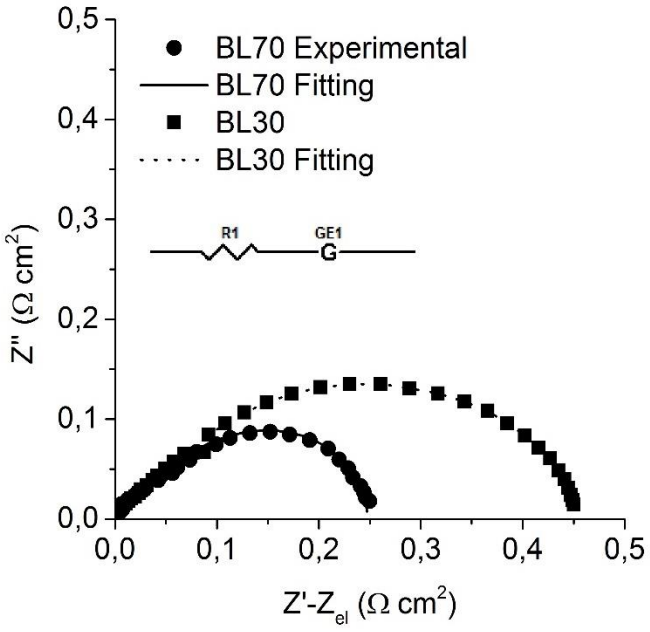

Fig. 4. 5 BL30 and BL70 cathode impedance spectra at 500°C and OCV overlaid on the fitting spectra. R_1 = (subtracted) electrolyte resistance; GE1 = Gerischer element (named G in the text).

Considering the kinetic regime change, further investigation was carried out under cathodic polarization condition in the studied range of temperature. Fig. 4. 6 reports the impedance spectra at different cathodic overpotentials (η) at 500 and 650 °C, with the matched distribution of relaxation times (insets) both for BL30 (Fig. 4. 6 (a) and (b)) and for BL70 sample (Fig. 4. 7(c) and (d)).

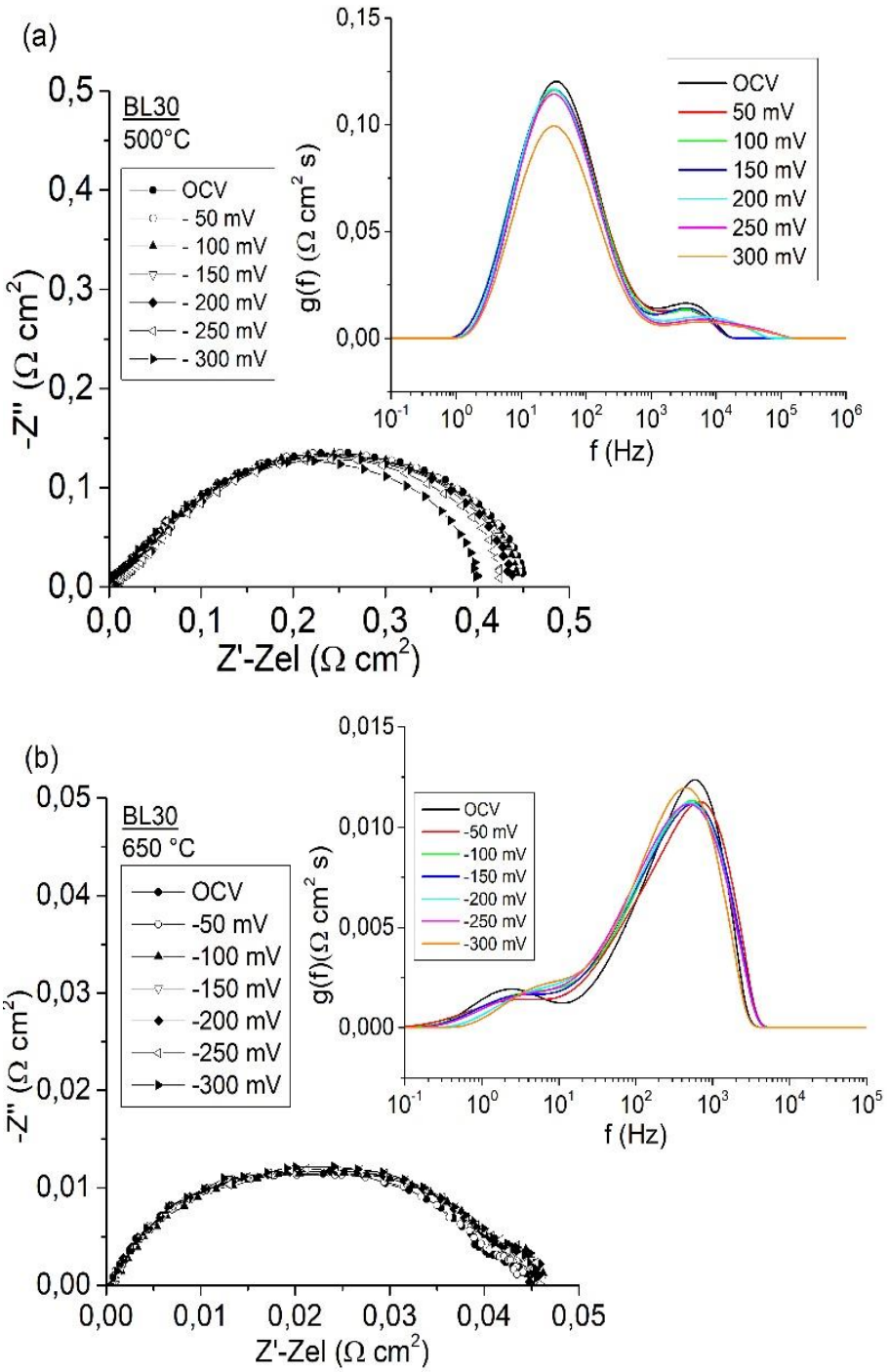

Fig. 4. 6 Impedance spectra and matched distribution of relaxation times at 500 and 600 °C for sample BL30. The mean peak at 500°C appears at 11-12 Hz the mean peak at 650°C appears at about 140 Hz.

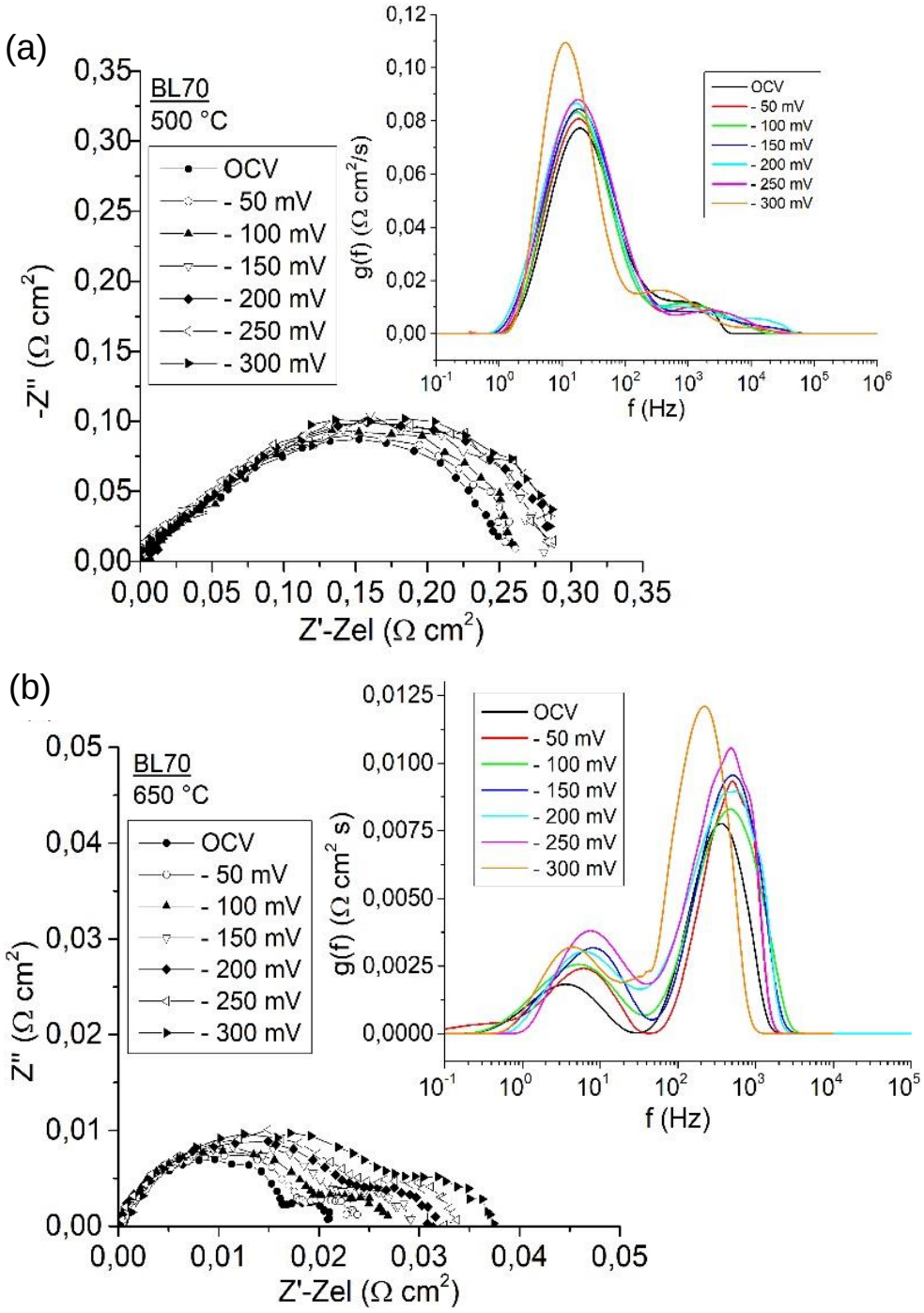

Fig. 4. 7 Impedance spectra and matched distribution of relaxation times at **(a)** 500 and **(b)** 600 °C for sample and for BL70 sample. The mean peak at 500°C appears at 11-12 Hz; the mean peak at 650°C appears at about 140 Hz.

According to Adler model, by manipulating relationship (4.1), it is possible to obtain the imaginary part of impedance from:

$$Z_G'' = \frac{R_{chem}}{\sqrt{2}} \sqrt{\frac{\sqrt{(\omega \cdot t_{chem})^2+1}-1}{(\omega \cdot t_{chem})^2+1}} \quad (4.2)$$

and then extrapolating t_{chem} and R_{chem} fitting experimental data. Their ratio allows to calculate a chemical capacitance:

$$C_{chem} = t_{chem}/R_{chem} \quad (4.3)$$

useful to evaluate the electrode bulk ability to store charge in terms of oxygen vacancies.

For both samples, at 500 °C, R_{chem} is a good approximation of global R_P for all the applied η, confirming the dominant Gerischer behavior introduced above.

More into detail, at 500 °C, BL30 exhibits the same behavior observed by the authors for LSCF reference electrode, with a R_P reduction as η increases. A possible explanation of this behavior, already proposed for LSCF (28), is the increase on oxygen vacancy concentration $[V_O^{\cdot\cdot}]$ under cathodic η and their fundamental contribution to oxygen solid-state diffusion through the electrode bulk. This $[V_O^{\cdot\cdot}]$ variation is highlighted also by C_{chem} response (Fig. 4. 8) that grows under low η. Although BL30 shows a smooth C_{chem} decrease at higher η, its final value globally increases if compared with that calculated in OCV conditions.

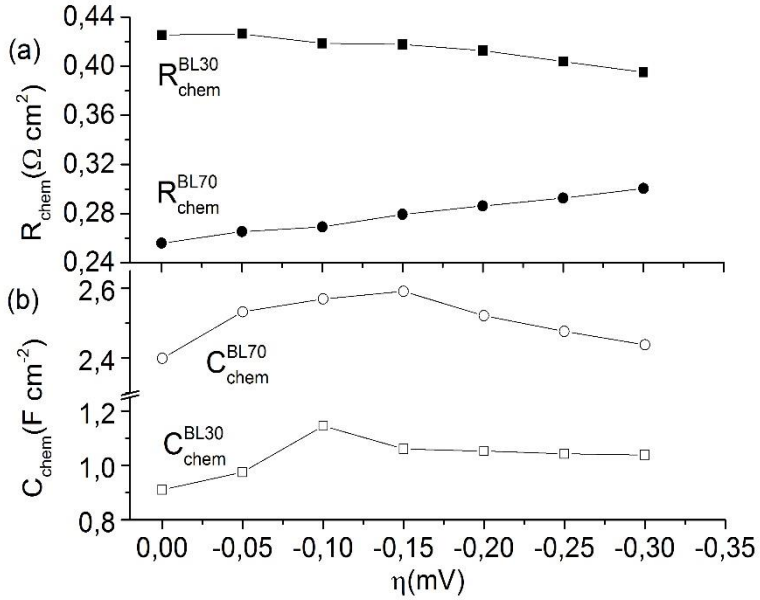

Fig. 4. 8 (a) R_{chem}, and **(b)** C_{chem} as functions of applied overpotential at 500°C, derived from Gerischer fitting, for BL30 and BL70.

For BL70 electrode η has an opposite effect (R_p increases with η), similar to BSCF – behavior investigated by some of the authors in previous paper (28). This work and other papers (34, 52, 53) highlighted that an applied overpotential can cause oxygen vacancy cluster formation as $[V_O^{\cdot\cdot}]$ increases, with consequent losses for oxygen reduction activity of the electrode, explaining why the $C_{chem,}$ starting increase is not able to lead an improvement in electrode activity.

When the system is brought at 650 °C the more resistive process was located at medium-high frequency (Fig. 4. 6 (b) and (d)) pointing out a kinetic change compared to 500 °C behavior. Based on DRT analysis and on a previous study (34), the circuit $R_1(R_{HF}Q_{HF})(R_{LF}Q_{LF})$ was used to fit the impedance results. In this equivalent circuit R_1 is the electrolyte resistance, R_{HF} and Q_{HF} are the resistance and constant phase element (CPE) at high frequency (~ 140 Hz) and R_{LF} and Q_{LF} describe the system at low frequency. According to (54) a capacitance was calculated from CPE parameters. All these parameters are reported in Fig. 4. 9 (a) and (b), which show that the limiting step at 650 °C is the high frequency process (Fig. 4. 6 (b) and Fig. 4. 7 (b)). Also at 650 °C,

according to their high values, the low frequency capacitance is chemical for both samples, confirming the bulk ability to store charge as oxygen vacancies.

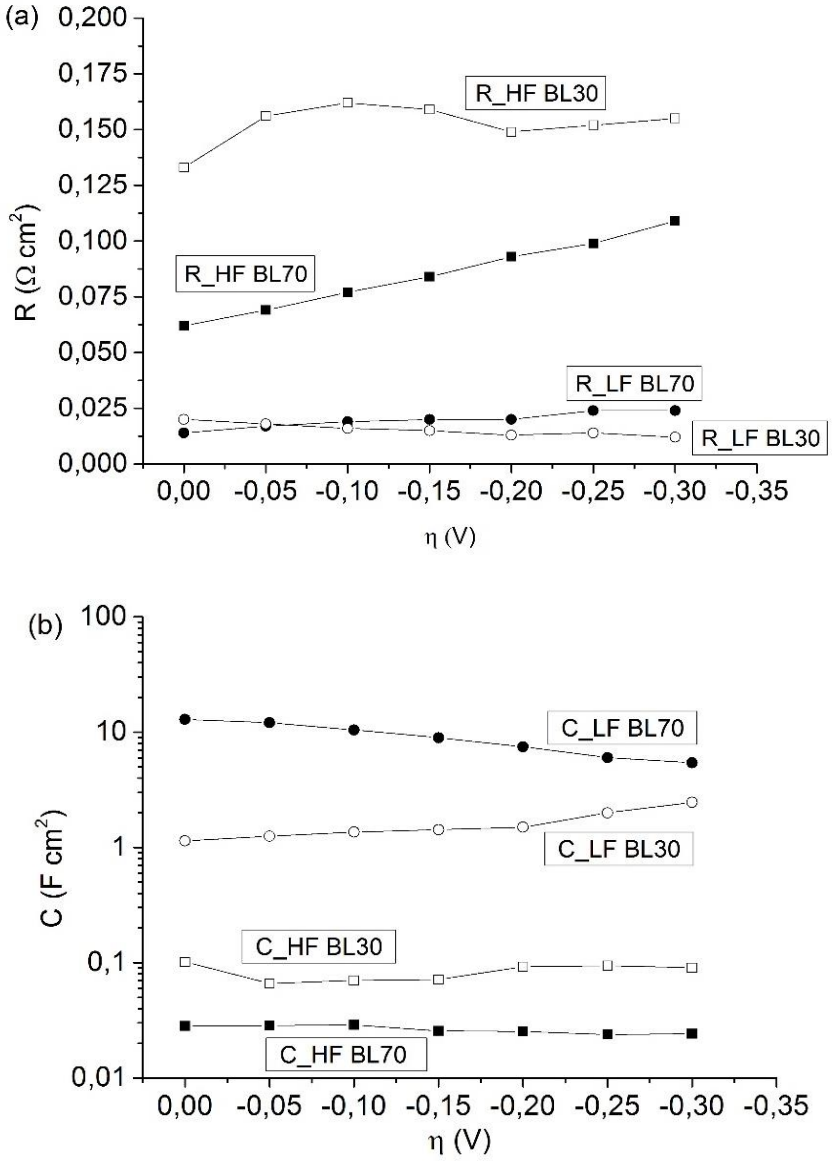

Fig. 4. 9 Values of resistances **(a)** and capacitances **(b)** extracted from the fitting analysis of impedance results obtained at 650°C for BL30 and BL70 samples.

These results showed the potentiality of these electrodes and can represent the base for advanced methods such as ab initio calculation and a theoretical physically-based system modeling, that are beyond the scope of this paper.

After the electrochemical investigation, an ageing test at 650°C under a current load of 200 mA/cm^2 was performed to evaluate electrode degradation over the time (Fig. 4. 10). Degradation of electrode performance in the first operating hours is reported as key factor for cathode materials life. Analysis of performance losses in the first 100-300 working hours has been taken as good indication to evaluate electrode stability for longer operating time (55, 56). Consequently, an ageing time of 200 hours was chosen to monitor the evolution of the system performing periodic EIS measurements at regular time. All the electrodes showed an initial remarkable degradation, but Rp trend are different for the three compositions. BL30 and BL50 showed a quite linear increase of Rp, while for BL70 after the first 50 hours the degradation rate slowed down, remaining the most attractive cathode. The Rp value stabilized close to 0.048 $\Omega\ cm^2$, that is highly competitive even if compared with resistance data of pure and fresh LSCF and BSCF cathode reported in literature (31, 45, 48, 57-63) and also with highly-performing BLSCF. Confirmation about stabilization of BL70 is provided by the decrease of degradation rate; indeed, three different intervals were identified between 0 - 24 h, 24-72 h and above 72 h with a slope of 6.67×10^{-4}, 1.66×10^{-4} and $3.58 \times 10^{-5}\ \Omega\ cm^2\ h^{-1}$ respectively. The starting order of magnitude for degradation rate ($\sim 10^{-4}\ \Omega\ cm^2\ h^{-1}$) is in accordance with those extrapolated for BSCF and LSCF ($10^{-3} \div 10^{-4}\ \Omega\ cm^2\ h^{-1}$) by the authors and other papers (24, 34, 55), while the drop to $\sim 10^{-5}\ \Omega\ cm^2\ h^{-1}$ ($R^2 = 0.992$) represents a stability improvement for electrode systems based on perovskite materials.

XRD and SEM investigations did not show structural and morphological modifications during ageing of BL30 and BL50 samples. It is known (64) that, at SOFC operative temperature, segregation of Sr and Co is likely to take place in LSCF. Therefore, the formation of tiny layers of Sr oxides with limited conductivity can be expected at grain boundaries on aging, but cannot be detected due to the resolution of standard SEM and XRD used in this work as reported in the structural analysis section. The increase of Rp (Fig. 4. 10) with aging time in BL30 and BL50 can be ascribed to

this phenomenon, which is more pronounced in BL30, i.e. the mixture with highest LSCF content.

On the other hand, the observed backward shift of cubic phase XRD peaks during BL70 ageing, explained as progressive incorporation of La compensated by a decrease of oxygen vacancies, find confirmation on the measure of the amount of oxygen vacancies through $C_{Chem.}$ Its trend shows a decrease from 10 to 1 F cm^{-2} in the first 50 hours followed by a stable value in the remaining hours. Such changes in the bulk of the electrode match well with the BL70 performance losses displayed in the first 50 hours of ageing of Fig. 4. 10 and the morphology evolution observed by SEM analysis.

As a matter of fact, BL30 and BL50 C_{Chem} remain unchanged during ageing, indicating a substantial constant concentration of oxygen vacancies.

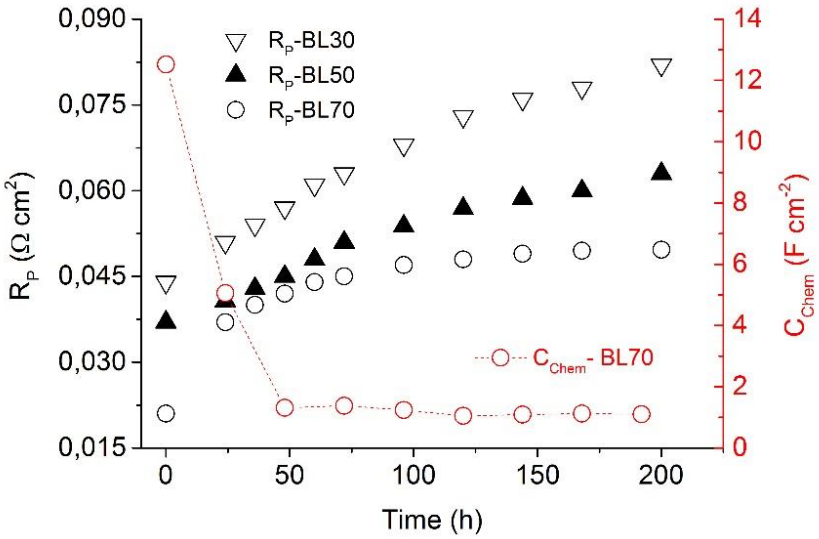

Fig. 4. 10 Degradation rate for BL30, BL50, BL70 electrodes and BL70 chemical capacitance evolution under an applied current load of 200 mA/cm^2 at 650 °C.

4.4 Summary

The effect of composition in performance and stability of $La_{0.6}Sr_{0.4}Co_{0.2}Fe_{0.8}O_{3-\delta}$ (LSCF) - $Ba_{0.5}Sr_{0.5}Co_{0.8}Fe_{0.2}O_{3-\delta}$ (BSCF) based cathodes was investigated. The mixtures were prepared through ball milling of commercial LSCF and BSCF powders. The cathodes were deposited on $Ce_{0.8}Sm_{0.2}O_{2-\delta}$-electrolytes and investigated in SOFC typical conditions of operation (different temperatures and cathodic overpotentials). Microstructural investigation revealed cations interdiffusion between the cubic BSCF and trigonal LSCF structures during sintering, without formation of secondary phases. For BL70, the cubic structure was predominant and showed lattice parameter increase on ageing, compatible with oxygen uptake from atmosphere.

Analyses of the impedance results by distribution of relaxation time (DRT) and equivalent circuits showed two kinetic regimes governing the electrocatalytic activity. At low temperature (500°C), the more resistive step was identified at low frequencies and global impedance was fitted through a Gerischer element, pointing out a behavior co-controlled by surface oxygen exchange and bulk diffusion; this model was no longer suitable for the high temperature regime (650°C).

The resistance trends for BL30 and BL70 as functions of overpotential appeared different: an increase of η led to a R_{chem} decrease for BL30 (LSCF-like behaviour) and to an increase for BL70 sample (BSCF-like behaviour). Like BSCF, also BL70 electrochemical activity decreased under applied overpotential, because of a suppression of vacancy concentration, and this behaviour was not mitigated by the presence of a significant (30 %) starting amount of LSCF.

All cathodes showed very good electrochemical performance. A preliminary ageing test (200 hours) was carried out at 650 °C; despite the observed degradation for all three investigated cathodes, BL70 R_p showed an almost asymptotic trend, displaying, for the ageing studied time, a final stabilized and low value close to 0.048 Ω cm^2. These first results open the way for a further optimization step to modulate physical and chemical electrode properties, with a more detailed experimental approach based on application of strategies already available to improve electrode stability and activity.

Nevertheless, investigations at longer loading time are necessary and planned for the near future, especially for BL70 composition.

4.5 References

1. S. B. Adler, *Chem. Rev.*, **104**, 4791 (2004).
2. J. Areum, K. Junyoung, S. Jeeyoung and K. Guntae, *ChemElectroChem*, **3**, 511 (2016).
3. M. P. Carpanese, A. Barbucci, G. Canu and M. Viviani, *Solid State Ionics*, **269**, 80 (2015).
4. F. S. da Silva and T. M. de Souza, *Int. J. Hydrog. Energy*, **42**, 26020 (2017).
5. Y. Dai, Z. Lou, Z. Wang, J. Qiao, W. Sun and K. Sun, *Int. J. Hydrog. Energy*, **40**, 5939 (2015).
6. X. Huang, J. Feng, H. R. S. Abdellatif, J. Zou, G. Zhang and C. Ni, *Int. J. Hydrog. Energy*, **43**, 8962 (2018).
7. C. Nicollet, A. Flura, V. Vibhu, A. Rougier, J.-M. Bassat and J.-C. Grenier, *Int. J. Hydrog. Energy*, **41**, 15538 (2016).
8. N. Ortiz-Vitoriano, C. Bernuy-López, A. Hauch, I. Ruiz de Larramendi and T. Rojo, *Int. J. Hydrog. Energy*, **39**, 6675 (2014).
9. S. J. Skinner, *Int. J. Inorg. Mater.*, **3**, 113 (2001).
10. M. Viviani, G. Canu, M. P. Carpanese, A. Barbucci, A. Sanson, E. Mercadelli, C. Nicolella, D. Vladikova, Z. Stoynov, A. Chesnaud, A. Thorel, Z. Ilhan and S.-A. Ansar, *Energy Procedia*, **28**, 182 (2012).
11. D. Vladikova, Z. Stoynov, A. Chesnaud, A. Thorel, M. Viviani, A. Barbucci, G. Raikova, P. Carpanese, M. Krapchanska and E. Mladenova, *Int. J. Hydrog. Energy*, **39**, 21561 (2014).
12. A. Mineshige, J. Izutsu, M. Nakamura, K. Nigaki, J. Abe, M. Kobune, S. Fujii and T. Yazawa, *Solid State Ionics*, **176**, 1145 (2005).
13. M. Z. Khan, M. T. Mehran, R.-H. Song, J.-W. Lee, S.-B. Lee, T.-H. Lim and S.-J. Park, *Ceram. Int.*, **42**, 6978 (2016).
14. M. Z. Khan, M. T. Mehran, R.-H. Song, S.-B. Lee and T.-H. Lim, *Int. J. Hydrog. Energy*, **43**, 12346 (2018).

15. R. Kiebach, W.-W. Zhang, W. Zhang, M. Chen, K. Norrman, H.-J. Wang, J. R. Bowen, R. Barfod and P. V. Hendriksen, *J. Power Sources*, **283**, 151 (2015).
16. F. Wang, M. E. Brito, K. Yamaji, D.-H. Cho, M. Nishi, H. Kishimoto, T. Horita and H. Yokokawa, *Solid State Ionics*, **262**, 454 (2014).
17. F. Wang, M. Nishi, M. E. Brito, H. Kishimoto, K. Yamaji, H. Yokokawa and T. Horita, *J. Power Sources*, **258**, 281 (2014).
18. H. Wang, K. J. Yakal-Kremski, T. Yeh, G. M. Rupp, A. Limbeck, J. Fleig and S. A. Barnett, *J. Electrochem. Soc.*, **163**, F581 (2016).
19. W. Araki, Y. Arai and J. Malzbender, *Mater. Lett.*, **132**, 295 (2014).
20. Z. Shao and S. M. Haile, *Nature*, **431**, 170 (2004).
21. D. N. Mueller, R. A. De Souza, T. E. Weirich, D. Roehrens, J. Mayer and M. Martin, *Phys. Chem. Chem. Phys.*, **12**, 10320 (2010).
22. Z. Yáng, J. Martynczuk, K. Efimov, A. S. Harvey, A. Infortuna, P. Kocher and L. J. Gauckler, *Chem. Mater.*, **23**, 3169 (2011).
23. J. M. Bermudez, J. Garcia-Fayos, T. R. Reina, G. Reed, E. S. Persoon, D. Görtz, M. Schroeder, M. Millan and J. M. Serra, *J. Membr. Sci.*, **562**, 26 (2018).
24. M. Arnold, H. Wang and A. Feldhoff, *J. Membr. Sci.*, **293**, 44 (2007).
25. Y. Zhang, G. Yang, G. Chen, R. Ran, W. Zhou and Z. Shao, *ACS Appl. Mater. Interfaces*, **8**, 3003 (2016).
26. N. Ai, K. Chen and S. P. Jiang, *Int. J. Hydrog. Energy*, **42**, 7246 (2017).
27. J. Chen, D. Wan, X. Sun, B. Li and M. Lu, *Int. J. Hydrog. Energy*, **43**, 9770 (2018).
28. A. Giuliano, M. P. Carpanese, D. Clematis, M. Boaro, A. Pappacena, F. Deganello, L. F. Liotta and A. Barbucci, *J. Electrochem. Soc.*, **164**, F3114 (2017).
29. E. N. Naumovich, K. Zakharchuk, S. Obrębowski and A. Yaremchenko, *Int. J. Hydrog. Energy*, **42**, 29443 (2017).
30. F. Zhou, Y. Liu, X. Zhao, W. Tang, S. Yang, S. Zhong and M. Wei, *Int. J. Hydrog. Energy*, **43**, 18946 (2018).
31. X. Zhang, W. Zhang, L. Zhang, J. Meng, F. Meng, X. Liu and J. Meng, *Electrochim. Acta*, **258**, 1096 (2017).
32. Y. Liu, J. Bi, B. Chi, J. Pu and L. Jian, *Int. J. Hydrog. Energy*, **41**, 6486 (2016).

33. E. Perry Murray, M. J. Sever and S. A. Barnett, *Solid State Ionics*, **148**, 27 (2002).
34. A. Giuliano, M. P. Carpanese, M. Panizza, G. Cerisola, D. Clematis and A. Barbucci, *Electrochim. Acta*, **240**, 258 (2017).
35. M. Mosiałek, A. Kędra, M. Krzan, E. Bielańska and M. Tatko, *Arch. Metall. Mater.*, **61** (2016).
36. J.-S. Kim, D.-H. Yeon, D. W. Jung and C. Kwak, *J. Power Sources*, **249**, 66 (2014).
37. M. Cimenti, A. C. Co, V. I. Birss and J. M. Hill, *Fuel Cells*, **7**, 364 (2007).
38. J. Winkler, P. V. Hendriksen, N. Bonanos and M. Mogensen, *J. Electrochem. Soc.*, **145**, 1184 (1998).
39. M. P. Carpanese, M. Panizza, M. Viviani, E. Mercadelli, A. Sanson and A. Barbucci, *J. Appl. Electrochem.*, **45**, 657 (2015).
40. S. Presto, A. Barbucci, M. P. Carpanese, M. Viviani and R. Marazza, *J. Appl. Electrochem.*, **39**, 2257 (2009).
41. T. H. Wan, M. Saccoccio, C. Chen and F. Ciucci, *Electrochim. Acta*, **184**, 483 (2015).
42. L. Almar, H. Störmer, M. Meffert, J. Szász, F. Wankmüller, D. Gerthsen and E. Ivers-Tiffée, *ACS Appl. Energy Mater.*, **1**, 1316 (2018).
43. J. M. Serra, J. Garcia-Fayos, S. Baumann, F. Schulze-Küppers and W. A. Meulenberg, *J. Membr. Sci.*, **447**, 297 (2013).
44. C. Duan, D. Hook, Y. Chen, J. Tong and R. O'Hayre, *Energ. Environ. Sci.*, **10**, 176 (2017).
45. L. Almar, J. Szász, A. Weber and E. Ivers-Tiffée, *J. Electrochem. Soc.*, **164**, F289 (2017).
46. Y. Zhang, Y. Chen, M. Yan and F. Chen, *J. Power Sources*, **283**, 464 (2015).
47. S. B. Adler, J. A. Lane and B. C. H. Steele, *J. Electrochem. Soc.*, **143**, 3554 (1996).
48. D. Garcés, A. L. Soldati, H. Troiani, A. Montenegro-Hernández, A. Caneiro and L. V. Mogni, *Electrochim. Acta*, **215**, 637 (2016).
49. H.-N. Im, M.-B. Choi, S.-Y. Jeon, B. Singh and S.-J. Song, *Meeting Abstracts*, **MA2014-01**, 729 (2014).
50. R. Amin and K. Karan, *J. Electrochem. Soc.*, **157**, B285 (2010).

51. F. Bidrawn, R. Küngas, J. M. Vohs and R. J. Gorte, *J. Electrochem. Soc.*, **158**, B514 (2011).
52. S. Gangopadhyay, A. E. Masunov, T. Inerbaev, J. Mesit, R. K. Guha, A. K. Sleiti and J. S. Kapat, *Solid State Ionics*, **181**, 1067 (2010).
53. E. V. Tsipis, E. N. Naumovich, M. V. Patrakeev, A. A. Yaremchenko, I. P. Marozau, A. V. Kovalevsky, J. C. Waerenborgh and V. V. Kharton, *Solid State Ionics*, **192**, 42 (2011).
54. B. Hirschorn, M. E. Orazem, B. Tribollet, V. Vivier, I. Frateur and M. Musiani, *Electrochim. Acta*, **55**, 6218 (2010).
55. C. Endler, A. Leonide, A. Weber, F. Tietz and E. Ivers-Tiffée, *ECS Trans.*, **25**, 2381 (2009).
56. W. G. Wang and M. Mogensen, *Solid State Ionics*, **176**, 457 (2005).
57. C.-H. Chen, C.-L. Chang and B.-H. Hwang, *Mater. Chem. Phys.*, **115**, 478 (2009).
58. Y. Chen, B. Qian, S. Li, Y. Jiao, M. O. Tade and Z. Shao, *J. Membr. Sci.*, **449**, 86 (2014).
59. F. Deganello, L. F. Liotta, G. Marcì, E. Fabbri and E. Traversa, *Mater. Renew. and Sustain. Energy*, **2**, 8 (2013).
60. C. Su, X. Xu, Y. Chen, Y. Liu, M. O. Tadé and Z. Shao, *J. Power Sources*, **274**, 1024 (2015).
61. H. Sumi, T. Ohshiro, M. Nakayama, T. Suzuki and Y. Fujishiro, *Electrochim. Acta*, **184**, 403 (2015).
62. K. Wang, R. Ran, W. Zhou, H. Gu, Z. Shao and J. Ahn, *J. Power Sources*, **179**, 60 (2008).
63. X. Zhu, H. Xia, Y. Li and Z. Lü, *Mater. Lett.*, **161**, 549 (2015).
64. J. S. Hardy, C. A. Coyle, J. F. Bonnett, J. W. Templeton, N. L. Canfield, D. J. Edwards, S. M. Mahserejian, L. Ge, B. J. Ingram and J. W. Stevenson, *J. Mater. Chem. A*, **6**, 1787 (2018).

CHAPTER 5

LSF meets LBC: what happens?

HIGHLIGHTS

- *$La_{0.6}Sr_{0.4}FeO_3$ (LSF64) and $La_{0.6}Ba_{0.4}CoO_3$ (LBC64) were mixed to study interaction in different conditions.*
- *LSF64 and LBC64 react during sintering stage forming $Ba_{0.099}Sr_{0.297}La_{0.594}Fe_{0.8}Co_{0.2}O_3$, a new perovskite phase (NPP).*
- *NPP material was electrochemically tested as cathode for IT-SOFC by means Pulse Laser Deposition (PLD) thin film electrode.*
- *NPP shows a lower polarization resistance than reference materials, due to its higher content of oxygen vacancy concentration.*
- *Bilayer systems were investigated: a LBC top-layer over a LSF cathode improve electrocatalytic activity.*

5.1 Introduction

Because Solid oxide fuel cells (SOFCs) are taken hold on the market, they need to satisfy two fundamental requirements, i) high power density and ii) durability. One of the main bottleneck, which limits the usage of these devices, is the cathode side, where the oxygen reduction reaction takes place. Cathode material must have a high electrocatalytic activity for the oxygen reaction and at the same time high thermal stability. This means not only achieve a good resistance to the stressfully operating condition (high temperature), but also a good matching (chemical, thermal and mechanical) with other cell components.

Materials proposed until today suffer of stability problems or do not combine in a sufficient way the features presented above. A possible solution is the formation of a composite cathode, which is made combining different materials. In the past studies almost all the composite cathode mixed the electrode material with electrolyte particle with the main aim to improve the ionic conductivity and accommodate mismatches with the dense electrolyte.

Starting from these preliminary consideration, and based on results presented in the previous chapters the attention has been focused on two materials: $La_{0.6}Sr_{0.4}FeO_3$ (LSF64) and $La_{0.6}Ba_{0.4}CoO_3$ (LBC64). Both show an ABO_3 perovskite structure, widely investigated as cathode for SOFC (1-10).

In this case, the idea of composite electrode is developed around a fulcrum point: combine two cathode materials to exploit their different and complementary strengths under several point of view, namely, oxygen surface exchange capability, charge transport and thermal stability.

In fact, LSF64 shows a good chemical stability and a thermal expansion compatibility with the most of electrolytes (1, 2). Nevertheless, its electrochemical activity, in the temperature range of our interest (500-650°C), is too low considering the research target.

On the other hand, the few studies focused on LBC64 have highlighted an extraordinary activity toward oxygen reduction reaction, especially due to its very high

oxygen surface exchange ability (9). For this material the main problem rises from a remarkable mismatch with electrolyte thermal expansion coefficient.

For these reasons, looking for a mutual aid, here the interaction between the two materials are investigated.

To the best of author knowledge, no works about LSF-LBC mixture based cathode are reported in literature.

5.2 Sample preparation

Samples described in this session, differently from those described in the previous chapters, are constituted by thin film electrodes in the order of nm (in this specific case no thicker than 200 nm). Also the sample configuration has peculiar features. In fact the conventional porous electrode is used to evaluate material performance in a cell configuration close to those of commercial applications. Thin film technology can be fruitful exploited to investigate processes involved in the electrode kinetic with more detail. This advantage is due to the simplified geometry of the thin electrode that allow to neglect some phenomena like gas transport and diffusion present in conventional porous and thick electrode. Where present, the porosity of thin film is more regular thanks to the deposition technique used (Pulse Laser Deposition, PLD).

Based on these points cell configurations with thin film electrodes have been prepared to evaluate the electrochemical performance of composite electrodes obtained by mixing and/or coupling for the first time LSF64 and LBC64.

The system used for all the electrochemical test is sketched in Fig. 5. 1. It consists of a 5 x 5 mm supporting electrolyte, (100) oriented Yttria – stabilized Zirconia (YSZ 9.5 mol% Y_2O_3), width 0.5 mm, a buried Pt grid as current collector and an active thin-layer (electrode). The position of embedded Pt grid has been chosen after preliminary tests, which allow to evaluate the best current collector position and in accordance with literature (11-13).

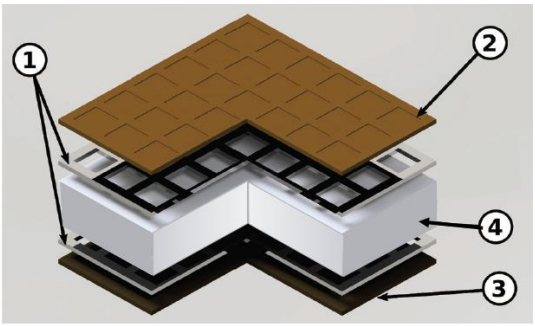

Fig. 5. 1 Sketch of cell configuration **(1)** Platinum current collector **(2)** Working electrode **(3)** counter electrode **(4)** YSZ electrolyte. Adapted from (5)

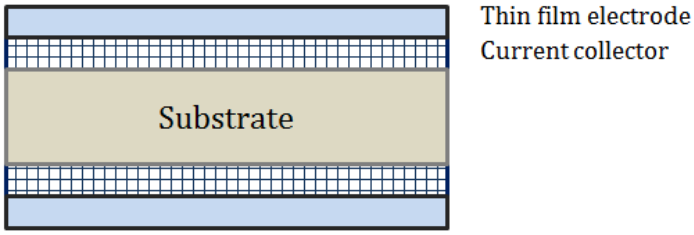

Fig. 5. 2 Front view of cell configuration used

5.2.1 Target preparation

$La_{0.6}Sr_{0.4}FeO_3$ (Sigma Aldrich) and $La_{0.6}Ba_{0.4}CoO_3$ (LBC64 by Pechini's method (14) were used in the cell preparation. In LBC64 synthesis Lanthanum oxide (La_2O_3), strontium carbonate ($SrCO_3$), barium carbonate ($BaCO_3$) and cobalt powders (all Sigma Aldrich, 99.995%) were individually dissolved in nitric acid, mixed in appropriate ratios and finally citric acid (TraceSELECT, 99.9998%) was added for chelation. A calcination step was performed at 1000 °C to obtain the desired phase as confirm by X-ray diffraction analysis presented here in **Fig. 5. 3**.

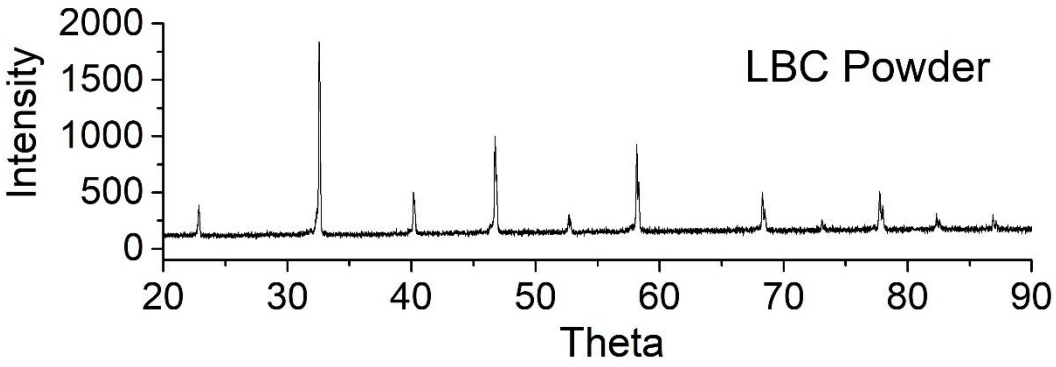

Fig. 5. 3 X-ray diffraction pattern for LBC64 powder.

To investigate the interaction between LSF64 and LBC64 in different condition, several PLD targets were prepared:

1. pure LSF64,
2. pure LBC64,
3. a mixture of LSF64 and LBC64 powders in a molar ratio 50:50 %,
4. a “Fake” mixed target prepared as illustrated in Fig.

All the pellets were obtained through an isostatical pressing at 150 MPa followed by a sintering stage at 1200 °C for 12 hours. These three types of targets are made by a unique disk as reported in Fig. 5. 4 (left-side), which is the classical target configuration for PLD target.

The last target prepared, called “new PLD target” and illustrated in Fig. 5. 4 (right-side), is made by half LSF64 and half LBC64 pellet. Then, the peculiar characteristic of this new target is that the two materials are physically separate and come into contact for the first time inside PLD chamber during film deposition.

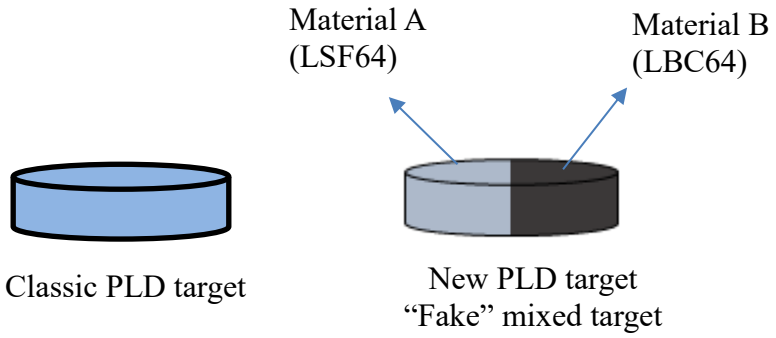

Fig. 5. 4 Scheme of target used in PLD process

5.2.2 Current collector preparation

Pt current collector was deposited by means of photolithography and sputtering process. Negative photolithography was used to create the desired pattern for current collector, as reported in Fig. 5. 5 describing the main phases of the process.

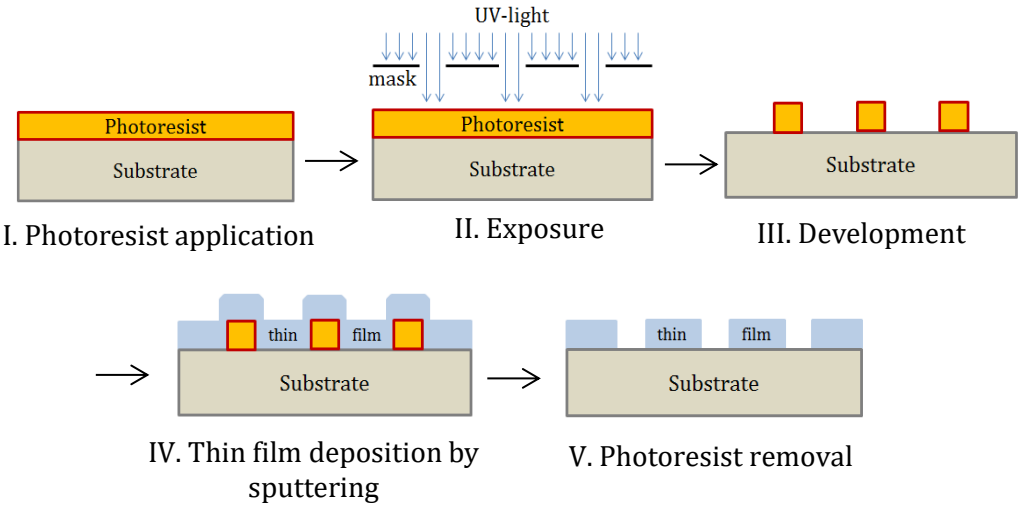

Fig. 5. 5 Sketch of Pt grid current collector preparation by mean of photolithography and sputtering processes.

Current collector deposition can be subdivided in five steps:

i. photoresist layer was deposited on electrolyte surface by spin coating process;
ii. photoresist layer is covered by a mask with the desired pattern and irradiated by UV-light;
iii. a development step allows to remove the non-irradiated photoresist;
iv. platinum layer (100 nm) is deposited on a 5 nm Titanium layer, which aids the adhesion with the electrolyte;
v. remaining photoresist is removed with ethanol forming the desired pattern.

Table 5.1 and Table 5. 2 summarized all the photolithography and sputtering operating conditions, respectively.

Photolithography	
Photoresist	100 µl
Spincoater speed	100 rpm
Heating	2 – 3 min at 100 °C
Developing time	60
Exposure time	60 – 90 s

Table 5. 1 Photolithography parameters

Sputtering		
	Titanium (5 nm)	Platinum (100 nm)
Sputter time	27 s	125 s
Argon pressure	7 x 10^{-3} mbar	2 x 10^{-2} mbar
Sputter current	100 mA	100 mA
Target distance	6 cm	6 cm

Table 5. 2 Sputtering parameters

In Fig. 5. 6 a current collector grid is reported in a planar view; it is characterized by a width of 5 µm spaced for 30 µm.

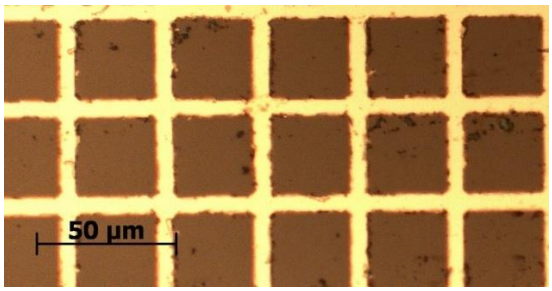

Fig. 5. 6 Top view of Platinum current collector grid on YSZ substrate

5.2.3 Thin layer deposition

Thin layers of active material were deposited using Pulse Laser Deposition technique. PLD process was conducted at oxygen partial pressure of $4*10^{-2}$ mbar, and before the deposition, target was ablated for 2 minutes by a KrF-excimer laser (Compex Pro 201 F) with 248 nm wavelength, and an energy per pulse of 400 mJ (Table 5. 3). The substrate was heated at 650 °C to obtain a dense thin layer, at 450 °C for a porous electrode structure. The desired layer thickness was 100 nm for the porous electrode, and 200 nm for the dense and bilayer system.

Pulse Laser Deposition

Oxygen partial pressure	4×10^{-2} mbar
Laser energy	400 mJ
Laser frequency	5 Hz
Substrate temperature	450 – 650 °C
Substrate – target distance	6 cm
Cooling rate	15 °C/min

Table 5. 3 Pulse Laser Deposition parameters

5.3 Porous system characterization

Before to start to present the results about porous electrode, it could be useful, define a nomenclature for different sample, to make reading more fluent. The reference samples are called with the own material (LSF64, LBC64), while we refer to the new perovskite phase with the acronym NPP.

Microstructural and electrochemical characterization are divided in two subsections, to compare samples with a similar morphological structure (porous or dense). Section (5.3), considers three porous samples made by a thin porous layer (100 nm) of a pure LSF, pure LBC, and new perovskite phase (NPP) $Ba_{0.099}Sr_{0.297}La_{0.594}Fe_{0.8}Co_{0.2}O_3$, respectively. Section (5.4) summarizes the effects of the

addition of a thin LBC top layer on a thin-dense LSF electrode, evaluating temperature and oxygen partial pressure dependence in terms of activation energy, polarization resistance and capacitance.

5.3.1 Microstructural characterization

Target materials and deposited electrodes were analyzed in Bragg Brentano geometry by a X'Pert Powder (PANalytical) diffractometer.

Fig. 5. 7 reports all the patterns for targets before and after sintering stage measured in 2θ range. Fig. 5. 7 (b) shows the pattern for the LBC target prepared by Pechini's method.

After sintering step, the two reference pellets maintain the same structure and no changes have been detected. On the other hands for mixture target, the two starting phases (LSF64 and LBC64) were no longer detected after sintering as reported in Fig. 5. 7 (c). XRD pattern analysis showed a strong modification, and a new phase has been detected as $Ba_{0.099}Sr_{0.297}La_{0.594}Fe_{0.8}Co_{0.2}O_{3.}$ The new phase has been characterized by a perovskite structure.

To investigate the interactions of LSF64 with LBC64 in different conditions than those characteristic of sintering process, a pellet made half by LSF64 target and half by LBC64 target has been prepared as sketch in Fig. 5. 4 ("Fake" mixed target right-side). In this configuration, LSF64 and LBC64 come into contact for the first time during PLD process. As remarked in Table 5. 3, in PLD chamber, temperature and oxygen partial pressure are extremely far from values used for a common sintering phase. Two materials could start to interact within the plume or at electrolyte surface, after deposition. XRD analysis in Fig. 5. 8 reports the pattern of a thin film on YSZ substrate after 1 hour of deposition process.

In addition to YSZ peaks, the same new perovskite phase ($Ba_{0.099}Sr_{0.297}La_{0.594}Fe_{0.8}Co_{0.2}O_3$), introduced above, was recognized. This means that LSF64 and LBC64 have a strong interaction also in PLD operating conditions. Then, even the "fake" target is unsuitable to preserve these two materials separate to produce a composite electrode. Furthermore, the cation interdiffusion which occurs between the reference structures, make extremely tricky to control the stoichiometry of deposited

layer; in fact PLD process depends by several parameters, and among them the material rate deposition and the surface area exposed to the beam play a crucial role.

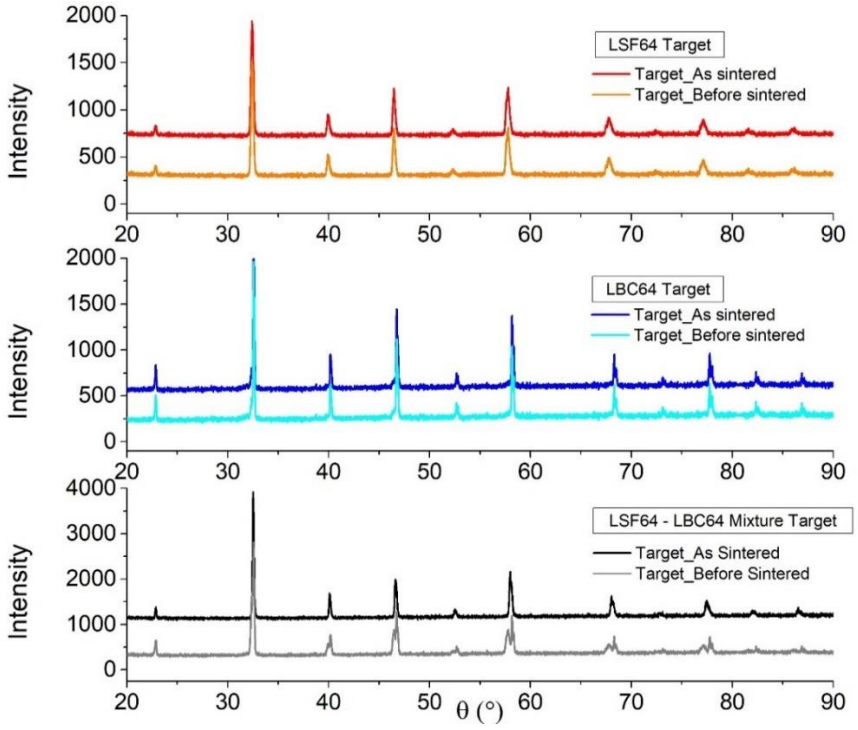

Fig. 5. 7 X-ray diffraction pattern for (a) LSF, (b) LBC64 and (c) LSF64-LBC64 mixture targets before (bottom pattern) and as sintered (up pattern).

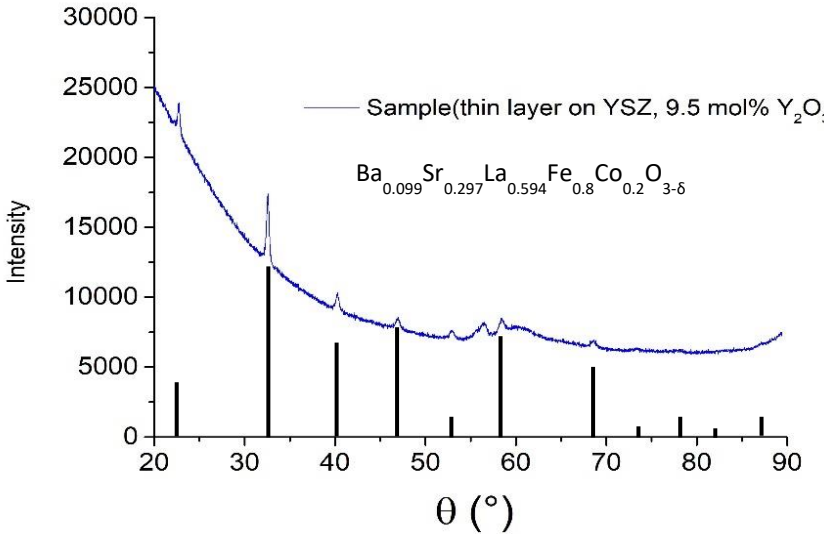

Fig. 5. 8 X-ray diffraction pattern of sample deposited by using “new fake” target.

5.3.2 Electrochemical characterization

Electrochemical Impedance Spectroscopy measurements were carried out using a Novocontrol PotGal electrochemical test station in a frequency range of 1MHz to 10 mHz with a ac voltage of 10 mV.

The first operating parameter taken into account was the temperature in a range between 380 - 600 °C with a temperature step of 20 °C. All impedance measurements were performed in synthetic air. Within the considered temperature range, the NPP electrode showed the lowest polarization resistance as reported in the Fig. 5. 9. At 600 °C, the NPP cathode had a polarization resistance of 0.2 Ω cm^2, against 0.4 Ω cm^2 and 1.05 Ω cm^2 for LBC and LSF electrodes, respectively. The value obtained for NPP electrode is competitive compared with polarization resistance values reported in literature for SOFC cathodes tested in a thin film configuration (15-17).

From Fig. 5. 9 (a) (b) it is clear that LSF64 is characterized by at least two processes in the whole temperature range, one at medium-high frequency and the other at lower frequency. Also NPP seems to follow a similar behavior that at higher temperature appears more depressed at high frequency. As regards LBC64 electrode, two separated phenomena are well evident at 400 °C (see inset Fig. 5. 9 a), while at 600 °C (Fig. 5. 9 b) is not so trivial, observing impedance spectra. A more detail discussion about possible physical phenomena involved is presented below by means distribution of relaxation time and equivalent circuit analysis.

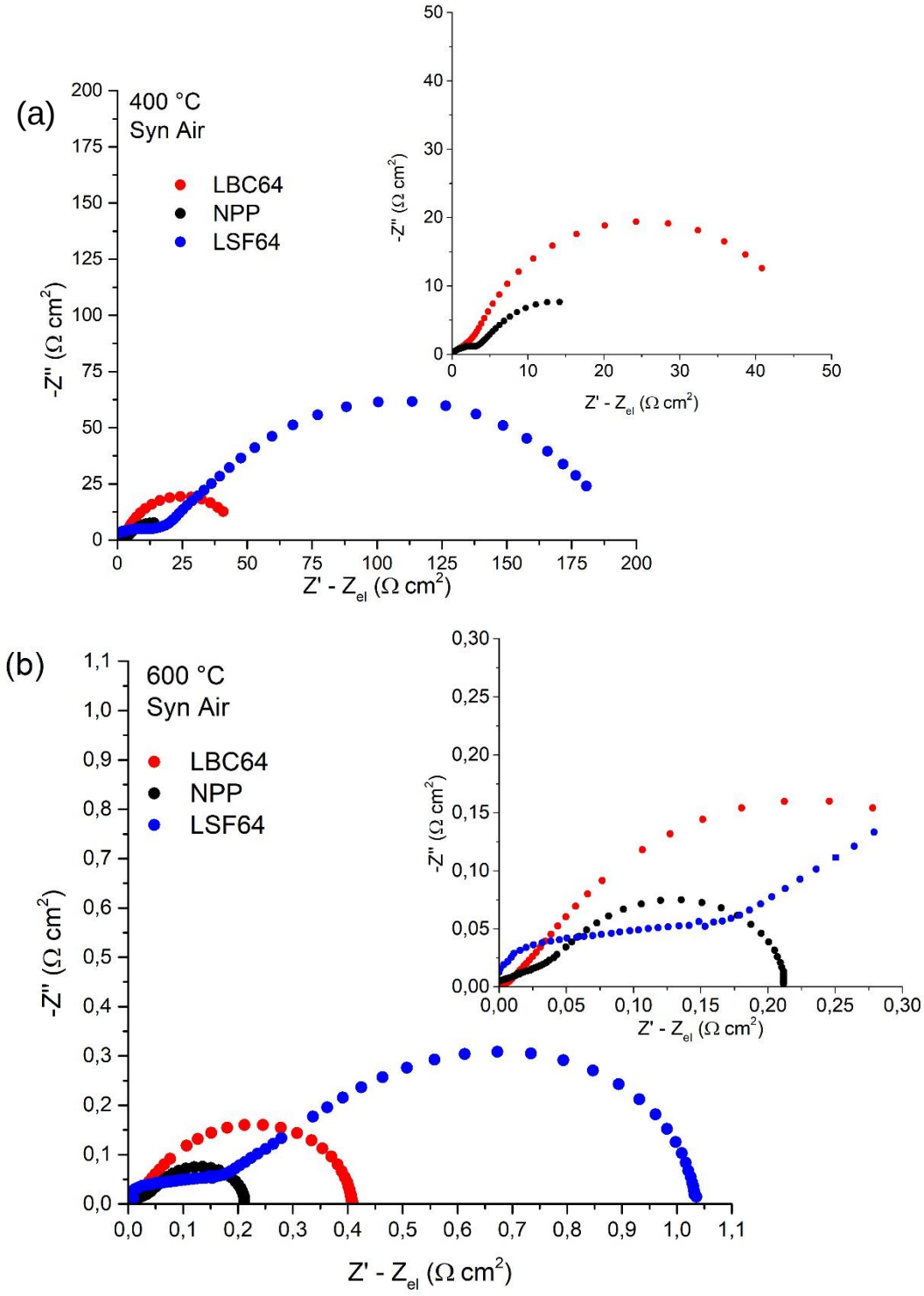

Fig. 5. 9 Electrochemical impedance spectroscopy at **(a)** 400 °C and **(b)** 600 °C for LSF, LBC and NPP thin film electrodes on YSZ substrates.

A global apparent activation energy was calculated. In Fig. 5. 10 is reported the Arrhenius plot for the three samples during the heating. LBC64 and NPP have a similar activation energy, while LSF64 has a higher value. Also the activation energy here presented are in agreement with activation energy of mixed ionic and electronic conductor with a perovskite structure, reported in literature (9, 18-24). After these preliminary, but promising, results about NPP material, the new electrode has been deeper electrochemically investigated and compared with reference materials.

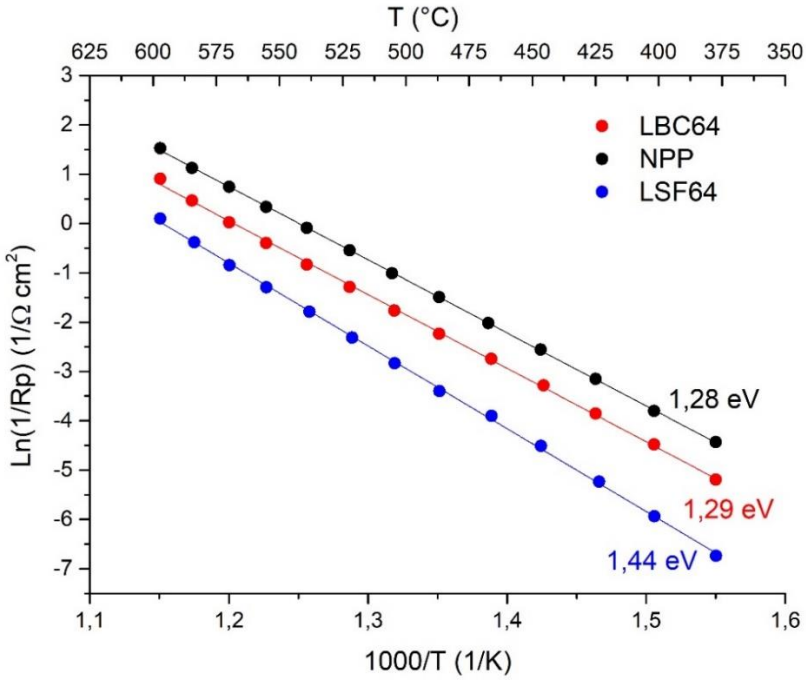

Fig. 5. 10 Polarization resistance as a function of temperature for LBC64 (red points), LSF64 (blue points) and NPP (black points) thin porous electrodes, and corresponding activation energies.

- *Distribution of relaxation time analysis*

To identify the number of phenomena involved, analysis of distribution of relaxation time (DRT) was performed using a user-made code, based on well-known Tikhonov regularization and described in Chapter 2. This kind of analysis allows to evaluate how many processes occur in the whole frequency range considered, without make any physical assumption about the system.

From Fig. 5. 11 (a) and (b) is evident that the most resistive process is located at low frequency (between 0.01 and 30 Hz) for all the electrodes. Moving at higher frequency (f > 30 Hz) DRT does not show a unique trend and a possible behavior explanation requires a deeper analysis as reported below. Nevertheless, these DRT curves can provide some preliminary information. Indeed, these graphs highlight a thermal activation of the main process when temperature grow up: area under the curves drastically decreases but also the peak frequency move to the right-side at higher values suggesting a faster process.

Fig. 5. 12 shows the DRT spectra for the LBC64 cathode at 600°C in synthetic air, that it will be taken as example in this first part of the discussion.

From the DRT curve two processes (P1, P2) are well recognizable, with peaks at 12.58 Hz (P1) and 398 Hz (P2), respectively. A third small peak has been identified at higher frequency (10^5 Hz); its intensity is remarkably lower than others two and the first used approach neglected it as an independent phenomena. Moreover, its frequency position is quite high to be considered as part of electrode process.

DRT curve also allows to extrapolate the global polarization resistance (R_P) for the electrode process, as the area under the curve, and the obtained value (0.406 Ω cm^2) is really close to experimental value (0.404 Ω cm^2), with an error of 0.5%.

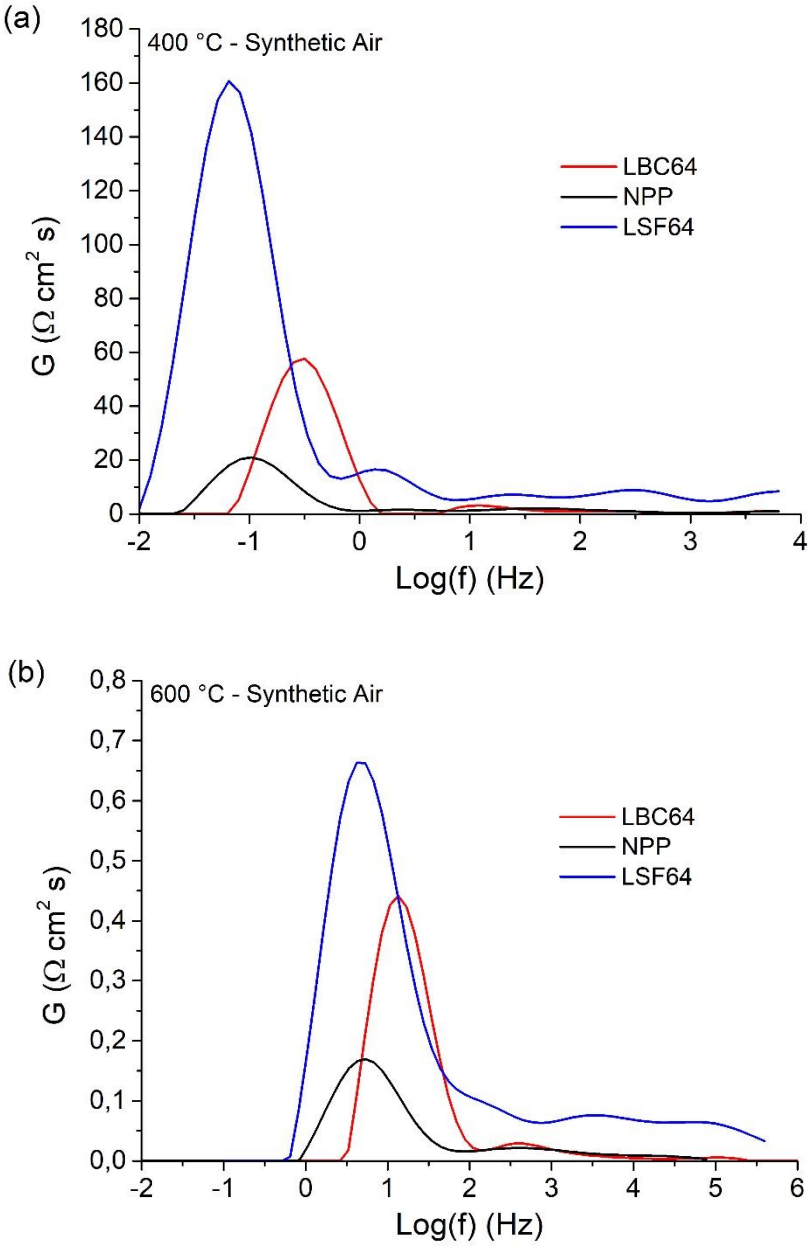

Fig. 5. 11 Distribution of relaxation times analysis for LBC64 (red line), LSF64 (blue line) and NPP (black line) at **(a)** 400 °C and **(b)** 600 °C.

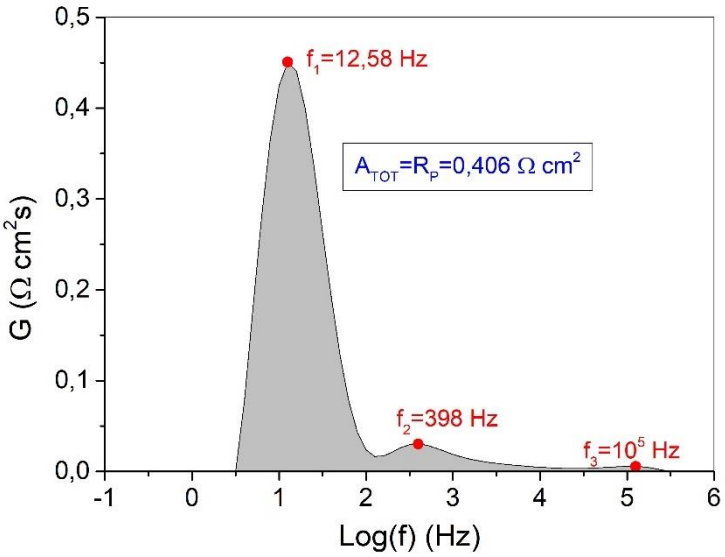

Fig. 5. 12 DRT curve for porous LBC64 sample at 600 °C and OCV condition, to evaluate polarization resistance and frequency peaks.

Based on the hypothesis that the electrode kinetic is described by two processes, a first evaluation of their resistance was performed calculating the area under the curve. The local minimum at 125 Hz was considered as separation point between the two processes. Therefore the left-side part of the curve (Fig. 5. 13 a) is ascribed to a low frequency process (P1) while the right-side (Fig. 5. 13 b) was considered as medium frequency phenomena (P2). A_1 and A_2 are the area used to evaluate resistance associated to P1 and P2, respectively. It is well evident that P1 is more resistive and with a value equal to 0.36987 Ω cm^2 represents 91% of the total resistance. As regards P2, its resistance was extrapolated including also the third peak at 10^5 Hz as anticipated before. Under this assumptions, R_2 is 0.03657 Ω cm^2 with an absolute variation of 0.0044 Ω cm^2 if compared with the value obtained limiting the resistance calculation at local minimum at 25120 Hz (f_{A2_Min}).

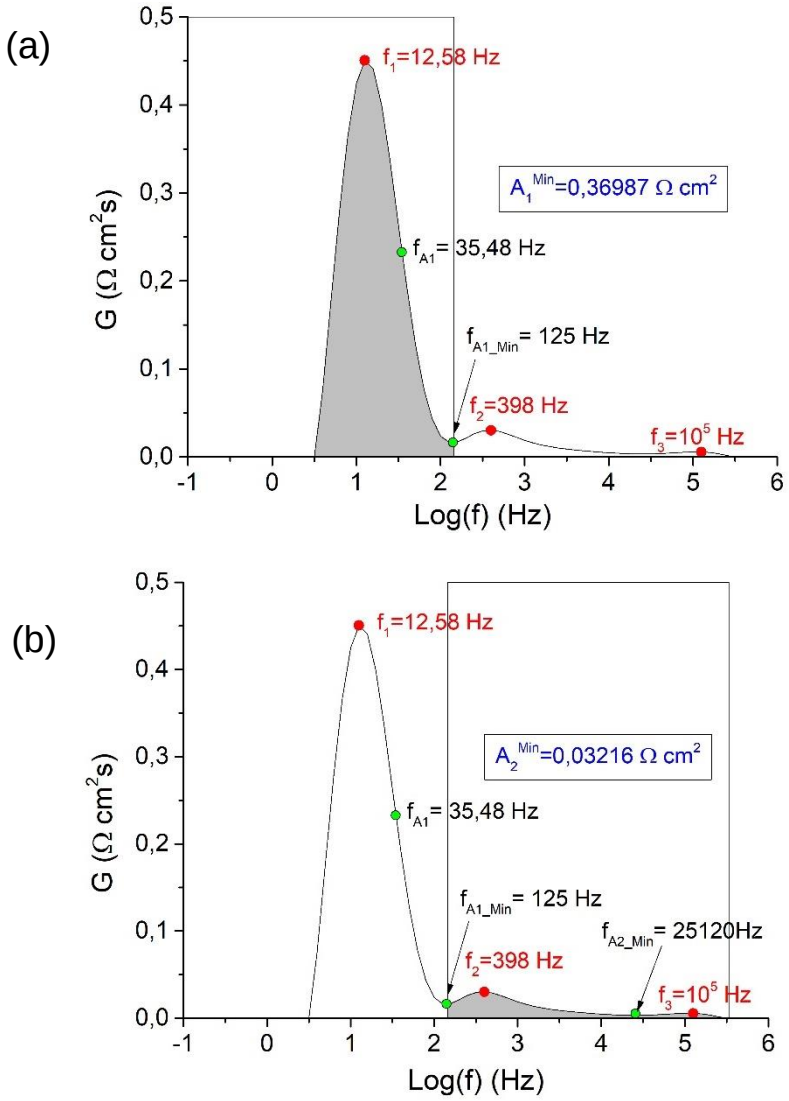

Fig. 5. 13 DRT curve for porous LBC64 sample at 600 °C and OCV condition, to evaluate polarization resistance of the different process at **(a)** low frequency and **(b)** high frequency.

Other important details about processes were provide by the curve shape. A well-centered peak, characteristic of a capacitive process that could be represented in an equivalent circuit analysis by a RQ subcircuit, where Q is a constant phase element with parameter n > 0.9, describes P1. On the other hand, P2 shows a broader frequency distribution in the medium range, that could indicate a higher diffusion contribute (CPE n-parameter < 0.9) (24).

Fig. 5. 14 is helpful to explain and to support better the correlation between DRT-curve shape and equivalent circuit proposed below. Here are reported the DRT spectra obtained from an electrochemical impedance spectroscopy simulation of (RQ) subcircuit, changing only the n-parameter of CPE.

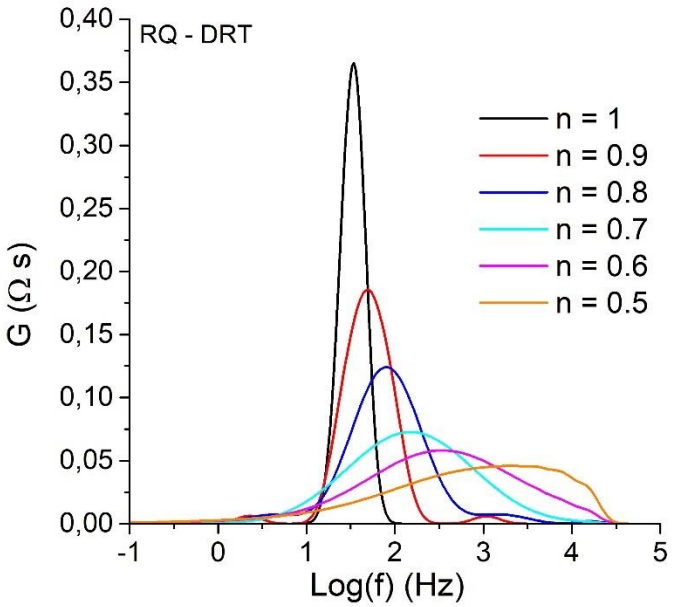

Fig. 5. 14 DRT simulation of RQ subcircuit as a function of n-parameter of constant phase element

Results well highlighted the strong effect of parameter *n* on DRT, varying from 1 (black line) to 0.5 (orange line). In the case of ideal capacitance (n=1) the DRT curve is characterized by a symmetric and narrow distribution, well centered on the expected characteristic frequency. Moving towards a Warburg-behavior (n=0.5), the distribution progressively lost its symmetry and frequency distribution became wider.

The evaluation of polarization resistance as global area under the curve allows to obtain activation energy from Arrhenius plot reported in Fig. 5. 15 (black pots). In this figure are also reported the activation energy for P1 (blue dots) and P2 (red dots). The value of 1.27 eV for global process is in agreement with the value calculated from experimental data of 1.29 eV and presented in Fig. 5. 10. Other two values for high and

low frequency processes will be compared with activation energy derived for single process from equivalent circuit analysis, presented in the following section.

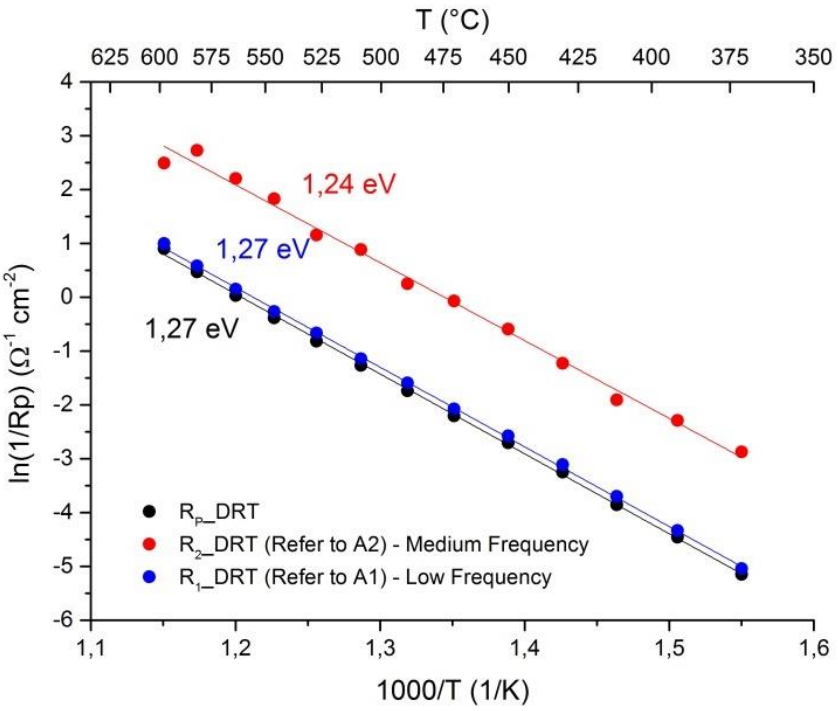

Fig. 5. 15 Evaluation of polarization resistance and activation energy of global process (Rp), medium frequency process and low frequency process by distribution of relaxation time.

- *Equivalent circuit analysis*

DRT analysis allows to make useful hypothesis for the equivalent circuit to analyze data. In the previous paragraph two main processes have been highlighted and for this reason an equivalent circuit described by $R_{el}(R_{HF}Q_{HF})(R_{LF}Q_{LF})$ has been employed (Fig. 5. 16). R_{el} is associated to the electrolyte resistance and the two following subcircuit are related to high-medium and low frequency processes, respectively.

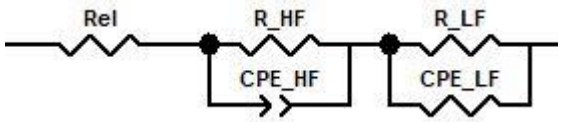

Fig. 5. 16 Equivalent circuit used to fit experimental data

As reported in **Fig. 5. 17** (a) and (b) the equivalent circuit chosen is able to fit all the samples in the whole temperature range (400 °C – 600 °C). In the impedance curves reported below, R_{el} contribution has been subtracted to direct compare the three electrode materials. The electrode contributions to the impedance have been identified for frequency lower than 10 kHz and 25 kHz at 400 °C and at 600 °C, respectively. Nevertheless, the semicircle at low frequency remains predominant even changing the temperature or electrode material. In accordance to the considered frequency range, in literature it is reported that for thin film electrode based on mixed ionic and electronic conductor the controlling processes are related with the oxygen exchange phenomena at electrode surface. Then, the phenomena involved can be several and their identification is not trivial. To provide more information and a deeper understanding the influence of operating parameters, such as oxygen partial pressure, has been taken into account in in the following paragraph.

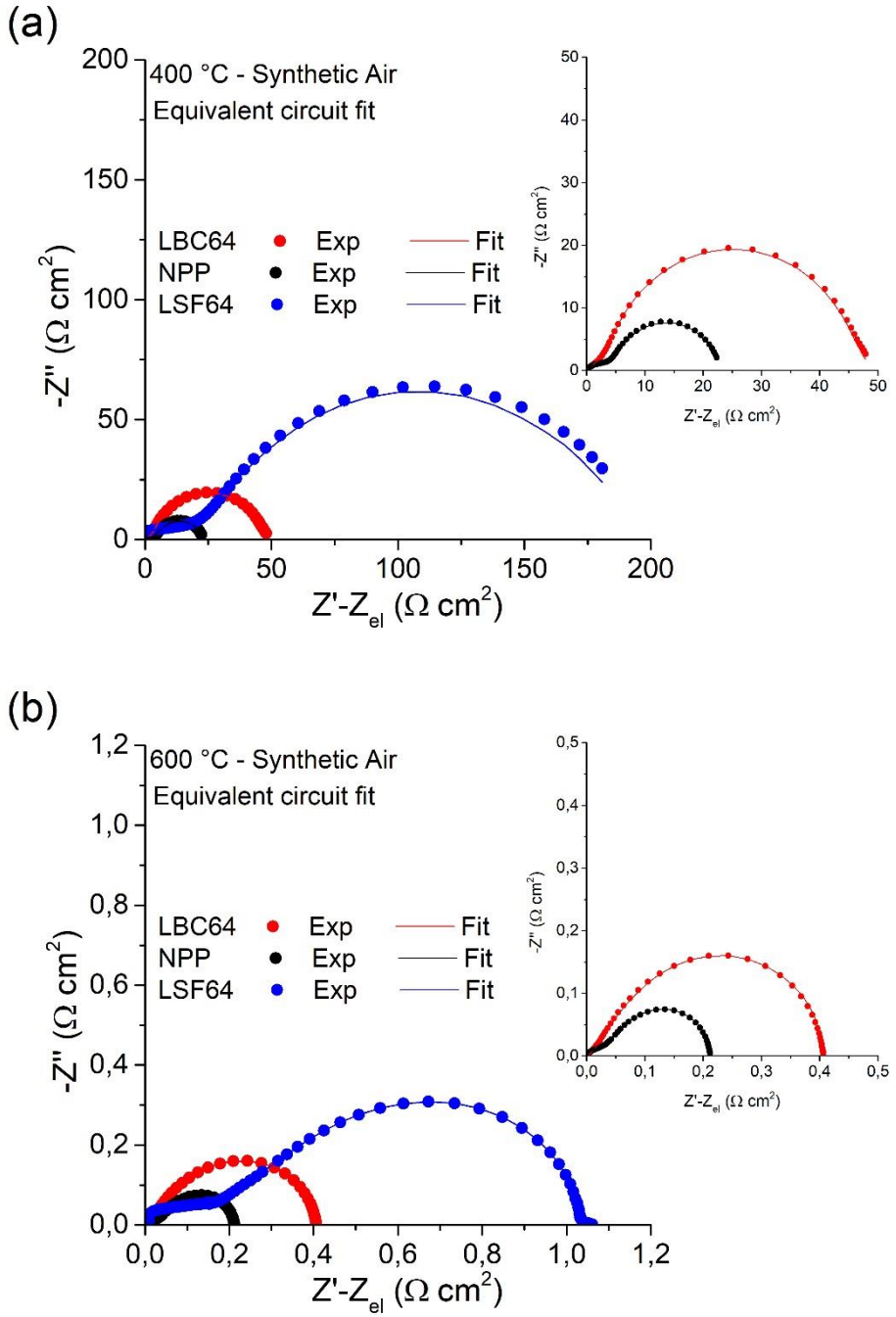

Fig. 5. 17 Nyquist plot with equivalent circuit fit superimposed for for LBC64 (red points), LSF64 (blue points) and NPP (black points) thin porous electrodes at **(a)** 400 °C and **(b)** 600 °C.

Each subcircuit and then for the related process, can be described by a characteristic frequency calculated as reported here:

$$f = \frac{1}{2\pi RC} \quad (5.1)$$

where R is the subcircuit resistance and C the equivalent capacitance associated to the constant phase element.

Both characteristic frequencies f_{HF} and f_{LF} change with the temperature, moving at higher values as summarized in Table 5. 4. This behavior pointing out a thermal activation of both processes and it is in accordance with DRT results.

	400 °C		**600 °C**	
	HF (Hz)	LF (Hz)	HF (Hz)	LF (Hz)
LBC64	6.25	0.30	97.01	13.57
NPP	22.10	0.10	189.47	5.41
LSF64	1.19	0.10	45.65	3.77

Table 5. 4 Characteristic frequencies for two subcircuit at boundary temperature range.

	400 °C		600 °C	
	n_{HF}	n_{LF}	n_{HF}	n_{LF}
LBC64	0.44	0.95	0.64	0.95
NPP	0.46	0.89	0.47	0.95
LSF64	0.47	0.91	0.63	0.92

Table 5. 5 Value of CPE – n parameter at boundary temperature range.

Fig. 5. 18 (a) and (b) report the Arrhenius plot for R_2 (high frequency) and R_3 (low frequency) resistances, respectively. The corresponding activation energy values are listed in Table 5. 6, which reports in the last column global activation energy values from Fig. 5. 10

	R_{HF} - E_{act}	R_{LF} - E_{act}	R_P – E_{act}
LBC64	1.20 eV	1.30 eV	1.28 eV
NPP	1.16 eV	1.31 eV	1.29 eV
LSF64	1.34 eV	1.47 eV	1.44 eV

Table 5. 6 Activation energy values for processes at high and low frequency. The last column reports the global activation energy.

Values comparison confirms that the low frequency process limit the overall behavior of all electrodes type, with activation energy values very close to those characteristic of global process. Moreover, the ratio between R_{LF} and $R_{P,}$ is always higher than 0.6, up to 0.9 for LBC64 at low temperature, confirming that oxygen surface activity is the limiting step for the three materials.

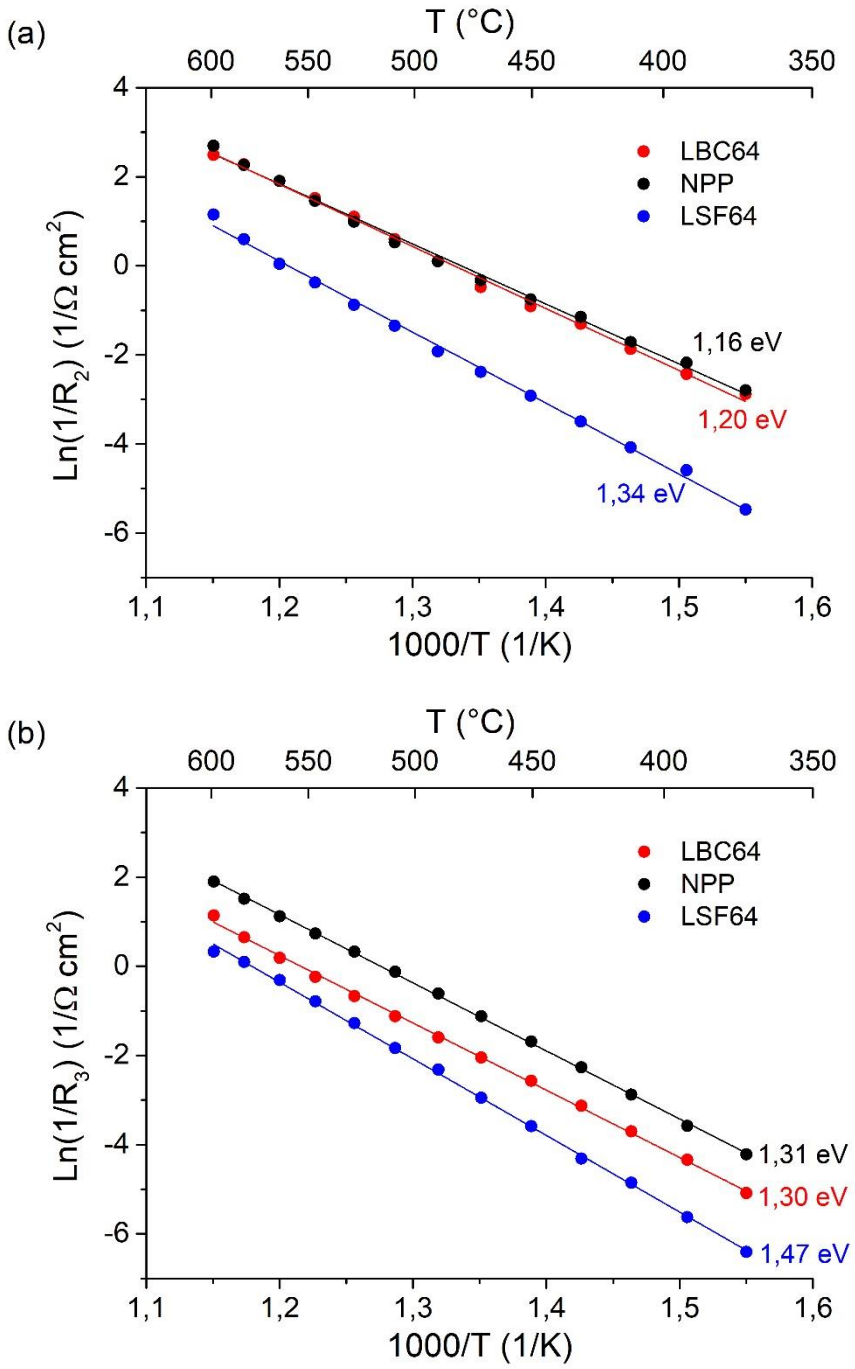

Fig. 5. 18 (a) R_2 and **(b)** R_3 behavior as a function of temperature for LBC64 (red points), LSF64 (blue points) and NPP (black points) thin porous electrodes from equivalent circuit analysis, and corresponding activation energies

Capacitance related with two processes are calculated with, their values as a function of temperature are reported in Fig. 5. 19 (a) and (b), respectively, and calculated as:

$$C = R^{\frac{1-n}{n}} Q^{\frac{1}{n}}$$

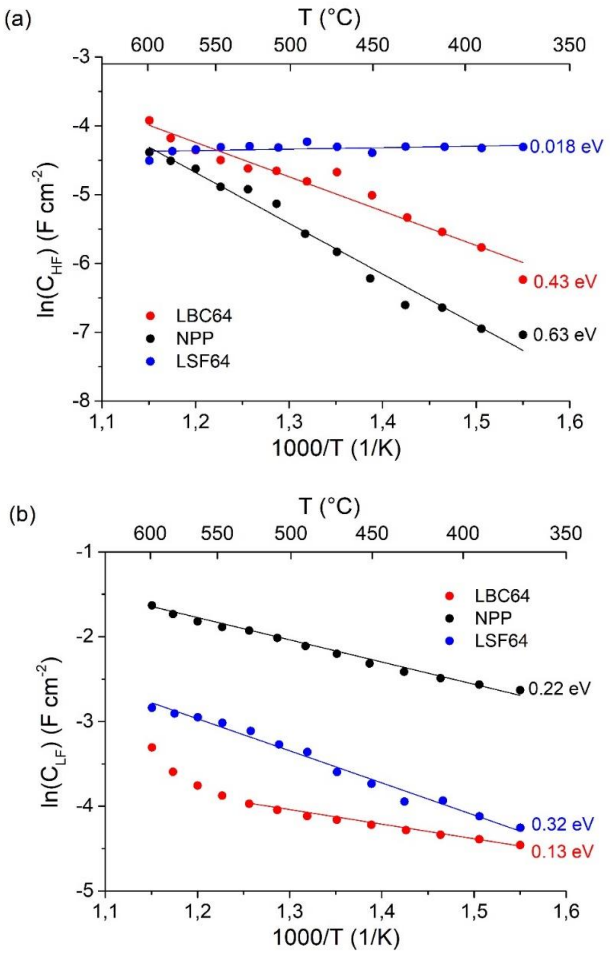

Fig. 5. 19 Evaluation of capacitance from equivalent circuit analysis at different temperature at **(a)** high frequency and **(b)** low frequency with corresponding activation energy evaluation.

The most interesting information are collected for the low frequency semicircle. In fact, C_{LF} is too high to be considered as a double layer capacitance and then will be treated as a chemical capacitance (25, 26). In $Ba_{0.099}Sr_{0.297}La_{0.594}Fe_{0.8}Co_{0.2}O_3$, the new perovskite phase (NPP), C_{LF} shows a huge increment if compared with the two starting material, LBC64 and LSF64. This relevant enhancement of C_{chem} in the NPP electrode,

linked with an increase of oxygen vacancy concentration as reported by several authors (27-29), favors oxygen ions transport leading to a lower polarization resistance as discussed above.

Comparison between DRT analysis and equivalent circuit results

The aim of this section is to compare results derived from DRT analysis and equivalent circuit fit, focusing in particular on process resistances and characteristic frequency.

Fig. 5. 20 illustrates the comparison of the $R_{p\ values}$ determined by DRT (A_P, A_2, A_1) and EC method (R_P, R_2, R_3). A good matching was found for the resistance at low frequency, and their ratio is quite close to 1 in the whole temperature range.

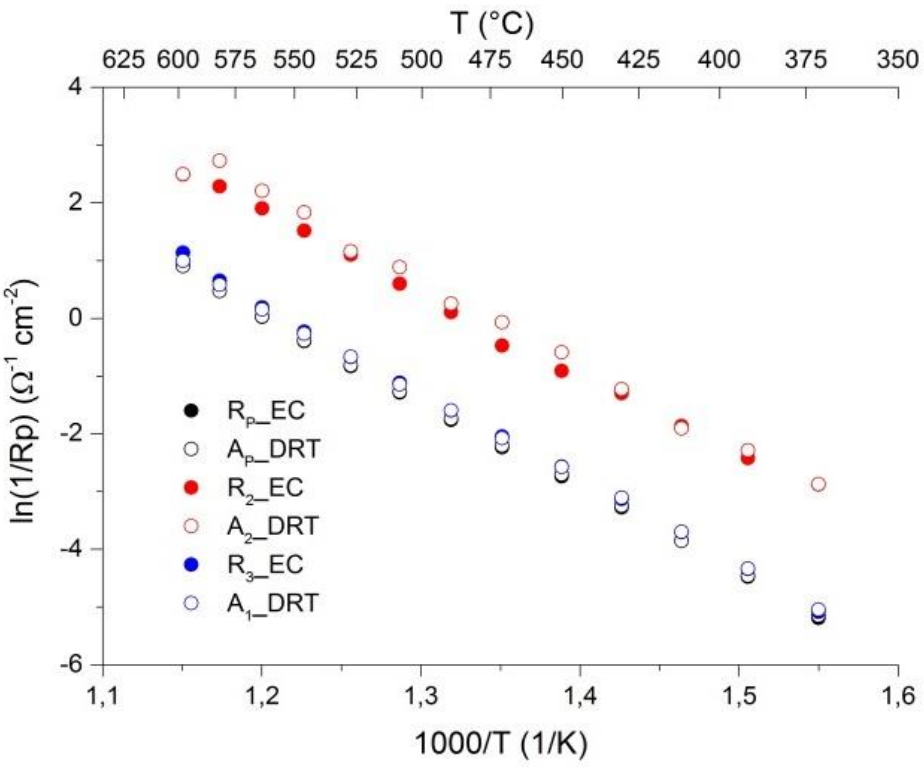

Fig. 5. 20 Comparison between polarization resistance (R_P), R_2 and R_3 values obtained from equivalent circuit (EC) and distribution of relaxation times (DRT) and as a function of temperature for LBC64 electrode.

A higher discrepancy was detected for resistance describing the process occurs at medium frequency (R_2 and A_2). Nevertheless, the effect of this uncertainty on the evaluation of the overall resistance is low, because this resistance represent a small fraction of the global process as discussed above.

Fig. 5. 21 (a) and (b) shows Nyquist and Bode plot, respectively, for LBC electrode obtained LBC at 600°C in synthetic air (this experimental measure has been used as example). On the both curves are reported characteristic frequencies obtained from DRT and EC analysis for the two main processes recognized and here considered.

The low frequency process is identify univocally by both methods close at 13 Hz, in agreement with Bode plot peak. About the second process DRT and EC detected two different frequency values, 398 Hz and 97 Hz, respectively. This difference could be explained by means of two consideration:

(i) the characteristic frequency extrapolated from DRT analysis was arbitrary chosen, taking into account the main peak value, even if the frequency dispersion range assigned to this process is much larger;

(ii) constant phase elements have the n-parameter (at 600°C n_{HF}=0.64 and n_{LF}=0.94), that can caused an interference in EC fit between two subcircuits, especially due to n_{HF} values, as reported in Chapter 2.

Then the fitting values (R and Q) can be reciprocally affected by the presence of the other mesh, influencing frequency calculation.

This approach just introduced to determine and compare characteristic frequency has been applied to the whole temperature range and results are summarized in Fig. 5. 22. A high quality matching between DRT and EC results was detected for low frequency process, where summit frequency extrapolated from two methods are overlapped. At higher frequency the discrepancy increase, in particular at high temperature, due to the reasons mentioned above.

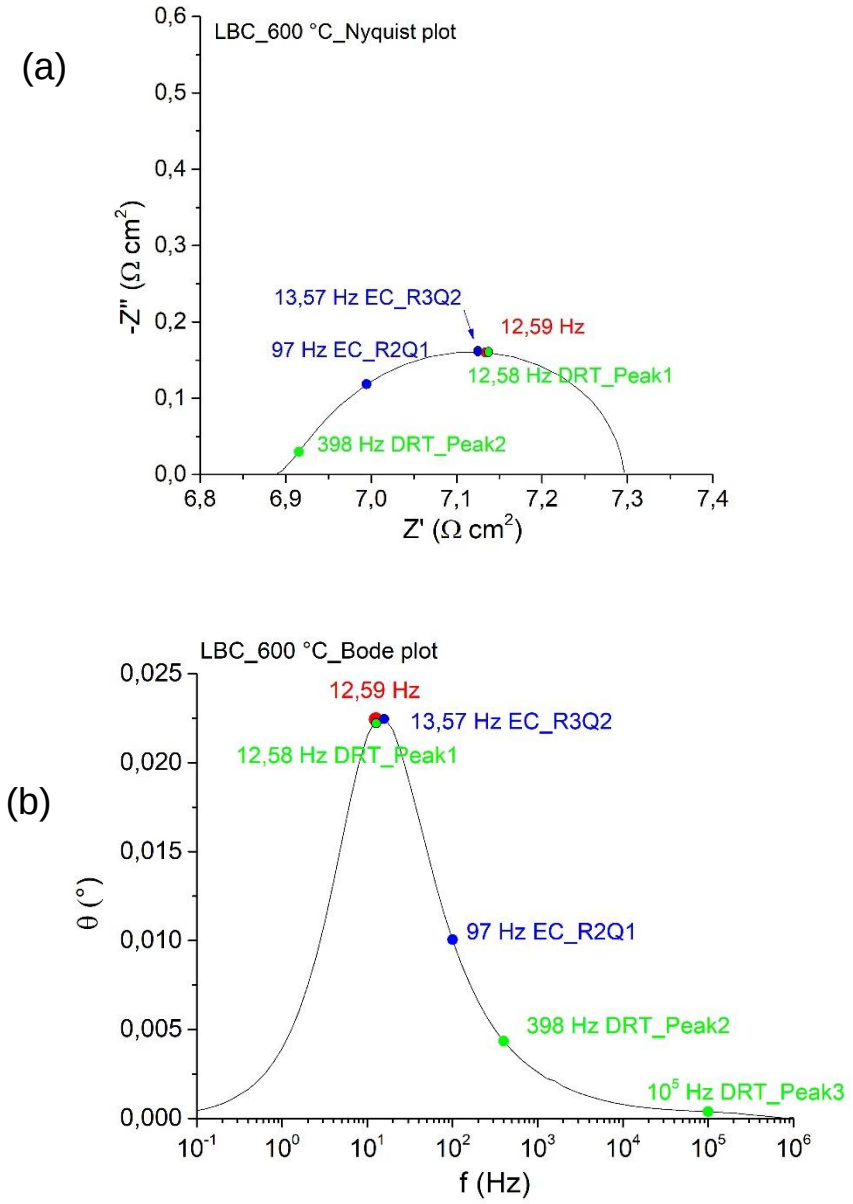

Fig. 5. 21 (a) Nyquist Plot and **(b)** Bode Plot for porous LBC electrode to compare the characteristic frequency obtained by DRT and EC analysis.

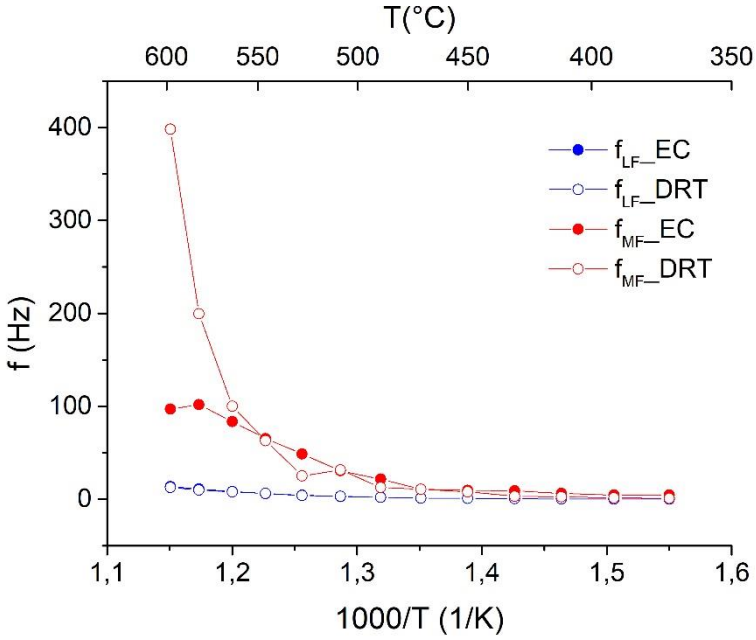

Fig. 5. 22 Comparison of characteristic frequency obtained with DRT and EC for low and high frequency processes.

The second parameter taken into account was oxygen partial pressure (p_{O_2}) in a range of 1-0.02 bar. Influence of p_{O_2} was investigated at different temperature between 460 – 600 °C. All three electrode materials increase their R_P decreasing p_{O_2}, as reported in Fig. 5. 23 (a - f) for LBC64, NPP and LSF64 at boundary range temperature. To better compare impedance data results are presented subtracting the electrolyte resistance at high frequency (Z'_{el}) that is independent by oxygen partial pressure.

The low frequency arc is highly dependent by oxygen partial pressure, while form the inset of each graph (Fig. 5. 23) it is clear that the system at high frequency for is unaffected by oxygen partial pressure change.

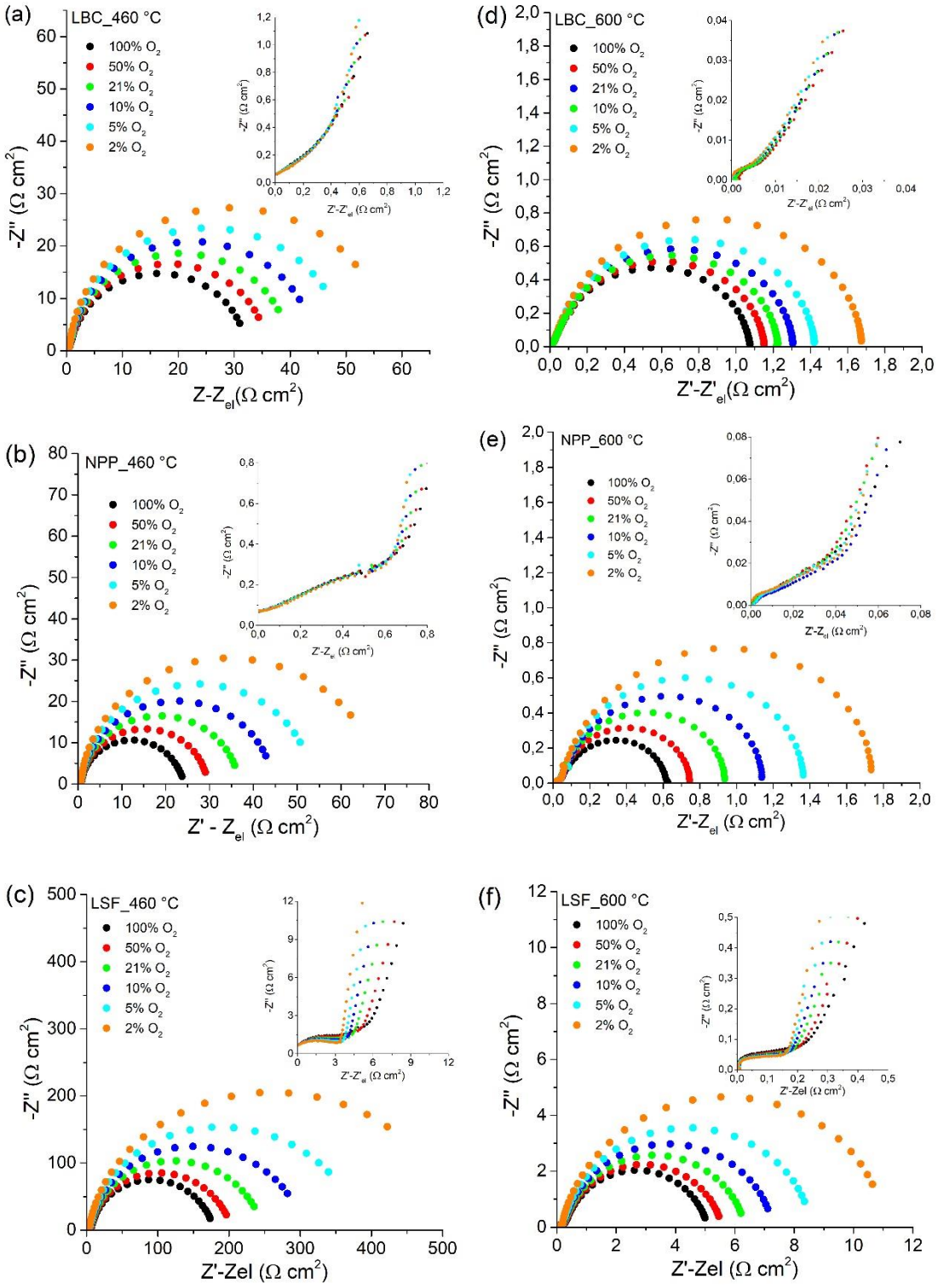

Fig. 5. 23 Electrochemical impedance spectroscopy at **(a) (b) (c)** 460 °C and **(d) (e) (f)** 600 °C for **(a) (d)** LBC64, **(b) (e)** NPP **(c) (f)** LSF64 thin film electrodes on YSZ substrates as a function of oxygen partial pressure. Figure insets highlight high frequency part

Oxygen partial pressure frequency dependence is also well highlighted by DRT analysis in Fig. 15 (d) (e) and (f). The area under the peak at low frequency grow up, decreasing p_{O_2} inside the cell. Moreover, also the related peak-frequency shifted to a lower value, indicating a slowdown of phenomena rates.

The equivalent circuit used is the same presented above for the study of temperature influence. As introduced before the main process is always at low frequency (0.1 – 10 Hz, as a function of material electrode); DRT showed a peak at medium frequency (10-1000 Hz), with a broad dispersion. This is in accordance with the n-parameter value obtained from EC-fit that never overcame 0.60.

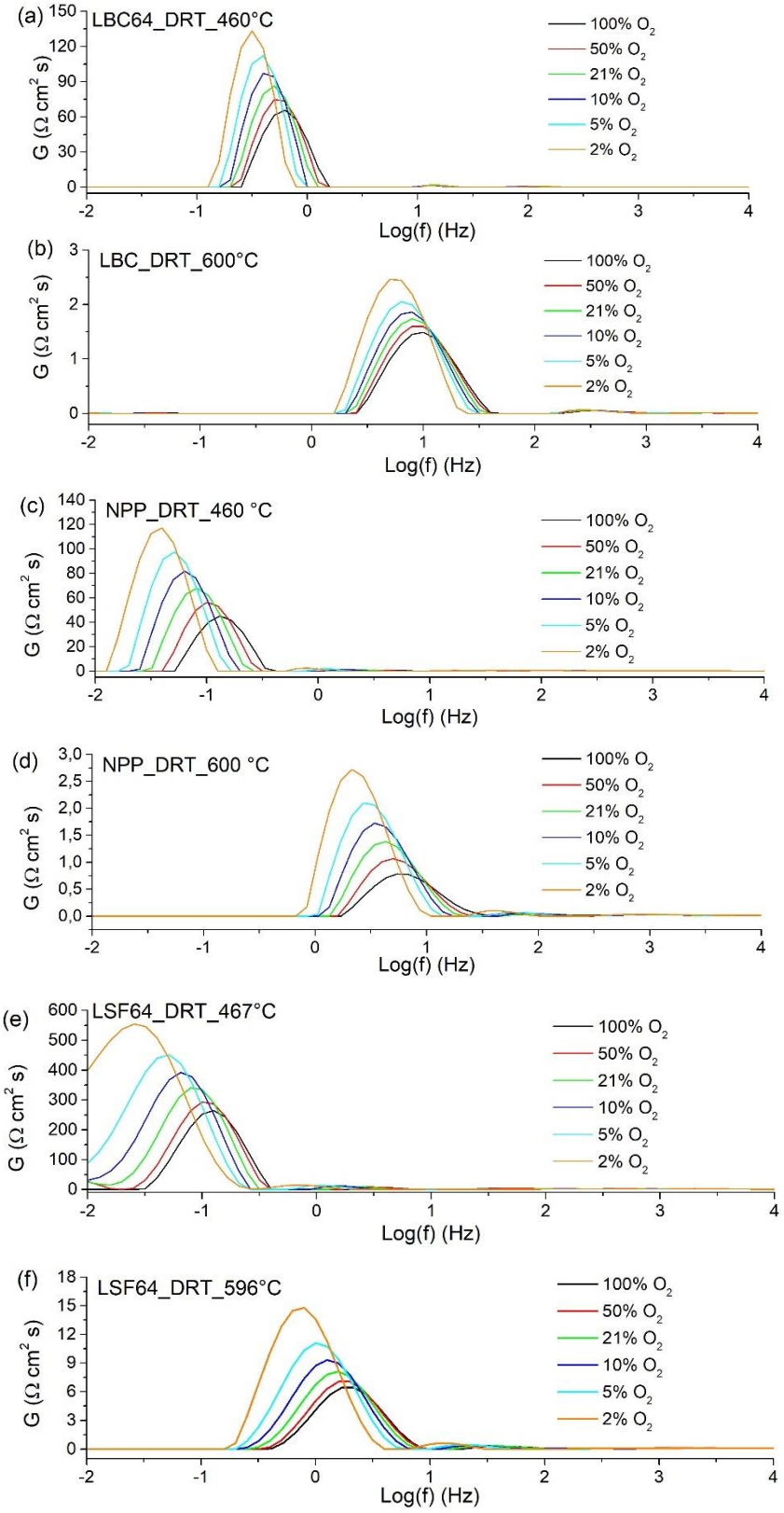

Fig. 5. 24 Distribution of relaxation times for **(a) (b)** LBC64, **(c) (d)** NPP, **(e) (f)** LSF64 at 460 °C and 600 °C at different oxygen partial pressure.

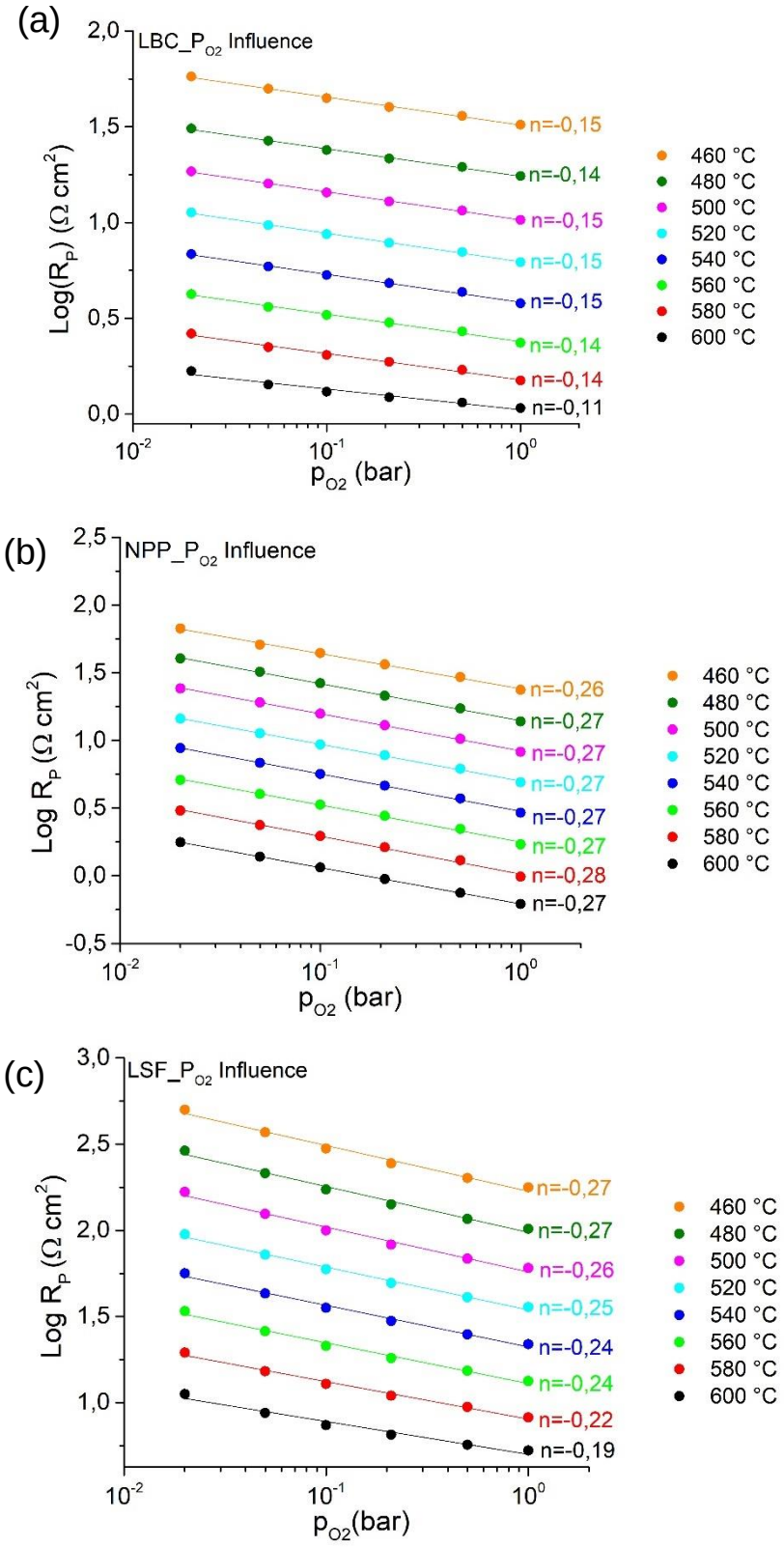

Fig. 5. 25 Polarization resistance evaluation at different temperature and different oxygen partial pressure **(a)** LBC64 **(b)** NPP **(c)** LSF64.

Extending the analysis, for each temperature was possible to identify a clear dependence of R_P as a function of p_{O_2}, described by well-known relationship:

$$R_p = Log(p_{O_2}^{-n}) \quad (5.1)$$

Three electrodes have a quite constant n – exponent as a function of temperature, meaning that even the rate determining step does not change between 460 -600 °C. It is possible to make hypothesis about possible limiting step, and as proposed in literature (30, 31) oxygen reduction to oxide ion follow these global scheme, using Kroger – Vink notation:

$$\frac{1}{2}O_2(g) + 2e^- + V_{\ddot{O}} \rightarrow O_O^X \quad (5.2)$$

Oxygen reduction reaction (ORR) is a multi-step reaction, which includes many processes extremely difficult to separate such as i) gas diffusion ii) adsorption and dissociation of oxygen on the electrode surface iii) charge transfer. In Table 5. 7 these processes are summarized with their peculiar n-exponent related with oxygen partial pressure dependence as reported in (32)

Process	Reaction	p_{O2} n-exponent
Diffusion and adsorption on electrode surface	$O_2(g) \leftrightarrow O_{2ad}$	-1
Dissociation of adsorbed molecular oxygen into atomic oxygen	$O_{2ad} \leftrightarrow 2O_{ad}$	-1/2
Charge transfer from the cathode to atomic oxygen	$O_{ad} + e^- \leftrightarrow O_{ad}^-$	-3/8
Solid-phase migration of oxide ion from the cathode to the TPB	$O_{ad}^- \leftrightarrow O_{TPB}^-$	-1/4
Reduction monovalent oxide ion at TPB	$O_{TPB}^- + e^- \leftrightarrow O_{TPB}^{2-}$	-1/8
Diffusion of the oxygen ion from TPB to the electrolyte, associate with a charge transfer process	$O_{TPB}^{2-} + V_{\ddot{O}} \leftrightarrow O_O^X$	0

Table 5. 7 List of possible steps involved in ORR and their p_{o2} n- exponent (32)

In our case LBC64, NPP, LSF64 have an average n-exponent equal to -0.14, -0.26, -0.24, respectively. This pointing out that LBC64 has a weaker p_{O2} dependence than other two materials. For this material, based on Table 5. 7, a possible rate determining step in the oxygen partial pressure range considered is the reduction of oxide ion at TPB. Nevertheless, NPP and LSF64 have a quite similar oxygen partial pressure dependence, with a solid phase migration to three phase boundary as controlling process. In Fig. 5. 26 (a – b) are plotted resistance at low and high frequency at boundary range temperature (460 – 600 °C) and n-exponent for Eq.(5.1) are summarized in Table 5. 8. However, the complete understanding of mechanism is still open and it will be faced in future work.

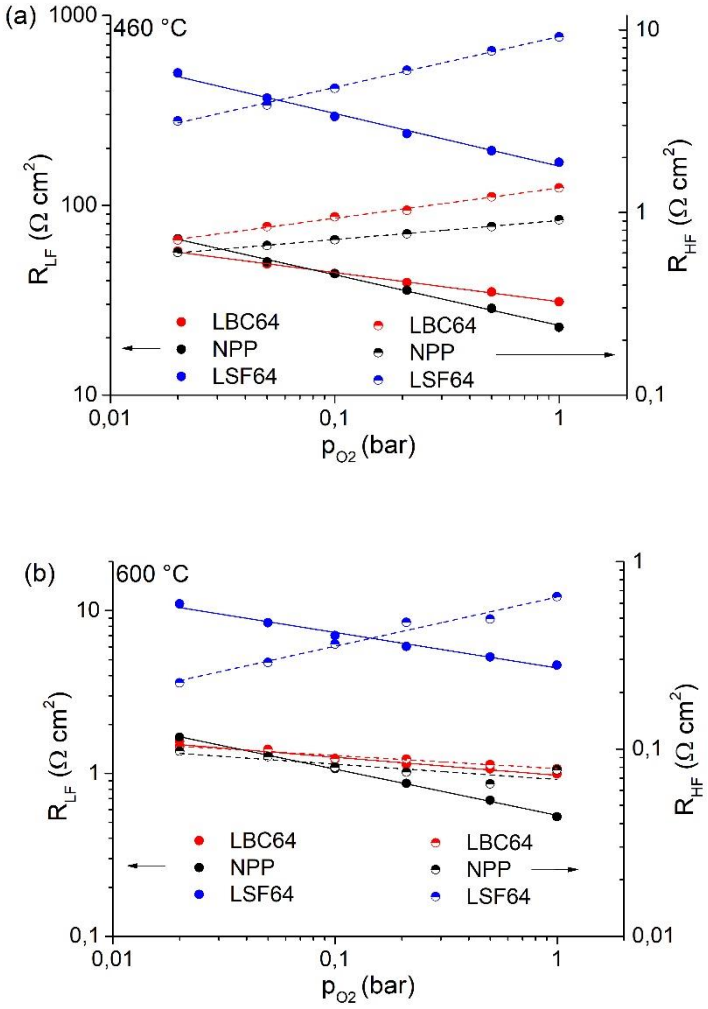

Fig. 5. 26 Evaluation of oxygen partial pressure dependence of R_{HF} (right-axis) and R_{LF} (left –axis) at **(a)** 460 °C and **(b)** 600 °C.

	LBC		**NPP**		**LSF64**	
	n_{HF}	n_{LF}	n_{HF}	n_{LF}	n_{HF}	n_{LF}
460 °C	0.16	-0.15	-0.10	-0.26	-0.27	-0.27
600 °C	-0.07	-0.11	-0.08	-0.28	0.26	-0.21

Table 5. 8 Evaluation of n – exponent p_{O2} dependence at 460 °C – 600 °C for high and low frequency processes for the three different samples.

The results (Fig. 5. 26 Table 5. 8) confirm how the low frequency process dominates the global electrode process. For all the materials, p_{O2} dependence obtained for low frequency subcircuit is completely in agreement with the dependence obtained from the evaluation of overall electrode resistance (Fig. 5. 25).

MIEC performance are highly affected by their capacitance. Fig. 5. 27 reports capacitance values at high and low frequency at 460 °C and 600 °C, used as examples. In all temperature conditions both capacitance are considered as chemical capacitance, and the increasing of the temperature grows up this quantity. As discuss in temperature influence section, low frequency process has a higher C_{chem} value and among the three cathode material NPP electrode has the highest capacitance. The new perovskite structure should be favored by its stoichiometry that produce an increment of oxygen vacancy concentration closely linked with C_{chem} magnitude. These results have been confirmed also by experiments at different oxygen partial pressure (Fig. 5. 27 (b) (d)); moreover, C_{chem} is unaffected by oxygen partial pressure variation within the pressure range considered, especially for LBC64 and LSF64 sample. Only NPP electrode show a slight increment of C_{chem} for p_{O2} lower than 0.2 bar.

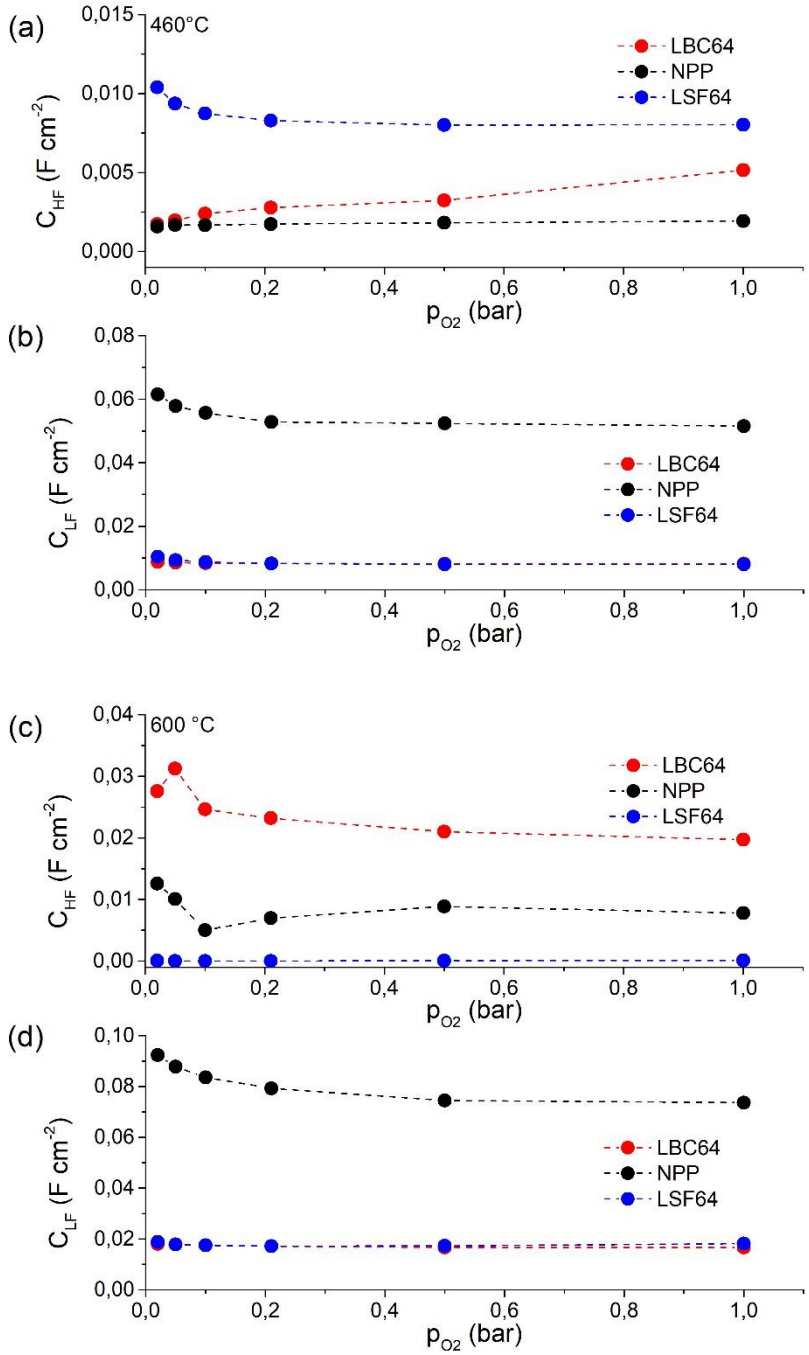

Fig. 5. 27 Capacitance at **(a) (c)** high frequency and **(b) (d)** low frequency, extrapolated with equivalent circuit analysis at boundary temperature range.

5.4 Bilayer system characterization

Two different cell configuration have been used to evaluate the activation of thin dense LSF64 electrode by means a LBC64 thin top layer. A reference LSF64 electrode with a thickness of 200 nm has been produced, while the bilayer systems have been obtained with the addition of a LBC layer, changing its structure, as reported in Fig. 5. 28 and Fig. 5. 29 (a) (c). In case (b) (c) 50 nm LBC layer is dense and porous, respectively. The densification of the structure has been achieved increasing deposition temperature from 450 °C to 650 °C (Table 5. 3). To properly compare electrode performance the global thickness was fixed at 200 nm.

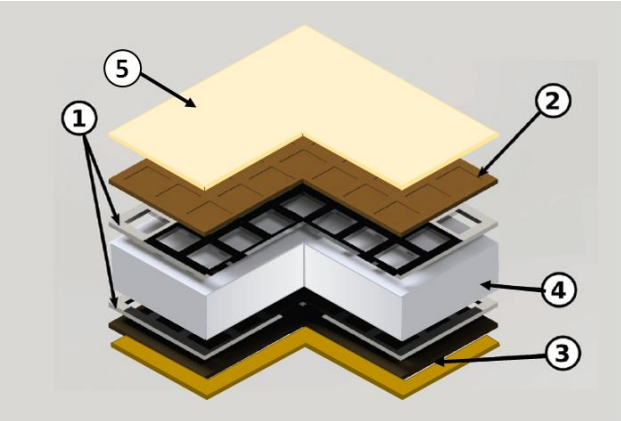

Fig. 5. 28 Sketch of cell configuration **(1)** Platinum current collector **(2)** Working electrode **(3)** counter electrode **(4)** YSZ electrolyte **(5)** top layer. Image adapted from (5)

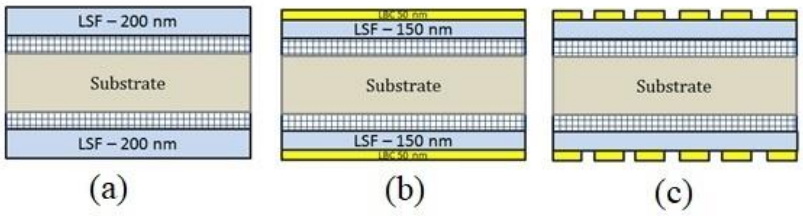

Fig. 5. 29 Front sketch of cells used to investigate the effect of a thin LBC top layer. **(a)** dense thin film (200 nm) LSF64 **(b)** dense thin film (150 nm) + dense LBC top layer (50 nm) **(c)** dense thin film (150 nm) + porous LBC top layer (50 nm)

5.4.1 Microstructural characterization

In the previous section the interaction between LSF64 and LBC64 have been investigated in different conditions. The results show a strong cation interdiffusion between the two materials with the formation of a new perovskite phase $Ba_{0.099}Sr_{0.297}La_{0.594}Fe_{0.8}Co_{0.2}O_3$ (named NPP). Nevertheless, in this case two materials get in touch in a different way, being deposited on YSZ supported at different time. This choice leads to maintain separate the phases, preserving the initial LSF64 and LBC64 materials as detected by X-ray diffraction analysis reported in Fig. 5. 30.

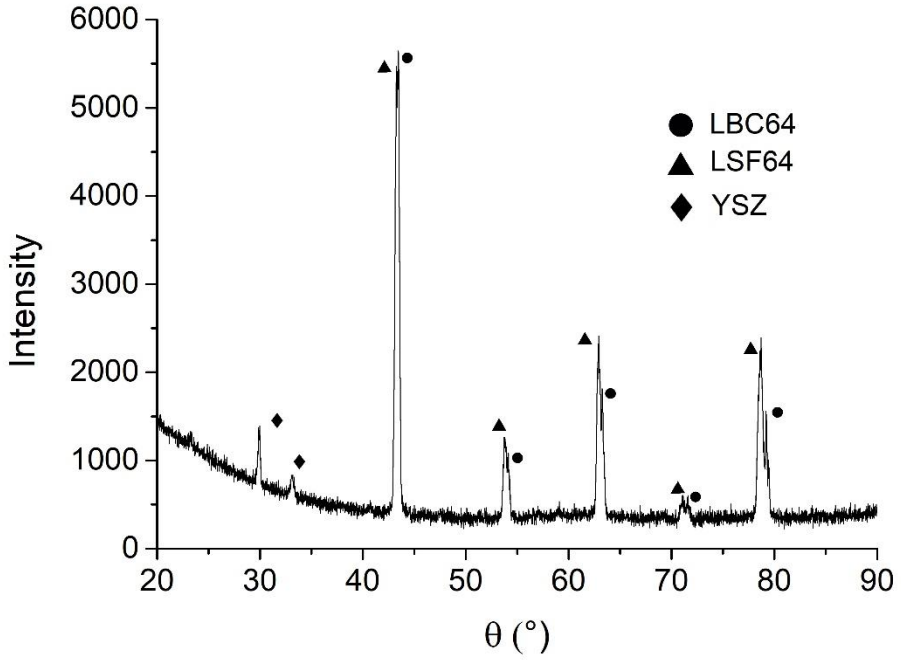

Fig. 5. 30 X-ray diffraction for bilayer system

5.4.2 Electrochemical characterization

Reference electrode and bilayer systems have investigated by means of electrochemical impedance spectroscopy in a temperature range of 460 – 600 °C and varying the oxygen partial pressure between 1 to 0.02 bar. Impedance measurements have been collected in a frequency range of $10^6 \div 10^{-2}$ with a voltage perturbation of 10 mV using a Novocontrol PotGal electrochemical test station.

The evaluation of the effects of LBC64 top layer and its geometry on LSF64 dense thin film starts considering the influence of temperature. From Fig. 5. 31, which reports impedance curves at 460 °C and 600 °C in synthetic air, two consequences are clear:

i. the presence of LBC64 top layer drastically reduce polarization resistance in the whole temperature range.

ii. the structure (dense or porous) of LBC64 top layer does not affect the performance of bilayer systems.

The first point, concerning with the polarization resistance drop due to the LBC64 addition, is explained by the different oxygen surface exchange resistance between LSF64 and LBC64 (9, 32). In fact, the substitution of LSF with LBC at gas-electrode interface favors surface phenomena. The discussion dealing with the absence of effects between the dense and the porous structure it is not trivial, and can be related with the extremely high activity of LBC for surface phenomena that cannot be enhanced by a so thin porous structure.

Distribution of relaxation times in Fig. 5. 32 provides important information about the process more affected by the presence of LBC64 top layer. It is evident that the low frequency peak strongly decreases by the presence of new material over LSF64. At 460 °C, Fig. 5. 32 (a), LSF64 has the main peak at low frequency not complete, and this is also in accordance with EIS curve shape and depends by lower frequency boundary range. In bilayer system, area under this peak drastically downs and the peak itself is localized at higher frequency, pointing out a faster process. This result is in agreement with material properties and with the improvement caused by the presence of LBC64 at gas interface.

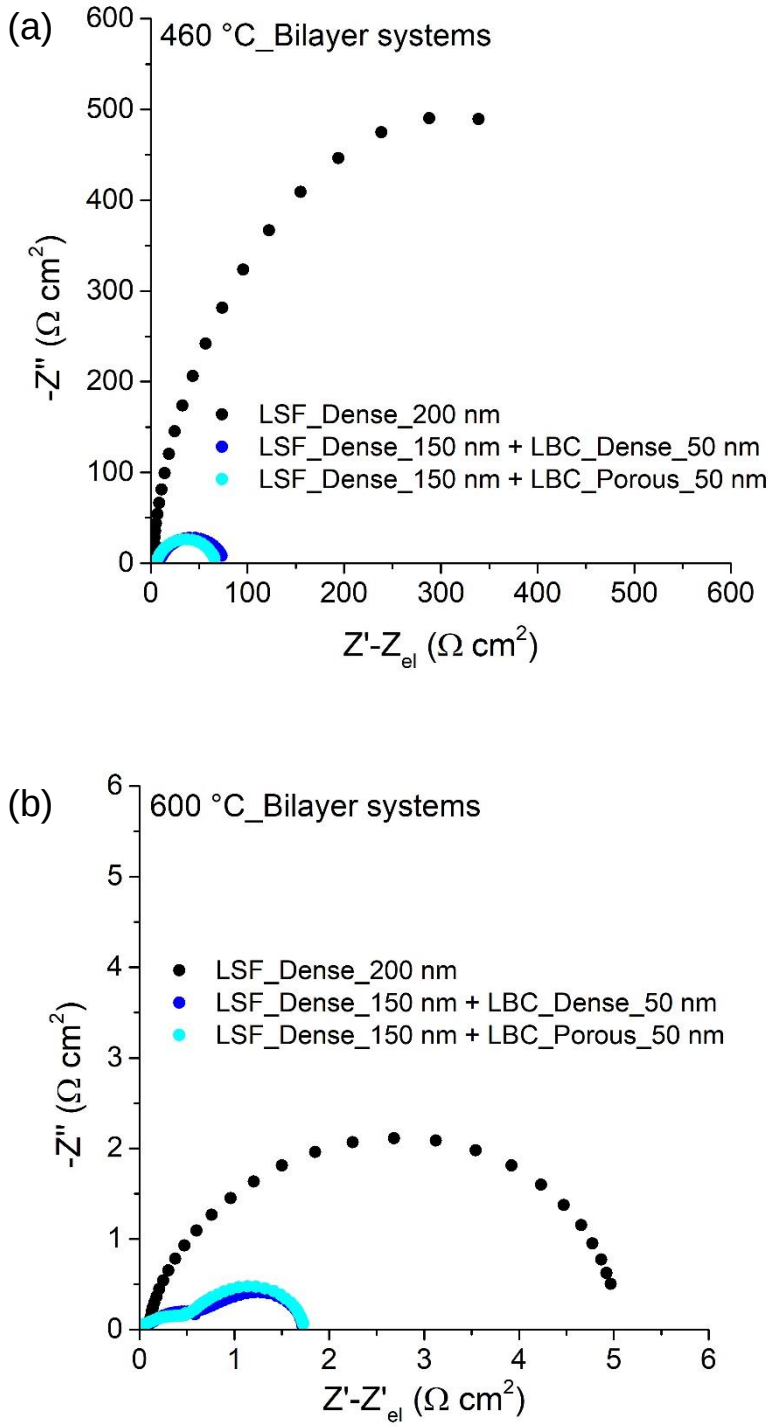

Fig. 5. 31 Electrochemical impedance spectroscopy at **(a)** 460 °C and **(b)** 600 °C for three electrode systems on YSZ substrates.

Moving at upper boundary temperature, 600 °C, the same behavior has been identified with a noteworthy decrease of electrode resistance at low frequency. In this case peak frequency shift is less pronounced than this at 460 °C, but occurs confirming the benefits brought about LBC64 presence.

From DRT is also clear that the process at low frequency considered above controls electrode performance. In particular, this resistance represents at least the 90 % of global resistance for pure dense thin LSF 64 film in the all operating conditions considered, then the overall electrode resistance can be approximated with its value. This hypothesis will be confirmed by equivalent circuit analysis presented below. For other two electrode configurations the ratio R_{LF}/R_P is included in a wider range (0.7 ÷ 0.98); however, also for these cases R_{LF} remains ascribable to the limiting process.

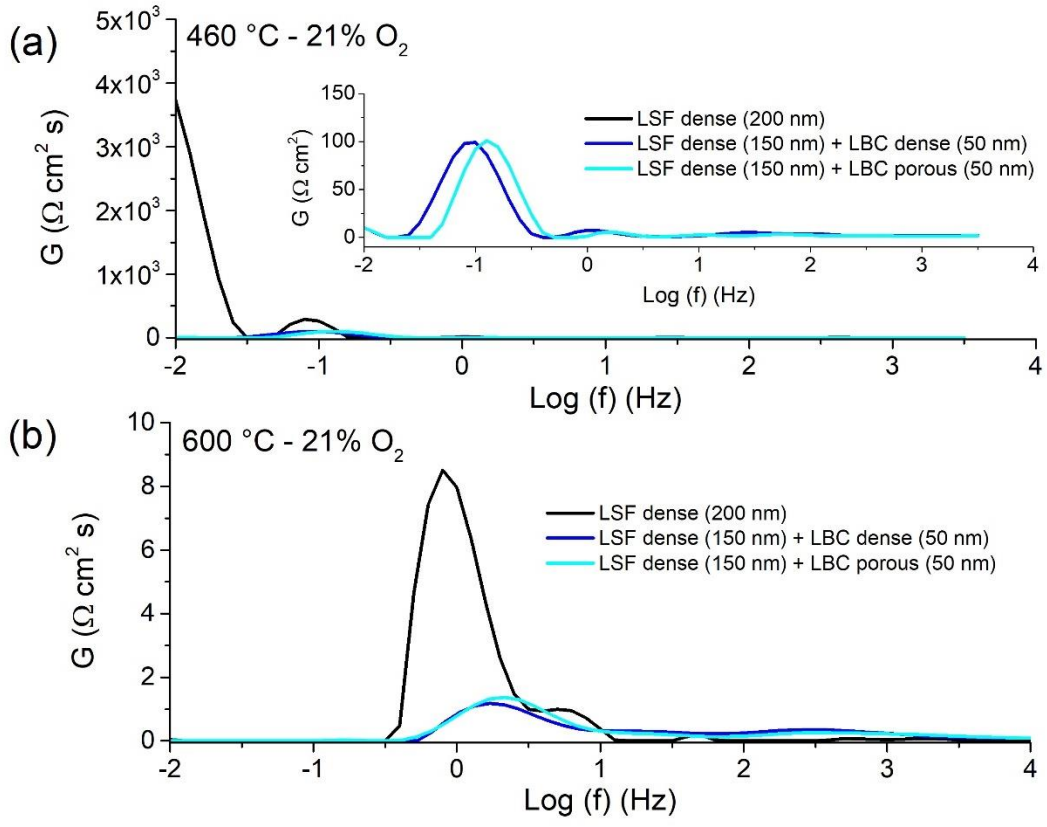

Fig. 5. 32 Distribution of relaxation times at **(a)** 460 °C and **(b)** 600 °C at 21% O_2 for all the three electrodes considered.

Distribution of relaxation time evidences the presence of two processes. As just introduced above, low frequency impedance arc is enough predominant to consider negligible the high frequency part. From these considerations, the equivalent circuit analysis has been proposed employing the most used electrical circuit composed by $R_{el}(R_{HF}Q_{HF})(R_{LF}Q_{LF})$. The discussion will be primarily focus on low frequency section.

The first parameter evaluate has been the global polarization resistance (R_P), and the natural logarithm of reciprocal values are graphed in Fig. 5. 33 at different oxygen partial pressure. It can be observed that for each sample, activation energy changes decreasing the oxygen partial pressure, while on the polarization resistance, p_{O2} has an opposite effect. All the activation energy values are reported in Table 5. 9.

Oxygen Partial Pressure	**Sample A**$^{(1)}$ R_p E_{act} (eV)	**Sample B**$^{(2)}$ R_p E_{act} (eV)	**Sample C**$^{(3)}$ R_p E_{act} (eV)
100 % O_2	2.02	1.68	1.64
50 % O_2	1.98	1.63	1.59
21 % O_2	1.97	1.60	1.55
10 % O_2	1.95	1.57	1.53
5 % O_2	1.93	1.55	1.49
2 % O_2	1.89	1.51	1.43

Table 5. 9 Activation energy values at different oxygen partial pressure calculated in a temperature range of 460 – 600 °C. **(1)**: Dense LSF64 (200 nm) **(2)**: Dense LSF64 (150 nm) + Dense LBC top layer (50 nm) **(3)**: Dense LSF64 (150 nm) +Porous LBC64 top layer (50 nm).

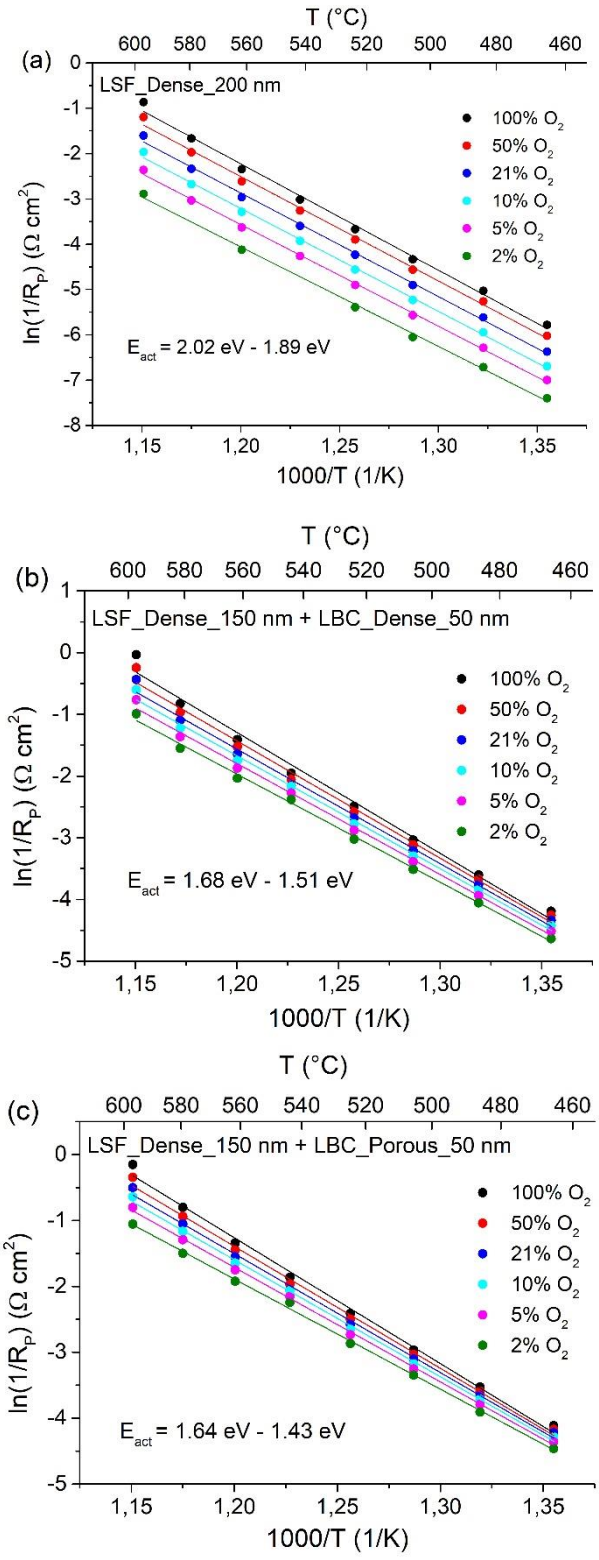

Fig. 5. 33 Arrhenius plot for **(a)** dense thin film (200 nm) LSF64 **(b)** dense thin film (150 nm) + dense LBC top layer (50 nm) **(c)** dense thin film (150 nm) + porous LBC top layer (50 nm) at different oxygen partial pressure.

Activation energy values for LSF64 extrapolated in Fig. 5. 33 and summarized in Table 5. 9 are in agreement with those reported in literature for dense LSF thin film electrode (33). The addition of LBC64 top layer decreases the activation energy up to 25 %, as a function of top layer structure and oxygen partial pressure. The positive effect it is explainable by the decreasing of activation energy of the process related with surface phenomena and which occurs at low frequency, as introduced above during DRT discussion. LBC64 provides a higher electrocatalytic activity than LSF64, especially for the oxygen surface reaction (9). Nevertheless, the results highlight also that a LBC top layer with a porous structure (Sample C Table 5. 9) has a lower activation energy than the dense one (Sample B Table 5. 9).

Further information concerning resistance and activation energy for single processes at high and low frequency as a function of temperature and at different oxygen partial pressure, are reported in Fig. 5. 34 (a-f) and Table 5. 10 for all the samples.

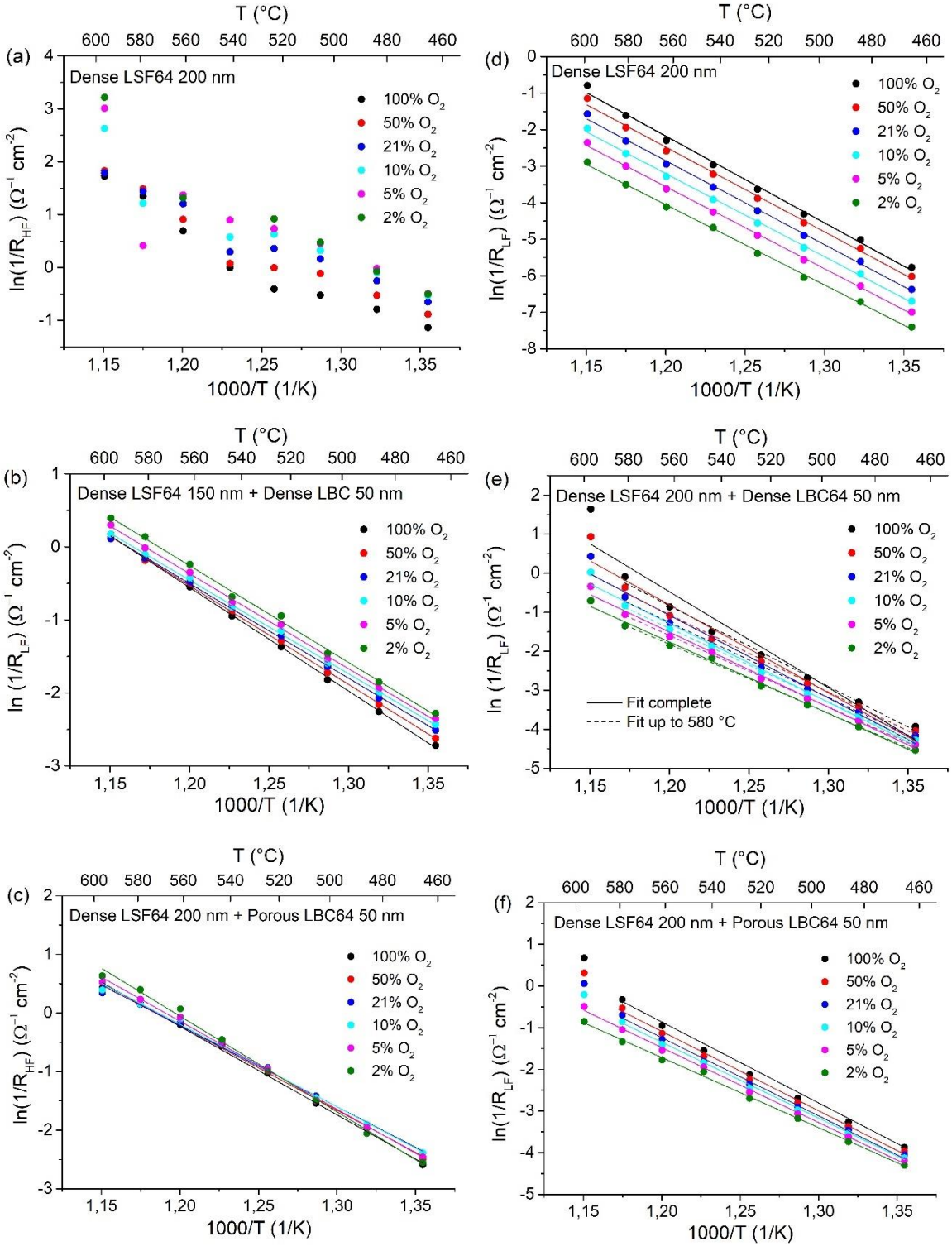

Fig. 5. 34 Arrhenius plot for **(a – c)** R_{HF} and **(d – f)** R_{LF} for reference dense LSF64 sample and two bilayer electrode system at different oxygen partial pressure (100% - 2% O_2) and temperature (600 – 460 °C).

Resistance at high frequency (R_{HF}) has not a unique trend for all the electrodes; pure dense LSF64 sample shows a not clear trend (**Fig. 5. 34** (a)) especially for temperature higher than 540°C; one possible reason about this uncertainty can rise from equivalent circuit analysis. In fact, fit at high frequency has a quite higher error (over 20%) and then can introduce inaccuracy. Nevertheless, for this sample the arc refers to the high frequency resistance is less than 1% of the total polarization resistance and not affects the fitting results and discussion about the main electrode process at low frequency.

The other two samples, with LBC64 as top layer, show a R_{HF} linear trend (**Fig. 5. 34**b-c), but weakly affected by the oxygen partial pressure. The slight dependence by p_{O2} leads to a decrease of R_{HF} lowering the oxygen partial pressure.

	Sample A(1)		**Sample B(1)**		**Sample C(1)**	
	R_{HF} E_{act} (eV)	R_{LF} E_{act} (eV)	R_{HF} E_{act} (eV)	R_{LF} E_{act} (eV)	R_{HF} E_{act} (eV)	R_{LF} E_{act} (eV)
100 % O_2	-	2.04	1.14	1.78	1.30	1.68
50 % O_2	-	2.00	1.12	1.71	1.24	1.63
21 % O_2	-	1.98	1.11	1.66	1.19	1.59
10 % O_2	-	1.96	1.10	1.62	1.21	1.56
5 % O_2	-	1.94	1.16	1.57	1.29	1.50
2 % O_2	-	1.89	1.22	1.52	1.40	1.44

Table 5. 10 Activation energy values at different oxygen partial pressure calculated in a temperature range of 460 – 600 °C for processes at high and low frequency. **(1)**: Dense LSF64 (200 nm) **(2)**: Dense LSF64 (150 nm) + Dense LBC top layer (50 nm) **(3)**: Dense LSF64 (150 nm) +Porous LBC64 top layer (50 nm).

Fixed operating temperature, R_p variation as a function of oxygen partial pressure highlight a clear change in the slope, illustrated in **Fig. 5. 35**. Dense thin film made by only pure LSF64 has an n-exponent equal to 0.51 while at the presence of LBC64 top layer corresponds a value close to 0.23.

Previously it has been introduced how the value of this parameter can help to make hypothesis regarding the rate determining step. In agreement with literature an n value equal to 0.51 is associable to a dissociation of adsorbed molecular oxygen into atomic oxygen at electrode surface, while 0.23 is close to 0.25 related with a solid-phase migration of oxide ion from the cathode to the TPB. The variation proposed here about the limiting step is in accordance with material properties, and results previously discussed in DRT analysis. The addition of LBC64 as top layer at gas/electrode interface drastically decrease the surface process resistance, which dominated LSF64 electrode, and then the transport of oxygen ion became limiting.

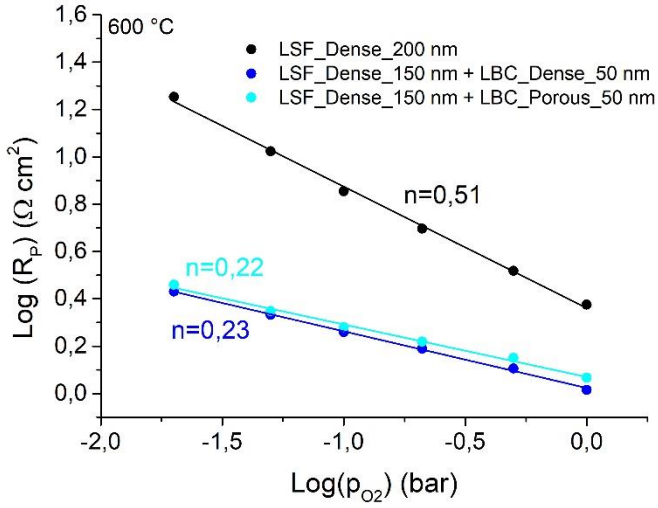

Fig. 5. 35 Dependence of polarization resistance on oxygen partial pressure dependence at 600 °C.

5.5 Summary

$La_{0.6}Sr_{0.4}Fe_{0.8}O_3$ and $La_{0.6}Ba_{0.4}CoO_3$ were tested in several thin film electrode configurations. First of all, particular attention has been dedicated to evaluate interaction between these two materials in different conditions. Microstructural results showed a strong interdiffusion between materials in two particular conditions. Interdiffusion occurred (i) when two powders were sintered after mixing process at, and (ii) in PLD chamber depositing LSF64 and LBC64 simultaneously starting from two difference pellets.

Microstructural analysis identified a new perovskite phase (NPP) with a stoichiometry of $Ba_{0.099}Sr_{0.297}La_{0.594}Fe_{0.8}Co_{0.2}O_{3.}$ NPP electrode was electrochemically tested in a porous thin film configuration (100 nm) and compared with reference materials. Impedance results highlighted an improvement of performance for the new electrode material; a possible explanation of this enhancement is the increase of chemical capacitance directly associable with oxygen vacancy concentration involved in the electrode process at low frequency, controlling the global kinetic.

Interactions between LSF64 and LBC64 were avoided in the bilayer system, preserving both phases. Two different bilayer systems were prepared and compared with pure dense thin LSF film. They consisted in a LSF64 layer covered by a LBC64 top layer: in the first case top layer had a dense structure, in the second case the layer was porous. The presence of LBC64 at gas/electrode interface drastically decrease electrode polarization resistance. DRT analysis and then equivalent circuit modeling of impedance data at different temperature and oxygen partial pressure attributed this performance improvement to the enhancement of low frequency process, related with oxygen surface phenomena. This explanation is in accordance with material properties; indeed, LBC64 surface is more active towards oxygen surface exchange than LSF64.

5.6 References

1. Y. Cheng, T.-S. Oh, R. Wilson, R. J. Gorte and J. M. Vohs, *Journal of The Electrochemical Society*, **164**, F525 (2017).
2. R. Küngas, A. S. Yu, J. Levine, J. M. Vohs and R. J. Gorte, *Journal of The Electrochemical Society*, **160**, F205 (2013).
3. A. M. Ritzmann, A. B. Muñoz-García, M. Pavone, J. A. Keith and E. A. Carter, *Chemistry of Materials*, **25**, 3011 (2013).
4. A. Schmid, G. M. Rupp and J. Fleig, *Chemistry of Materials*, **30**, 4242 (2018).
5. A. Schmid, G. M. Rupp and J. Fleig, *Physical Chemistry Chemical Physics*, **20**, 12016 (2018).
6. R. Amin, B. Kenney and K. Karan, *Journal of The Electrochemical Society*, **158**, B1076 (2011).
7. N. Arulmozhi, W. H. Kan, V. Thangadurai and K. Karan, *Journal of Materials Chemistry A*, **1**, 15117 (2013).
8. D. Garcés, A. L. Soldati, H. Troiani, A. Montenegro-Hernández, A. Caneiro and L. V. Mogni, *Electrochimica Acta*, **215**, 637 (2016).
9. G. M. Rupp, A. Schmid, A. Nenning and J. Fleig, *Journal of The Electrochemical Society*, **163**, F564 (2016).
10. C. Setevich, S. Larrondo and F. Prado, *Ceramics International*, **44**, 16851 (2018).
11. J. Liu and F. Ciucci, *Physical Chemistry Chemical Physics*, **19**, 26310 (2017).
12. W. C. Chueh, Y. Hao, W. Jung and S. M. Haile, *Nature Materials*, **11**, 155 (2011).
13. A. Nenning, A. K. Opitz, T. M. Huber and J. Fleig, *Physical Chemistry Chemical Physics*, **16**, 22321 (2014).
14. M. P. Pechini, Vol. US3330697 A, USA, in (1967).
15. W. Jung and H. L. Tuller, *ECS Transactions*, **35**, 2129 (2011).
16. F. S. Baumann, J. Fleig, H. U. Habermeier and J. Maier, *Solid State Ionics*, **177**, 3187 (2006).
17. F. S. Baumann, J. Fleig, G. Cristiani, B. Stuhlhofer, H.-U. Habermeier and J. Maier, *Journal of The Electrochemical Society*, **154**, B931 (2007).

18. H. G. Seo, Y. Choi and W. Jung, *Advanced Energy Materials*, **8**, 1703647 (2018).
19. F. S. Baumann, J. Fleig, H.-U. Habermeier and J. Maier, *Solid State Ionics*, **177**, 1071 (2006).
20. N. J. Simrick, A. Bieberle-Hütter, T. M. Ryll, J. A. Kilner, A. Atkinson and J. L. M. Rupp, *Solid State Ionics*, **206**, 7 (2012).
21. W. Jung and H. L. Tuller, *Energy & Environmental Science*, **5**, 5370 (2012).
22. J. Januschewsky, M. Ahrens, A. Opitz, F. Kubel and J. Fleig, *Advanced Functional Materials*, **19**, 3151 (2009).
23. D. Chen, S. R. Bishop and H. L. Tuller, *Journal of Electroceramics*, **28**, 62 (2012).
24. W. Jung and H. L. Tuller, *Solid State Ionics*, **180**, 843 (2009).
25. J. Jamnik and J. Maier, *Physical Chemistry Chemical Physics*, **3**, 1668 (2001).
26. W. Lai and S. M. Haile, *Journal of the American Ceramic Society*, **88**, 2979 (2005).
27. N. H. Perry and T. Ishihara, *Materials (Basel, Switzerland)*, **9**, 858 (2016).
28. B. A. Boukamp, N. Hildenbrand, H. J. M. Bouwmeester and D. H. A. Blank, *Solid State Ionics*, **283**, 81 (2015).
29. C. S. Kim and H. L. Tuller, *Solid State Ionics*, **320**, 233 (2018).
30. Y. Wang, L. Zhang, F. Chen and C. Xia, *International Journal of Hydrogen Energy*, **37**, 8582 (2012).
31. L. Wang, R. Merkle, Y. A. Mastrikov, E. A. Kotomin and J. Maier, *Journal of Materials Research*, **27**, 2000 (2012).
32. Y. Zhou, *Study on Fabrication and Performance of Metal-Supported Solid Oxide Fuel Cells*, Springer (2018).
33. S. Kogler, A. Nenning, G. M. Rupp, A. K. Opitz and J. Fleig, *Journal of The Electrochemical Society*, **162**, F317 (2015).

CHAPTER 6

Summary and perspectives

In this thesis old cathode materials such as LSM, LSCF and BSCF were considered, looking for a new way to exploit their properties (LSM) or to improve stabilty (LSCF, BSCF). Moreover, based on their complementary properties also LSF and LBC were investigated in mixing systems.

A particular attention was paid also on interpretation of impedance data using distribution of relaxation times and equivalent circuit modeling; a combination among them was proposed to obtain a more reliable data analysis, highlighting strengths and weaknesses of this integrate approach.

The first material investigated was LSM deposited onto YSZ electrolyte. Different morphology were obtained changing the sintering temperature; this allows to have sample with a different TPB and volume extension. Electrochemical results highlights a kinetic transition of oxygen reduction reaction mechanism as a function of applied overpotential. The threshold bias was 0.2 V, below this limit value the electrocatalytic process was dominated by a surface path, while for higher values a new bulk path was activated. Besides DRT and EC analysis, the regime transition was supported by the introduction of geometric index able to explain the phenomena from a morphological point of view.

A further confirmation regarding the difference nature of LSM under a cathodic bias was provided by a physically based model developed by the Department of Civil and Industrial Engineering of University of Pisa. This model is based on surface path only considering system co-limited by adsorption/diffusion of oxygen and charge transfer reaction at TPB at electrode/electrolyte interface. After model calibration, simulated impedance are able to describe real data only for overpotential value lower than 0.2 V. Increasing bias more, model diverge from experimental data, suggesting the activation of a new bulk path neglected by simulation.

Based on these results a new route for LSM application in IT-SOFC cathode has been proposed in the last section of Chapter 3. The material was infiltrated in LSCF and BSCF scaffolds to improve their stability. The presence of a discrete LSM film over the surface not only decrease the degradation rate of two materials but increase material performance, showing a new possible application.

LSCF and BSCF are the leading actor of Chapter 4; they were mixed with three different volume ratio, and samples were called (BL30, BL50, BL70). All the new electrodes showed a very promising performance in temperature range of 500 – 650 °C, with one of the lowest polarization resistance value reported in literature for perovskite-based SOFC cathode (BL70 @ 650 °C 0.021 Ω cm^2).

DRT analysis highlights a change in the kinetic mechanism from 500 °C to 650 °C, moving from a system co-limited by oxygen surface phenomena and solid-state diffusion to a kinetic governing by charge – transfer. These results were confirmed by equivalent circuit analysis performed using two different circuits at low and high temperature.

BL70 remained the most interesting system even after ageing test. In fact it showed a degradation rate in the order of 10^{-5} Ω cm^2 h^{-1}, at least one order of magnitude lower than reference materials.

In Chapter 5 other two perovskite materials were combined. LSF (stable) and LBC (high electrocatalytic activity) were mixed. Their interaction were studied in different environments. The first, was during a traditional sintering stage, which led to the formation of a new perovskite phase $Ba_{0.099}Sr_{0.297}La_{0.594}Fe_{0.8}Co_{0.2}O_3$, called NPP. The same phase was obtained also when LSF and LBC interact for the first time inside the PLD chamber under completely different working conditions.

A thin film NPP electrode was deposited onto YSZ substrates and electrochemically tested. It showed an increase in performance compared with reference materials, and analysis regarding the kinetic mechanism has been carried out, studying the influence of temperature and oxygen partial pressure. The main reason for performance improvement could be the high concentration of oxygen vacancy evaluated by means of chemical capacitance.

Lastly, two bilayer systems was investigated; it was made by a dense LSF thin film covered by a LBC top layer. All the layers were deposited by PLD technique and both the materials were detected in the tested samples. They differed for LBC layer structure, which was dense in the first case and porous in the second one. The presence of Co-based perovskite on the top of the electrode drastically reduced polarization resistance due to the enhancement of oxygen surface activity. This behavior was well highlighted by DRT analysis that show a strong fall of peak at low frequency, closely related with this kind of phenomena.

Results of this thesis open new perspectives about the employment well-known electrode material as cathode for IT-SOFCs:

1. $La_{1-x}Sr_xMnO_3$ will be optimized as stabilizing phase for porous scaffold, providing also an active surface for oxygen reduction reaction.

2. BSCF – LSCF composite electrode performance will require a deeper ageing analysis, and if the obtained results will be confirmed they can be a very promising electrode materials even for temperature close to 600 °C. Moreover, another interesting point will be the study of LSM – infiltration on these cathodes a solution to improve stability.

3. LSF64-LBC64 system will be tested in a porous electrode closer to commercial application. The main idea is based on the preparation of LSF64 scaffold electrode that will be impregnated by a LBC64 phase, in order to reproduce the last thin film system proposed in Chapter 5.

List of Figures

List of tables

Publications

List of journal articles

1. R. Oriol, **D. Clematis**, E. Brillas, J.L. Cortina, M. Panizza, I. Sirés;
   "*Groundwater treatment using a Solid Polymer Electrolyte Cell with Mesh Electrodes".*
   ChemElectroChem 6 (2019) 1235-1243

2. **D. Clematis**, A. Barbucci, S. Presto, M. Viviani, M.P. Carpanese;
   "*Electrocatalytic Activity of Perovskite-based Cathode for Solid Oxide Fuel Cells".*
   International Journal of Hydrogen Energy 44 (2019) 6212 – 6222

3. **D. Clematis**, J. Abidi, G. Cerisola, M. Panizza;
   "*Coupling BDD anode with solid polymer electrolyte to avoid the addition of supporting electrolyte in electrochemical advanced oxidation processes".*
   ChemElectroChem (In Press)

4. A. Bertei, E. Ruiz-Trejo, **D. Clematis**, M.P. Carpanese, A. Barbucci, C. Nicolella, N. Brandon;
   "*A Perspective on the Role of the Three-Phase Boundary in Solid Oxide Fuel Cell Electrodes".*
   Bulgarian Chemical Communications 50 (2018) 31-38

5. M.P. Carpanese, **D. Clematis**, M. Viviani, S. Presto, G. Cerisola, M. Panizza, M. Delucchi, A. Barbucci;
   "*A Comprhensive Approach to Improve Performance and Stability of State-of-the-Art Air Electrodes for Intermediate Temperature Reversible Cells: An Impedance Spectroscopy Analysis*
   Bulgarian Chemical Communications 50 (2018)39-47

6. M. Viviani, A. Barbucci, M.P. Carpanese, R. Botter, **D. Clematis**, S. Presto;
   "*Ionic Conductivity of Na-doped $SrSiO_3$"*
   Bulgarian Chemical Communications 50 (2018)55-61

7. N. Klidi, **D. Clematis**, M. P. Carpanese, A. Gadri, S. Ammar, M. Panizza;
   "*Electrochemical oxidation of crystal violet using a BDD anode with a solid polymer electrolyte".*
   Separation and Purification Technology 208 (2019) 178 –183
   https://doi.org/10.1016/j.seppur.2018.03.042

8. N. Klidi, **D. Clematis**, M. Delucchi, A. Gadri, S. Ammar, M. Panizza;
"*Applicability of electrochemical methods to paper mill wastewater for reuse. Anodic oxidation with BDD and $TiRuSnO_2$* anodes".
Journal of Electroanalytical Chemistry 799 (2018) 34-39
https://doi.org/10.1016/j.jelechem.2018.02.063

9. S. Cotillas, **D. Clematis**, P. Canizares, M. P. Carpanese, M. A. Rodrigo, Marco Panizza;
"Degradation of dye Procion Red MX-5B by electrolytic and electro-irradiated technologies using diamond electrodes".
Chemosphere 19 (2018) 445-452
https://doi.org/10.1016/j.chemosphere.2018.02.001

10. M.P. Carpanese, **D. Clematis**, M. Viviani, S. Presto, M. Panizza, G. Cerisola, A. Barbucci;
"*Characterization of LSCF-BSCF composite cathode for Solid Oxide Fuel Cells"*
Bulgarian Chemical Communications 50 (2018) 95-101

11. **D. Clematis,** N. Klidi , A. Barbucci, M.P. Carpanese, M. Delucchi, G. Cerisola, M.Panizza;
"*Application of Electro-Fenton process for the treatment of Methylene Blue"*.
Bulgarian Chemical Communications 50 (2018) 22-26

12. S. Cotillas, J. Llanos, P. Cañizares, **D. Clematis**, G. Cerisola, M. Rodrigo, M. Panizza;
"*Removal of Procion Red MX-5B dye from wastewater by conductive-diamond electrochemical oxidation"*.
Electrochimica Acta 263 (2018) 1-7
https://doi.org/10.1016/j.electacta.2018.01.052

13. S. Elleouze, S. Kessemtini, **D. Clematis**, G. Cerisola, M. Panizza, S.C. Elaoud;
"*Application of Doehlert design to the electro-Fenton treatment of Bismarck Brown Y".*
Journal of Electroanalytical Chemistry 799 (2017) 34-39
https://doi.org/10.1016/j.jelechem.2017.05.042

14. A. Giuliano, M. P. Carpanese, **D. Clematis**, M. Boaro, A. Pappacena, F. Deganello, L. F. Liotta and A. Barbucci.
"*Infiltration, Overpotential and Ageing Effects on Cathodes for Solid Oxide Fuel Cells: $La_{0.6}Sr_{0.4}Co_{0.2}Fe_{0.8}O_{3-\delta}$ versus $Ba_{0.5}Sr_{0.5}Co_{0.8}Fe_{0.2}O_{3-\delta}$"*.
Journal of The Electrochemical Society 164 (2017) F3114-F3122
doi: 10.1149/2.0161710jes

15. A. Giuliano, M.P. Carpanese, M. Panizza, G. Cerisola, **D. Clematis**, A. Barbucci;
"*Characterization of $La_{0.6}Sr_{0.4}Co_{0.2}Fe_{0.8}O_{3-\delta}$ - $Ba_{0.5}Sr_{0.5}Co_{0.8}Fe_{0.2}O_{3-\delta}$ composite as cathode for solid oxide fuel cells".*
Electrochimica Acta 240 (2017) 258-266
https://doi.org/10.1016/j.electacta.2017.04.079

16. A. Bertei, M.P. Carpanese, **D. Clematis**, A. Barbucci, M. Z. Bazant, C. Nicolella;
"*Understanding the electrochemical behavior of LSM-based SOFC cathodes. Part-II Mechanistic modelling and physically – based interpretation".*
Solid State Ionics 303 (2017) 181-190
https://doi.org/10.1016/j.ssi.2016.09.028

17. M.P. Carpanese, **D. Clematis**, A. Bertei, A. Giuliano, A. Sanson, E. Mercadelli, C. Nicollela, A. Barbucci;
"Understanding the electrochemical behaviour of LSM-based SOFC cathodes. Part I – Experimental and electrochemical".
Solid State Ionics 301 (2017), 106-115
https://doi.org/10.1016/j.ssi.2017.01.007

18. **D. Clematis**, G. Cerisola, M. Panizza;
"Electrochemical oxidation of a synthetic dye using a BDD anode with a solid polymer eletrolyte".
Electrochemistry Communications 75 (2017) 21-24
https://doi.org/10.1016/j.elecom.2016.12.008

19. M. Panizza, **D. Clematis**, G. Cerisola;
"*Electrochemical treatment of poorly biodegradable DPC cationic surfactant".*
Journal of Environmental Chemical Engineering 4 (2016) 2692–2697
https://doi.org/10.1016/j.jece.2016.05.013

List of contributions to conferences

1. Oral contribution at 11th International Workshop on Impedance Spectroscopy – Chemnitz, Germany.
   D. Clematis, M.P. Carpanese, G. Cerisola, M. Panizza, S. Presto, M. Viviani, M. Delucchi, A. Barbucci;
   "*Identification of characteristic frequency by means of distribution of relaxation time and Bode's diagram in cathodes for Solid Oxide Fuel Cells".*
   September, 27-28 2018

2. Poster at 69th Annual Meeting of the International Society of Electrochemistry – Bologna, Italy.
   D. Clematis, N. Klidi, G. Cerisola, M. Delucchi, M.P. Carpanese, A. Barbucci, M . Paniza;
   "*Solid Polymer Electrolyte: an approach for electrochemical wastewater treatment with low conductivity".*
   September, 2-7 2018

3. Poster at 69th Annual Meeting of the International Society of Electrochemistry – Bologna, Italy.
   D. Clematis, M.P. Carpanese, S. Presto, M. Viviani, G. Cerisola, M. Panizza, M. Delucchi, A. Barbucci; "*Will distribution of relaxation time and equivalent circuit ever be friends? Kinetic mechanism transition in LSCF – BSCF cathodes".*
   September, 2-7 2018

4. Oral contribution at 69th Annual Meeting of the International Society of Electrochemistry – Bologna, Italy.
   A. Bertei, E. Ruiz-Trejo, V. Yufit, F. Tariq, N. Brandon, **D. Clematis**, M.P. Carpanese, A. Barbucci, C. Nicolella; "*Unveiling the complex interplay between nanoscale electrochemical reactions and microscale electrode architecture in solid oxide fuel cells via physically-based modeling".*
   September, 2-7 2018

5. Oral contribution at XXXIX Meeting of the Electrochemistry Group of the Spanish Royal Society of Chemistry and 3rd E3 Mediterranean Symposium: Electrochemistry for Environment and Energy. Madrid, Spain.
   D. Clematis, M.P. Carpanese, S. Presto, M. Viviani, M. Panizza, A. Barbucci; "*Enhanced electrocatalytic activity of perovskite materials in energy conversion by intermediate temperature solid oxide fuel cells".*
   July 2-5, 2018

6. Oral contribution at XXXIX Meeting of the Electrochemistry Group of the Spanish Royal Society of Chemistry and 3rd E3 Mediterranean Symposium: Electrochemistry for Environment and Energy. Madrid, Spain.
   D. Clematis, N. Klidi, G. Cerisola, M.P. Carpanese, M. Delucchi, A. Barbucci, M. Panizza; "*Electrochemical treatments and low conductivite solutions: overcoming supporting electrolyte addition".*
   July 2-5, 2018

7. Poster at. IX Giornate Italo-Francesi di Chimica.
   Genova, Italy
   M. Panizza, F. Portesine, F. Vaccaro, C. Carbone, **D. Clematis**, A. Calcagno; "*Innovative high capacity mobile storage for consumer market".*
   April 16-18, 2018

8. Oral contribution at Giornate dell'Elettrochimica Italiana.
   Sestriere, Italy
   A. Barbucci, **D. Clematis**, A. Bertei, C. Nicolella, M.P. Carpanese; "*Impedance study of perovskite materials for IT-SOFC: case of* $La_{0.8}Sr_{0.2}MnO_{3-\delta}$, $La_{0.8}Sr_{0.2}Co_{0.2}Fe_{0.8}O_{3-\delta}$ *and* $Ba_{0.5}Sr_{0.5}Co_{0.8}Fe_{0.2}O_{3-\delta}$*".*
   January 21-25, 2018

9. Poster at Giornate dell'Elettrochimica Italiana.
   Sestriere, Italy
   M.P. Carpanese, **D. Clematis**, G. Cerisola, M. Panizza, M. Delucchi, S. Presto, M. Viviani, A. Barbucci; "*Kinetics of* $La_{0.8}Sr_{0.2}Co_{0.2}Fe_{0.8}O_{3-\delta}$ *and* $Ba_{0.5}Sr_{0.5}Co_{0.8}Fe_{0.2}O_{3-\delta}$ *composite as cathode for IT-SOFCs".* January 21-25, 2018

10. Poster at Giornate dell'Elettrochimica Italiana.
    Sestriere, Italy
    A. Bertei, E. Ruiz-Trejo, K. Kareh, **D. Clematis**, M.P. Carpanese, A. Barbucci, M. Bazant, C. Nicolella, N. Brandon; *"Do electrochemical reactions realla take place at the three-phase boundary in solid oxide fuel cells?".*
    January 21-25, 2018

11. Poster at 11th International Symphosium on Electrochemical Impedance Analysis 2017.
    Camogli, Italy.
    D. Clematis, M.P. Carpanese, S. Presto, M. Viviani, A. Barbucci; *"Impedance study on LSCF-BSCF composite system: effect of temperature and overpotential"*.
    November 6-10, 2017

12. Poster at 11th International Symphosium on Electrochemical Impedance Analysis 2017.
    Camogli, Italy.
    M.P. Carpanese, **D. Clematis**, S. Presto, M. Viviani, F. Deganello, L.F. Liotta, M. Delucchi, M. Panizza, G. Cerisola, A. Barbucci; *"Redox properties of LSCF-BSCF cathodes and effect of infiltration by LSM"*.
    November 6-10, 2017

13. Poster at 11th International Symphosium on Electrochemical Impedance Analysis 2017.
    Camogli, Italy.
    M. Viviani, A. Barbucci, M.P. Carpanese, R. Botter, **D. Clematis**, S. Presto; *"Ionic conductivity of Na-doped SrSiO3".*
    November 6-10, 2017

14. Oral contribution at 11th International Symphosium on Electrochemical Impedance Analysis 2017.
    Camogli, Italy.
    Bertei, E. Ruiz-Trejo, K. Kareh, **D. Clematis**, M.P. Carpanese, A. Barbucci, M.Z. Bazant, C. Nicolella, N.P. Brandon; *"Physically-based modelling of solid oxide fuel cells: overcoming the three-phase boundary paradigm".*
    November 6-10, 2017

15. Oral contribution at 11th International Symphosium on Electrochemical Impedance Analysis 2017.
    Camogli, Italy.
    M.P. Carpanese, G. Caboche, L. Combemale, **D. Clematis**, A. Bertei, C. Nicolella, A. Barbucci; "*Impedance characterisation of perovskites as cathodes for IT-SOFCs: from typical* $La_{0.8}Sr_{0.2}MnO_{3-\delta}$ *to high-performing* $La_{0.6}Sr_{0.4}Co_{0.2}Fe_{0.8}O_{3-\delta}$ *and* $Ba_{0.5}Sr_{0.5}Co_{0.8}Fe_{0.2}O_{3-\delta}$*".*
    November 6-10, 2017

16. Oral contribution at 21st International Conference on Solid State Ionics.
    Padova, Italy.
    M.P. Carpanese, **D. Clematis**, S. Presto, M. Viviani, A. Barbucci; *"*$La_{0.6}Sr_{0.4}Co_{0.2}Fe_{0.8}O_{3-\delta}$ *-* $Ba_{0.5}Sr_{0.5}Co_{0.8}Fe_{0.2}O_{3-\delta}$ *composite cathode for intermediate - temperature solid oxide fuel cells".*
    June 18-23, 2017